Boston University

OpenBU **http://open.bu.edu**

Boston University Theses & Dissertations Boston University Theses & Dissertations

2024

Local gauge symmetry and emergence of topological order in quantum spin systems

https://hdl.handle.net/2144/49800

Downloaded from OpenBU. Boston University's institutional repository.

BOSTON UNIVERSITY

GRADUATE SCHOOL OF ARTS AND SCIENCES

Dissertation

LOCAL GAUGE SYMMETRY AND EMERGENCE OF TOPOLOGICAL ORDER IN QUANTUM SPIN SYSTEMS

by

KAI-HSIN WU

B.S., National Taiwan University, 2016
M.S., National Taiwan University, 2018

Submitted in partial fulfillment of the
requirements for the degree of
Doctor of Philosophy

2024

© 2024 by
KAI-HSIN WU
All rights reserved

Approved by

First Reader

Claudio Chamon, Ph.D.
Professor of Physics

Second Reader

Anders Sandvik, Ph.D.
Professor of Physics

To my parents.

Acknowledgments

As people often say, “It was the best of times, it was the worst of times.” Life was especially challenging when Covid-19 accompanied most of my graduate years.

Reflecting on my graduate school journey at Boston University, I always consider myself fortunate to have both Anders Sandvik and Claudio Chamon as my advisors. They not only possess extensive and comprehensive knowledge in physics, guiding me through academic adventures, but they’ve also been mentors who were there to support me through life’s ups and downs, encouraging me to think, explore, and pursue my future. Their genuine curiosity toward physics is truly inspiring. I’ve always been amazed by their scientific insights and their ability to motivate the study of challenging problems. They have been like beacons, always there to point me in the right direction when I felt lost. What else could you ever dream of than having such wonderful mentors in your life?

My achievements during graduate studies would not have been possible without the help of my collaborators. I want to express my gratitude to Zhi-Cheng Yang for helping me settle down when I first moved to the United States and for collaborating with me on my first project at BU. I would also like to thank our cohort: Sumner Hearth, Maria Yampolskaya, Jacob Warshauer, Anna Tsatsos, Hasung Song, Jiin So, Nathan Rose, Ziwei Huang, and Adam Lux. Our cohort was truly exceptional, and I couldn’t have asked for better colleagues. I want to express my appreciation to Gabe Schumm, Bowen Zhao, Sibin Yang, Jun Takahashi, Pranay Patil, and Philip Weinberg, who were part of my early days in graduate school. Not to forget my group members Shiyu Zhou, Elliot Yu, Aleksei Khudorozhkov, and Guilherme Delfino, who have always been fun, curious, and excited about physics. Engaging in discussions with them has consistently been one of my favorite activities. Special thanks go to my office mates Sumner, Matteo and Gautam, who were always willing to listen to

my complaints and discuss the problems I faced in my projects. I would also like to express my gratitude to the entire CMT (Condensed Matter Theory) community at Boston University for fostering a friendly and collaborative environment.

I especially want to thank Jackson Nguyen, whom I'd like to take a moment to express just how much you mean to me for the unwavering support, encouragement, and love that you have showered upon me throughout this journey. Your presence in my life has been a constant source of strength and inspiration ever since I met you.

Lastly, I want to thank my family for their unwavering support and encouragement in every decision I made. Without them, I would not have been able to come to the United States to pursue my dreams. They always encouraged me to boldly explore the unknown, knowing that I could always return to them when I needed a moment of rest and comfort.

Kai-Hsin Wu

LOCAL GAUGE SYMMETRY AND EMERGENCE OF TOPOLOGICAL ORDER IN QUANTUM SPIN SYSTEMS

KAI-HSIN WU

Boston University, Graduate School of Arts and Sciences, 2024

Major Professors: Claudio Chamon, Ph.D.
Professor of Physics

Anders Sandvik, Ph.D.
Professor of Physics

ABSTRACT

Topological quantum states of matter are a central focus in modern condensed matter physics and quantum information science. The study of topological order in quantum spin systems is closely linked to the concept of gauge symmetries. In this dissertation, we conduct detailed studies of two quantum spin systems with local gauge symmetries. Specifically, we numerically investigate a recently proposed theoretical model that realizes local Z_2 gauge symmetry with only two-body interactions. We confirm the existence of topological order and explore other physical properties within the model in depth. In the study of the $U(1)$ toric code, we enhance the conventional Kitaev's toric code by introducing global $U(1)$ symmetry. The study emphasizes the interplay between local Z_2 gauge symmetry and constraints arising from global $U(1)$ symmetry. This examination uncovers the presence of topological degeneracy and reveals an unconventional UV/IR mixing phenomenon within the system. We explore possible implementations of the $U(1)$ toric code in superconducting wires and discuss potential future research directions based on the insights gained

from our investigations of these two models.

Contents

1 Introduction **1**

2 Overview of Topological Phases and Symmetries **4**

2.1 Z_2 Local Gauge Symmetry in Spin systems 4

2.1.1 Toric code 4

2.1.2 Z_2 lattice gauge model 10

2.1.3 Toric code on a ladder 11

3 Z_2 Topological Order and First-Order Quantum Phase Transitions **17**

3.1 Local Z_2 Gauge Symmetry with Two-body terms 19

3.1.1 Z_2 Combinatorial Gauge Symmetries 19

3.1.2 Adding kinetic terms 25

3.2 Stochastic Series Expansion for CGS Models 28

3.3 Results of Model-X: Transverse Field on The Gauge Spins 33

3.3.1 Fidelity Susceptibility and Phase Boundary 34

3.3.2 Topological Order 38

3.3.3 First Order Phase transition 40

3.4 Results of Model-XX: Ferromagnetic XX-interaction On The Gauge Spins 46

3.4.1 Phase Boundary 46

3.4.2 Topological Order 47

3.4.3 First Order Phase Transition 47

3.5 Low-Energy Excitations in the Topological Phase 48

3.5.1 Level Spectroscopy for Model-X 49
3.5.2 Level Spectroscopy for Model-XX 54

4 $U(1)$ Symmetry-Enriched Toric Code **64**
4.1 Kitaev's Z_2 Toric Code with U(1) symmetry 66
4.1.1 U(1) toric code on a ladder 68
4.1.2 U(1) toric code on 2D lattice 70
4.2 Quantum Monte Carlo with Generalized Sweeping Cluster Update . . 71
4.3 Hilbert Space Fragmentation 76
4.4 Topological Degeneracy and UV/IR Mixing 80
4.4.1 Lowest Energy in Topological Sectors 82
4.4.2 Discussion on Topolgoical order and UV/IR mixing 86
4.5 Other Properties 88
4.5.1 Correlation Functions 88
4.5.2 Symmetry Breaking 91
4.6 Proposal for Experimental Realization 92

5 Conclusion and Future Directions **101**

References **104**

Curriculum Vitae **113**

List of Figures

2·1 (a) The square lattice that defines the toric code. The blue crosses represent the star operator A_s, defined as the product of σ_z operators along the dashed-arrow closed-loop surrounding a 'star', while the red boxes represent the plaquette operator B_p, defined as the product of 4 σ_x operators on the edges of the box. (b) When putting on a torus, 4 additional operators $W_{x,y}$ defined as product of σ_z along the line and $V_{x,y}$ defined as product of σ_x are also conserved. 5

2·2 (a) An example illustrating the conversion of a non-contractible operator W_y to $W_{y'}$ by taking the product with a series of local star operators. (b) The action of the non-contractible loop operator V_x along the x-direction, as indicated by the red arrow. This operator passes an even number of spins for elementary star operators, intersecting one spin of the non-contractible loop W_y, thus causing a flip in the quantum number. 8

2·3 (a)The excitation generated by acting a σ_z operator that creates two m excitation (visons) on the dual lattice, which represented as flipping two nearest-neighbor plaquette operators.(b)The excitation generated by acting a σ_x operator that creates two e excitation (spinons) on the lattice site, which represented as flipping two nearest-neighbor star operators. 10

2·4 The toric code on a ladder has its star term, A_s^x, defined as the product of σ^x for four spins on a site, depicted as a red star. The plaquette term B_p^z is a symmetry operator, defined as the product of two σ^z acting on plaquette p. 12

2·5 The quantum number of B_p^z divides the local Hilbert space into two parts: (a) With $B_p^z = +1$, the local space is spanned by $|\uparrow\uparrow\rangle, |\downarrow\downarrow\rangle$. (b) With $B_p^z = -1$, the local space is spanned by $|\uparrow\downarrow\rangle, |\downarrow\uparrow\rangle$. 13

2·6 The mapping to the transverse field Ising model in the sector with two visons (indicated by $B_p^z = -1$ at the locations shown in light orange) transforms the red star operator into the nearest neighbor ferromagnetic interaction $\tau_p^x \tau_{p+1}^x$. Furthermore, the operator $\hat{Z}_p$ is mapped to τ_p^z only at locations where $B_p^z = +1$. 15

3·1 (a) The arrangement of two species of Ising spins on a square lattice. Gauge spins (green squares) reside on the links and four matter spins (orange dots) occupy each site of the square lattice. (b) The vertex unit and the interactions between spins. The interactions between gauge-matter spins within a single unit are defined by the Hadamard matrix $\mathbf{W}$ in Eq. (3.3). For clarity, the couplings are depicted on a deformed cell in panel (c), where the ferromagnetic and antiferromagnetic couplings are shown as thin blue lines and bold red lines, respectively. . . 19

3·2 Connection between the model in our studies to the Z_2 gauge theory. The red star in (a) represents the expanded 4-body interacting term that is equivalent to the star term $\prod \sigma^z$ of the Z_2 gauge model in (b). The blue plaquette in (a) represents the local combinatorial gauge generator G_p by analogy with the local gauge generator B_p of the Z_2 gauge model defined as $\prod \sigma^x$ of the 4 spins around a plaquette in (b). 21

3·3 (a) Definitions of M independent gauge operators in the conventional Z_2 model for a system of size 2×2. (b) The corresponding operators define on the lattice of combinatorial Z_2 model. Here, G_x and G_y are the gauge operators defined on non-contractible loops along x and y direction respectively. 24

3·4 The second-order process generates the effective plaquette term in model-XX. The A-sublattice is marked in light yellow while the B-sublattice is indicated in white. **(a)** The processes that couple two stars in the A (top part) or B (bottom part) sublattice with an effective ferromagnetic interaction. **(b)** The arrangement of XX bonds (dashed lines) resulting in an effective TFIM on A and B sublattices. Different colors indicate bonds coupling sites in the A and B sublattices. 26

3·5 All allowed vertices for model-X. (a) FM and AFM vertices associate with the operators $U_{t=3}$. (b) Single-site constant vertices associate with $U_{t=1}$. (c) Single-site spin flip vertices associate with the off-diagonal operators $K_{t=1}$ and $K_{t=2}$. 31

3·6 All possible vertices for model-XX. (a) FM and AFM vertices associate with $U_{t=4}$. (b) Single-site constant vertices associate with $U_{t=1}$. (c) Single-site spin flip vertices associate with $K_{t=1}$. Vertices that represent the two-site operators of type $t = 2$ are represented by the red dashed lines, with diagonal constant (d) $U_{t=2}$ and off-diagonal term (e) $K_{t=2}$. Vertices corresponding to two-site operator of type $t = 3$ are represented by the blue-dotted line, with diagonal constant (f) $U_{t=3}$ and off-diagonal (g) $K_{t=3}$. (h) Illustration of the possible vertex processes for both type-2 and type-3 operators in the cluster update for model-XX. (i) An example of an update of the kind $U_{t=2} \rightarrow K_{t=2}$. . 33

3·7 (a) Phase diagram of model-X. The red curve is the perturbative large-Γ_m phase boundary, Eq. (3.39), between Z_2 quantum spin liquid and the confined (paramagnetic) phase, resulting from the mapping to the Z_2 lattice gauge model. Blue crosses are the boundary points from the location of maximum fidelity susceptibility calculated with ED, as shown in (b). The two open circles represent the $L \to \infty$ transition point extrapolated from the QMC data simulated at fixed $\Gamma_g = 0.2$ and 1.0, where the extrapolated transition points are at $\Gamma_m \approx 2.27$, and $\Gamma_m \approx 1.0$, respectively. The Fidelity susceptibilities χ_F^m in (b) and χ_F^g in (c) were calculated using Lanczos ED with $N = 2 \times 2 \times 6$ spins. 35

3·8 SSE results for the size-normalized fidelity susceptibilities χ_F^m/N (a) and χ_F^g/N (b) for systems with different number of spins $N = L \times L \times 6$. All data points for a given L were obtained in the same simulation with quantum parallel tempering at fixed $\Gamma_g = 0.2$ and inverse temperature $\beta = 4L$. The insets show log-log plots of the peak value of the fidelity susceptibility versus L, along with solid lines drawn through pairs of data points with L and $L+2$ to analyze power-law behaviors $\chi_F/N \sim L^{b_L}$. The extracted size-dependent exponents in (a) are $b_4 \approx 3.0$ from the $L = 4, 6$ points and $b_6 \approx 3.5$ from $L = 6, 8$. In (b) the $L = 4, 6$ points give $b_4 \approx 2.7$ and $L = 6, 8$ give $b_6 \approx 3.2$. The dotted lines in the insets of (a) and (b) have a slope $b = 2(d+1) - d = 4$ corresponding to a first-order transition and are shown as a reference. 37

3·9 Wilson-loop correlation function obtained in SSE simulations. (a) Results for the CGS model-X with $\Gamma_g = 0.2$. Data for different system sizes show convergence to a finite value for $\Gamma_m \approx 2.3$, with the expected value $C_p(L/2) = 1$ in the $\Gamma_m \to 0$ limit. The inset illustrates the definition Eq. (3.44) of the correlation function in terms of two parallel non-contractible Wilson loops in the x direction of a periodic lattice of size $L = 4$. (b) Results for square-lattice TFIM for several system sizes at inverse temperature $\beta = 2L$. The inset shows the finite-size scaling of the location $h_x^*(L^{-1})$ for which the value of the correlator is $1/2$, as indicated by the horizontal dashed line. A power-law fit $y = a + bL^{-c}$ for the $L \geq 12$ data gives $a = -0.02(1)$, $b = 3.15(2)$ and $c = 0.472(7)$, indicating a vanishing value of the correlator at any transverse field in the thermodynamic limit. 39

3.10 Results for the model-X at $\Gamma_g = 0.2$. (a) The Binder ratio B defined with both components of the Wilson loop order parameter $P^2 = P_x^2 + P_y^2$ in Eq. (3.46). The peaks adjacent to the phase transition for system sizes $L \geq 6$ (barely discernible for $L = 6$) are signatures of a first-order transition. (b) The numerical derivative of B with respect to Γ_m [computed using the linear approximation between the successive points in (a)]. The inset shows a power-law fit $y \propto L^b$ to the maximum value of the derivative, with only the largest three system sizes included. The exponent is $b \approx 3.0$, which is consistent with expected value $b = d + 1 = 3$ for a first-order transition. (c) Scaling with the inverse system size of the Γ_m values of the finite-size maxima $dB/d\Gamma_m$, χ_F^m/N and χ_F^g/N, with $\Gamma_g = 0.2$. Both $dB/d\Gamma_m^*$ and χ_F^{g*}/N have been fitted with a single power-law correction and give the $L \to \infty$ extrapolated values $\Gamma_m^c = 2.31(3)$ and $\Gamma_m^c = 2.27(4)$, respectively. The apparent large subleading corrections to χ_F^{m*} location forbid us to get a reasonable extrapolation based on the available data, though the $L = 6$ and $L = 8$ pints show full consistency with the other estimates. . . . 57

3.11 Distribution $\rho(P_x, P_y)$ of the Wilson loop order parameter accumulated in SSE simulation at $\Gamma_g = 0.2$ and three different values of the matter field; (a) $\Gamma_m = 2.3952$ (in the Z_2 QSL phase), (b) $\Gamma_m = 2.4343$ (close to the transition point), and (c) $\Gamma_m = 2.4563$ (in the confined phase). Near the transition point, in (b), five peaks are clearly observed, reflecting phase coexistence at a first-order transition. 58

3·12 (a) Energy density computed in SSE simulations with $\Gamma_g = 0.2$. (b) The corresponding derivatives are taken numerically based on the available data in (a). Features indicating a discontinuity developing with increasing L demonstrate a first-order transition. We have fitted lines to the $L = 8$ data away from the sharp features and observe the presence of a jump when these forms are extrapolated to the location of the sharp peak (the vertical dashed line, which can be taken as a finite-size definition of the transition point). 58

3·13 (a) Phase diagram of the model with XX interactions. The red curve is the approximate phase boundary obtained from the asymptotic $\Gamma_m \to \infty$ mapping to the TFIM. This boundary separates the Z_2 topological quantum spin liquid and the ferromagnetic phases. The blue crosses are points on the boundary estimated from the maximum of the fidelity susceptibility in (b), calculated using ED on an $L = 2$ system. The green open circle indicates the $L \to \infty$ extrapolated transition point $J_x \approx 0.706$ from QMC simulations at $\Gamma_m = 1.0$. (c) Fidelity susceptibility of model-XX at $\Gamma_m = 1.0$ for different system sizes L calculated using SSE simulation at inverse temperature $\beta = 4L$. The inset shows power-law fits $y \propto L^{b_L}$ to the maximum values for system sizes L and $L + 2$. The exponents are $b_2 \approx 4.9$ and $b_4 \approx 3.9$. The slope of dotted line corresponds to the predicted exponent $b_\infty = 2(d + 1) - d = 4$ expected for a first-order transition. 59

3·14 QMC results for model-XX at $\Gamma_m = 1.0$ for the Wilson loop correlation function, Eq. (3.44). 59

3.15 Results for model-XX at $\Gamma_m = 1.0$. (a) The Binder ratio of the Wilson loop order parameter defined with both components in Eq. (3.45); $P^2 = P_x^2 + P_y^2$. The divergent peak next to the step indicates phase coexistence at a first-order transition. Accordingly, in (b) the derivative of the Binder ratio shows divergent positive and negative peaks. (c) Energy per spin of model-XX obtained in the same simulations as the other quantities at $\Gamma_m = 1.0$ and temperature $T = (4L)^{-1}$. (d) The derivatives are evaluated using the linear approximation using the data in (c). The dotted lines are fits to the $L = 4$ results away from the peak and demonstrate a jump in the energy derivative at the transition (here represented by the peak location as indicated by the vertical dashed line). 60

3·16 ED level spectrum at $\Gamma_g = 0.2$ for a system of size $L = 2$ ($N = 2 \times 2 \times 6$ spins). In (a) the two lowest energy gaps relative to the ground state (marked Gnd in the legends) are graphed versus the matter field strength for each of the 32 blocks with quantum numbers $\mathbf{q} = (\pm, \pm, \pm, \pm, \pm)$. Many blocks are degenerate because of lattice symmetries; thus the number of different curves is much less than 64. The four states that become degenerate topological ground states in the Z_2 phase are marked by blue crosses (the finite-size ground state), red stars, and green triangles (two degenerate sectors); these states all have the local quantum numbers $G_i = +1$. The blue dots represent all other lowest block levels; these are states with visons (two or a larger even number) of the topological phase (marked by v in the inset illustration). The orange curves represent the second-lowest states in each block; they correspond to the spinon excitations (particles indicated in the inset by s) of the topological phase and they all become degenerate for $\Gamma_m \to 0$. In (b), the lowest block states are graphed on a magnified scale. The eight-fold degenerate level that is the lowest excitation in the paramagnetic phase was calculated with both ED (yellow dots) and extracted from imaginary-time correlations from QMC simulations (violet circles), to demonstrate the correctness of the latter for $L = 2$. QMC results for both $L = 2$ and $L = 4$ (calculated at inverse temperature $\beta = 24L$) are shown in the inset. 61

3·17 The on-site σ_z operator creates a pair of visons when acting on the ground state with quantum number $\mathbf{q} = (+, +, +, +, +)$. The quantum number corresponding to the operators G_1 and G_3 is then changed, leading to an excited state with quantum number $\mathbf{q}' = (+, +, -, +, -)$. 62

3·18 The low-energy levels previously shown in Fig. 3·19, now marked by the eigenvalues ±1 of the spin-inversion operator, Eq. (3.62), in model-XX at $\Gamma_m = 1$. The gaps to the symmetric and antisymmetric states are marked with blue and red symbols, respectively. Out of all 64 states shown here, all the vison excitation states as well as the ground state are symmetric. The spinon excitations are all antisymmetric, except for the highest one, where a level crossing causes a change in symmetry at $J_x \approx 0.7$. 62

3·19 Level spectrum relative to the ground state for the $L = 2$ system with XX interactions, calculated with Lanczos ED. The organization of panels (a) and (b) is as in the corresponding Fig. 3·16 for the model-X. We refer to the same for further explanation of the visualization of the spectrum. The lowest spinon excitation, shown as orange circles with a dashed line, is the first excited state from the same block as the ground state (which has $\mathbf{q} = +++++$). This state is antisymmetric with respect to spin inversion and forms the two-fold degenerate multiplet together with the corresponding symmetric state in the ferromagnetic phase. 63

4·1 The dual mapping of the U(1) toric code ladder results in disconnected chains with XY and Ising interactions, depending on the sign of the plaquette B_p^z. In the upper graph, $B_p^z = -1$ is indicated by light orange ovals, and $B_p^z = +1$ is indicated by light yellow ovals. The mapping transforms the U(1) star operator into segments of an FM Ising chain where $B_p^z = -1$ consecutively, while consecutive $B_p^z = +1$ maps to segments of an XY chain. 70

4·2 (a) 6 allowed off-diagonal vertices from the Hamiltonian. Black (white) dots denote spin-up (spin-down). The four dots below (above) the line denote the classical configuration of the four spins on a star before (after) the application of a Hamiltonian term. (b) 16 additional allowed diagonal vertices after adding a constant to the Hamiltonian. The 12 vertices marked by green frames are the flippable stars. 72

4·3 (a) Example of a cluster. It starts as 4 defect lines coming out of a flippable star. The defect lines propagate upward along the "imaginary time" direction, modifying the vertices they encounter according to specified rules. After a vertex, the number of defect lines might potentially increase/decrease. Finally, the cluster terminates at another flippable star. (b) Examples of vertex updates. If a new configuration of the bottom four spins is not flippable, there is a unique way to propagate the defect lines, such that the new vertex remains allowed. (c) Examples of vertex updates. If less than 4 defect lines hit a vertex and update the bottom four spins to a flippable configuration, there are two possible ways to propagate the defect lines. We choose one of them with probability 1/2. Processes marked by the orange frame are the updates from a non-flippable vertex to a flippable vertex, for which the reverse process does not have probability 1/2. Blue arrows denote the defect lines propagating along the "imaginary time" direction (from bottom to top). 74

4·4 Ground state energy in four topological sectors of a system of size 4 × 4 stars. (dots) obtained from the SSE QMC with the generalized sweeping cluster update algorithm; (dashed lines) obtained from the ED calculation. 76

4·5 (a) Two states from the same symmetry sector, but from different fragments: an inert state with no flippable stars (top), and a state where every star is flippable (bottom) (b) Basis states of a 7-dimensional Krylov subsector. Black dots denote spin-downs, white dots (or the absence of a dot) denote spin-ups. 78

4·6 Exact enumeration study of the fragmentation fraction is defined as D_{max}/D, where D_{max} is the size of the largest fragment, and D is the size of the sector. The corresponding topological sectors are marked at the lower-left side of each figure. 79

4·7 An example of a lattice with compactification $a = 1, b = 2$ and linear size $L = 2$. Any vector $\vec{r}$ is identified with vectors $\vec{r} + \vec{L}_1$ and $\vec{r} + \vec{L}_2$. The whole lattice is shown in bright colors, while the shaded region denotes repeating parts of the lattice due to the periodic boundary condition. Two non-contractible loops γ_x and γ_y shown as purple and yellow dotted lines respectively along two compactification vectors $\vec{L}_1$ and $\vec{L}_2$. 81

4·8 Energy gaps between the ground states in different topological sectors as a function of system size L. (a) For 0°-tilt compactification. $E_{W_x W_y, W'_x W'_y}$ labels the energy difference between sectors (W_x, W_y) and (W'_x, W'_y). For all system sizes, the sector $(-,-)$ has the lowest energy. The inset shows that the finite size gap $\Delta E_{++,--} \to 0$ as $L \to \infty$. The results indicate that the system has a two-fold TGSD. (b) For 45°-tilt compactification. The state in the $(-,-)$ sector has higher energy, and is separated from the states in the other three sectors $(+,+), (+,-)$, and $(-,+)$, which are degenerate. [Note that $(+,-)$ and $(-,+)$ sectors have identical energy spectra due to the C_4 rotation symmetry of the lattice.] 82

4·9 QMC results of energies in 4 topological sectors for (a) 0°-tilt with system size $L = 13$ where only the sectors (+,-) and (-,+) are compatible with zero magnetization. (b) 45°-tilt with system size $L = 5$, where the TGSD remains three as the even size system, but the degenerate sectors are (+,-) (-,+) and (-,-). N_s denotes the total number of stars on the lattice. 83

4·10 ED results for the energy of the lowest states in each topological sectors with $m = 0$ for different compactifications. (a) $a = 2, b = 1, L = 2$. (b) $a = 3, b = 1, L = 1$ (c) $a = 3, b = 2, L = 1$. 85

4·11 Mapping between topological sectors in 0°-tilt (right side) and 45°-tilt (left side) compactifications. The ground state manifold is depicted with the red frames, while topological sectors with excited lowest energy states are depicted with gray dashed frames. We assume existence of non-local and non-unitary tunneling operators, $T_x^{45^\circ}$ (red arrows) and $T_y^{45^\circ}$ (dashed black arrows), that in the 45°-tilt case take the state $|{+}{+}\rangle$ to states $|{-}{+}\rangle$ and $|{+}{-}\rangle$, respectively. Simultaneous application of both tunneling operators to $|{+}{+}\rangle$ annihilates the state, and therefore $|{-}{-}\rangle$ does not belong to the ground state manifold. In the 0°-tilt case, assuming the same orientation of the tunneling operators with respect to the microscopic details of the lattice, both $T_x^{45^\circ}$ and $T_y^{45^\circ}$ take state $|{+}{+}\rangle$ to $|{-}{-}\rangle$, and hence states $|{+}{-}\rangle$, $|{-}{+}\rangle$ remain out of the ground state manifold. 96

4·12 Spin-spin correlation functions in the x- and 45°-directions ($C(r)$ and $C_d(r)$, respectively) are shown for different system sizes, L. The results are presented from left to right for the $(-,-)$, $(+,+)$, and $(+,-)$ topological sectors. The correlation functions decay to zero rapidly, indicating that the system is gapped for all topological sectors. 97

4·13 Spin-spin correlation functions in the topological sectors $(+,+)$, $(+,-)/(-,+)$ and $(-,-)$ for the 45°-tilt setup. All the results shows a fast decaying within the order of two lattice sites for all system sizes L. 98

4·14 Intensity plot of the star-star correlation $\left\langle \mathcal{A}_{s=(0,0)}\, \mathcal{A}_{s'=(x,y)} \right\rangle$, indicating translational symmetry breaking. (a) Result for 0°-tilt compactification, in the sector $(-,-)$ and with $M_z = 0$. The system size is $L = 16$. (b) Result for 45°-tilt compactification, in the sector $(+,+)$ and with $M_z = 0$. The system size is $L = 12$. 99

4.15 A proposed physical realization of the star term $\mathcal{A}_s$ in the $U(1)$ toric code lattice Hamiltonian. The center "waffle" is highlighted as an example. It is composed of intersecting superconducting wires coupled by Josephson junctions. The junctions in the diagonal (red) denote π couplings. Vertical wires (blue) are "matter" degrees of freedom labeled by phase ϕ_n. Horizontal wires (gold) are "gauge" degrees of freedom with phases θ_i. Only the gauge degrees of freedom (black) couple to other, neighboring, waffles. 100

List of Abbreviations

CGS	Combinatorial Gauge Symmetry
ED	Exact Diagonalization
GSD	Ground State Degeneracy
IR	infrared
NISQ	Noisy Intermediate-Scale Quantum
PBC	periodic boundary condition
QMC	Quantum Monte Carlo
SSE	Stochastic Series Expansion
TFIM	transverse field Ising model
TGSD	Topological Ground State Degeneracy
UV	ultraviolet

Chapter 1

Introduction

Understanding the behavior of quantum spin systems has been a key research area in condensed matter physics for several decades. Quantum spin systems exhibit a rich variety of phases, and the study of their emergent properties has led to profound insights into the fundamental principles of quantum mechanics. One of the most intriguing aspects of quantum spin systems is the emergence of topological order, a phenomenon that has attracted significant attention in recent years [1].

The concept of topological order is not only of fundamental importance but also holds promise for applications in quantum computing and quantum information theory. These special quantum phases exhibit exotic properties such as their topological ground state degeneracy (TGSD) and the excitation content that cannot be captured by conventional Ginzburg-Landau theory. A significant challenge we face today is that qubits, the fundamental units of quantum computers, are subject to noise and have short coherence times. This places us in the era of Noisy Intermediate-Scale Quantum (NISQ) computing, where quantum devices have a limited "lifetime" before they decohere, rendering them unsuitable for meaningful calculations. One promising avenue toward achieving fault-tolerant quantum devices is through systems exhibiting topological phases.

The reason is that topological phases are robust against local perturbations [1, 2, 3, 4, 5]. Since most of the noise sources are local, the properties of topological phases are thus essential for achieving fault-tolerant quantum computation. Therefore, understanding the underlying mechanisms that give rise to topological order is crucial for advancing both our theoretical understanding and practical applications in quantum information science. The study of topological order in quantum spin systems is closely linked to the concept of gauge symmetries. Gauge symmetries play a pivotal role in modern theoretical physics, ranging from the Standard Model of particle physics to condensed matter systems.

In this dissertation, we aim to focus on the study of quantum spin systems with local gauge symmetries. In particular, the systems we consider cannot be exactly solved but are sign-problem free, enabling large-scale numerical studies using unbiased methods such as quantum Monte Carlo (QMC). In Chapter 2, we first provide an overview of local gauge symmetry and topological phase to establish essential knowledge for the following explorations. We then delve into the detailed investigations of two specific quantum spin systems with local Z_2 gauge symmetries in search of topological orders and other properties of interest in the systems.

With local gauge symmetry in mind, Kitaev constructed one of the most influential quantum spin systems, dubbed Kitaev's toric code. The model is simple and exactly solvable, but it requires the inclusion of four-body interactions, which are not commonly found in nature. Recent theoretical proposals have come up with a solution. By combining combinatorial symmetry with auxiliary spins, local gauge symmetry can be constructed with only two-body interactions, and the existence of topological order phases has been theoretically predicted. In Chapter 3, we give an overview of this idea, introduce the concept of combinatorial gauge symmetries, and then focus on an in-depth study of the proposed theoretical model using numerical methods. Our primary goal is to verify the theoretical prediction of the existence of topological order. We also explore other properties of the system, such as phase diagrams, properties of phase transitions, as well as the low-energy excitations of the system.

In Chapter 4, we focus on another quantum spin system with local Z_2 gauge symmetry, where we generalize the well-known Kitaev's toric code by enriching the system with global U(1) symmetry. By introducing global U(1) symmetry, the model is no longer exactly solvable. We study the system by developing a new kind of update algorithm in the context of quantum Monte Carlo simulation. Through these explorations, we aim to advance our understanding of the fascinating phenomena that arise in this system, such as Hilbert space fragmentation, topological order, and the discovery of an unconventional type of ultraviolet/infrared (UV/IR) mixing, where the property of topological phase, such as ground state degeneracy (GSD), depends on the lattice compactification. In the end of this chapter, we also discuss the realization of this model via CGS construction, which can be implemented experimentally in superconducting quantum wires.

Finally, in Chapter 5, we summarize our discoveries in studying these two systems and provide insights into possible future research directions. This includes potential extensions of our work, exploration of related systems, and open questions in the field. We anticipate that our research will stimulate further investigations in the exciting intersection of local gauge symmetry and topological order.

Chapter 2

Overview of Topological Phases and Symmetries

2.1 Z_2 Local Gauge Symmetry in Spin systems

To provide an introduction to the realization of Z_2 local gauge symmetry in a spin system, particularly in the context of a spin-1/2 system, we begin by examining Kitaev's toric code [6]. In this model, the Hamiltonian is expressed as the sum of commuting projectors, making it exactly solvable. This allows for analytical insights into ground state properties, excitations, and the presence of topological order.

Subsequently, we extend our exploration to a slight modification of this model known as the Z_2 lattice gauge model, where one of the terms is replaced by a uniform transverse field. This model is highly relevant and serves as the foundation for understanding more complex models in the following chapters. Although this modified model is no longer exactly solvable, it exhibits a transition between a phase with topological order and another trivial paramagnetic phase as the strength of the transverse field is tuned.

2.1.1 Toric code

To start, Consider a square lattice with Ising degree of freedom sitting on each leg with periodic boundary conditions. The Hamiltonian of the toric code comprises two types of terms: "star" operators and "plaquette" operators.

The star term is defined as the product of 4 Pauli-Z operators acting on legs l

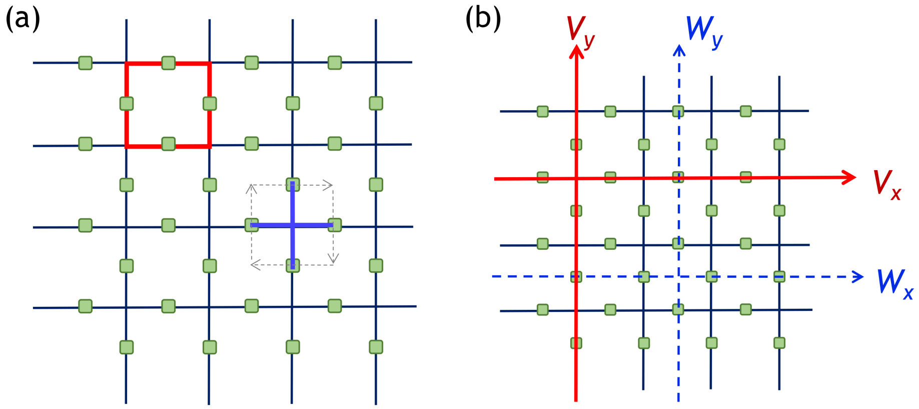

Figure 2·1: (a) The square lattice that defines the toric code. The blue crosses represent the star operator A_s, defined as the product of σ_z operators along the dashed-arrow closed-loop surrounding a 'star', while the red boxes represent the plaquette operator B_p, defined as the product of 4 σ_x operators on the edges of the box. (b) When putting on a torus, 4 additional operators $W_{x,y}$ defined as product of σ_z along the line and $V_{x,y}$ defined as product of σ_x are also conserved.

belonging to a lattice site s, denoted as $A_s = \prod_{l \in s} \sigma_l^z$, while the plaquette term is defined as the product of 4 Pauli-X operators acting on legs l belonging to a plaquette p (dual lattice site), denoted as $B_p = \prod_{l \in p} \sigma_l^x$, as shown in 2·1(a). It's worth noting that here, we choose the star operator to be a product of Pauli-Z operators, and the plaquette operator as a product of Pauli-X operators. In general, these two definitions are interchangeable without affecting the underlying physics. In the context of quantum information, these star and plaquette operators are sometimes referred to as stabilizers, as they play a role in "stabilizing" the topological ground states.

The toric code Hamiltonian is defined as the sum of star and plaquette terms,

$$H = -\lambda_A \sum_s A_s - \lambda_B \sum_p B_p. \tag{2.1}$$

One can easily check that all the operators A_s and B_p commute with each other. In other words, $[A_s, B_p] = 0$, for all s and p since nearby star and plaquette always overlap with even number of sites. With periodic boundary condition (PBC), 4 additional loop-operators, $W_{x,y}$ and $V_{x,y}$, defined along the shortest non-contractible loops that wind around the torus in the x and y directions are also conserved as shown in Fig. 2·1(b). It is important to notice that $[W_{x,y}, V_{x,y}] \neq 0$, since they intersect with each other on a single site, and at the intersection $[\sigma_x, \sigma_z] \neq 0$.

For any local closed loop γ composed of a sequence of connected links, the loop operator

$$V(\gamma) = \prod_{\ell \in \gamma} \sigma_\ell^x \tag{2.2}$$

commutes with the Hamiltonian, $[H, V(\gamma)] = 0$, and can be represented as a product of plaquette operators B_p enclosed by γ. Similarly, closed loop defined as product of σ_z on the dual lattice $\tilde{\gamma}$

$$W(\tilde{\gamma}) = \prod_{\ell \in \tilde{\gamma}} \sigma_\ell^z \tag{2.3}$$

also commutes,$[H, W(\tilde{\gamma})] = 0$, which can be represented as a product of star operators A_s enclosed by $\tilde{\gamma}$. Despite the possibility of finding many more different commuting operators in the system, only $M = 2 + 2(L_xL_y - 1)$ such operators are independent. This count includes $2(L_xL_y - 1)$ for both stars and plaquettes, with the subtraction of one accounting for the fact that the product of all stars/plaquettes is equivalent to the identity. The additional count of 2 arises from the non-contractable loops $W_{x,y}$ (or $V_{x,y}$), where one can only choose either one set of them due to the non-commutativity of $[W_{x,y}, V_{x,y}] \neq 0$.

One has the freedom to choose which M operators will characterize the symmetry sectors. For simplicity, we consider the operators A_s, B_p, W_x, W_y as our independent symmetry operators that simultaneously commute with the Hamiltonian. Notice that $M = 2 + 2(L_xL_y - 1) = 2L_xL_y$, which is the same as the total number of spins in the system. These operators have eigenvalues (quantum numbers) = ±1, thus enabling us to block diagonalize the Hilbert space into 2^M symmetry sectors. An interesting and important property is that the number of symmetry sectors is the same as the dimension of the Hilbert space, meaning that each symmetry sector has only one unique state.

Eigenstates and Topological Ground State Degeneracy

After introducing the conserved quantities, we are now ready to construct the explicit eigenstates of the toric code. We will begin with a single operator A_s. Since $A_s^2 = I$, the eigenstates $|q_s\rangle$ of operator A_s can be constructed starting from a classical representative state $|rep\rangle$ via the expression:

$$|q_s\rangle = (1 + q_s A_s)\,|rep\rangle\,, \tag{2.4}$$

where $q_s = \pm 1$ is the eigenvalue of operator A_s. It can be verified that $A_s\,|q_s\rangle = q_s\,|q_s\rangle$, which confirms that $|q_s\rangle$ is indeed the eigenstate.

We can extend the construction by considering all the M symmetry operators mentioned above. In this case, the eigenstate of the toric code can be written as:

$$|\vec{q}\rangle = (1 + w_x W_x)(1 + w_y W_y)\prod_p (1 + q_p B_p)\prod_s (1 + q_s A_s)\,|rep\rangle\,, \tag{2.5}$$

Here, $\vec{q} \equiv \langle w_x, w_y, \{q_p\}, \{q_s\}\rangle$ is the set of binary quantum numbers associated with each symmetry operator. As mentioned previously, since there is only one state associated with each quantum number set, one can start with any classical configuration that compatible with corresponding quantum number set $\vec{q}$ as a representative state. By following this construction, all the eigenstates in the system can be acquired.

Now let's examine the ground state of the toric code Hamiltonian Eq. 2.1. It is evident that the ground state should satisfy $A_s = q_s = +1$ and $B_p = q_p = +1$ to

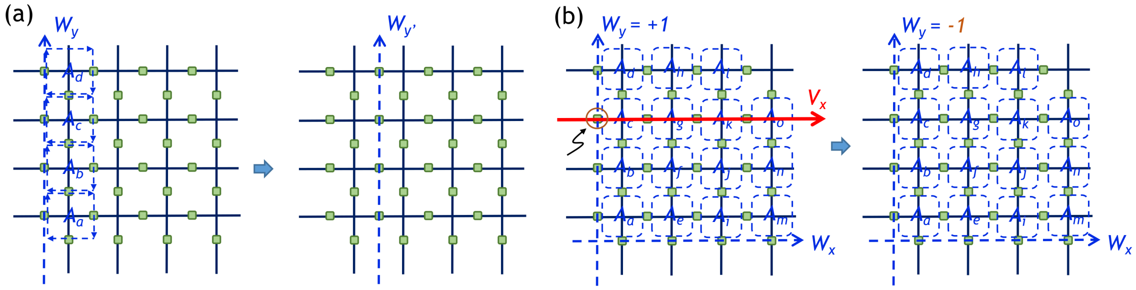

Figure 2·2: (a) An example illustrating the conversion of a non-contractible operator W_y to $W_{y'}$ by taking the product with a series of local star operators. (b) The action of the non-contractible loop operator V_x along the x-direction, as indicated by the red arrow. This operator passes an even number of spins for elementary star operators, intersecting one spin of the non-contractible loop W_y, thus causing a flip in the quantum number.

minimize the energy. In this case, the ground state is given by:

$$|w_x, w_y\rangle = (1 + w_x W_x)(1 + w_y W_y) \left[\prod_p (1 + B_p) \prod_s (1 + A_s) |rep\rangle \right]. \tag{2.6}$$

This results in 4 degenerate states characterized by two non-contractible loop operators W_x and W_y. Therefore, the ground state exhibits a 4-fold degeneracy with $w_x = \pm 1$ and $w_y = \pm 1$. We will refer to these as topological operators and topological quantum numbers in the following.

These topological states exhibit interesting properties. First, all the non-contractible loops $W(\tilde{\gamma})$ have the same quantum number. This can be observed from the fact that any non-contractible loop along the x- or y-direction can be constructed by combining local A_s operators with $W_{x,y}$ operators. As illustrated in Fig. 2·2(a), by combining with all the local A_s operators, one can transform W_y into $W_{y'}$. Since $A_s = +1$ for the ground state, the quantum numbers w_y and $w_{y'}$ are equal. Secondly, it is impossible to transition between these topological ground states using local operations. To go from one ground state to another, one must utilize the conjugate operator $V_{x,y}$, which flips the sign of the topological operators while leaving the local stars invariant. As demonstrated in Fig. 2·2(b), the action of V_x (indicated by the red arrow) flips the quantum number of W_y. It is noteworthy that V_x always overlaps two sites on the stars A_s it traverses, and therefore, the quantum number of A_s remains unchanged.

Fractional Excitations

Next, let's examine the excitations in the Z_2 ordered phase. There are two distinct types of excitations in this phase. The first type involves acting on a single site with a σ_z operator, creating a pair of m anyons, sometimes referred to as visons. These anyons are represented by the flipping of two plaquette operators B_p (denoted by the red squares) as shown in Fig.2·3(a). The second type of excitation occurs when we act on a single site with a σ_x operator, creating a pair of e anyons, also known as spinons. These anyons are represented by the flipping of two local star operators A_s as shown in Fig.2·3(b).

It's worth noting that the creation of spinon excitations does not alter the quantum numbers associated with B_p since σ_x commutes with the plaquette operators. However, it's essential to emphasize that σ_x does not commute with the Hamiltonian (H). Similarly, the creation of vison excitations does not affect the quantum numbers of A_s. Furthermore, in systems with periodic boundary conditions (PBC), visons and spinons must be created in pairs. Creating a pair of spinons results in two violations of star operators, with an associated energy gap of $\Delta_e = 4\lambda_A$. Creating a pair of visons gives rise to an energy gap of $\Delta_m = 4\lambda_B$. Due to the model's simplicity, both spinon and vison excitations exhibit a flat band in momentum space, indicating their degeneracy. This degeneracy implies that these excitations are localized and immobile.

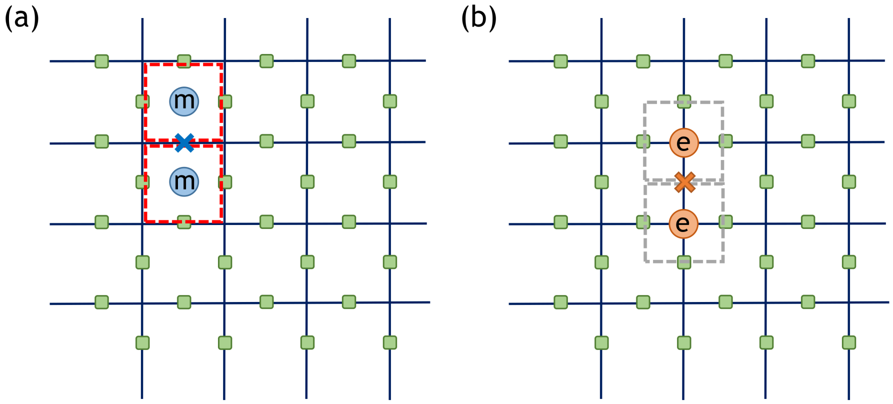

Figure 2·3: (a)The excitation generated by acting a σ_z operator that creates two m excitation (visons) on the dual lattice, which represented as flipping two nearest-neighbor plaquette operators.(b)The excitation generated by acting a σ_x operator that creates two e excitation (spinons) on the lattice site, which represented as flipping two nearest-neighbor star operators.

2.1.2 Z_2 lattice gauge model

In the case of the toric code, we observe that both star and plaquette operators are conserved. Now, let's consider a simple generalization of the model where the plaquette terms are replaced with terms that commute with the plaquette operators (thereby preserving the local Z_2 gauge symmetry), but these terms no longer commute with the star operators.

The simplest modification involves introducing a uniform transverse field, defining the Hamiltonian as follows:

$$H = -\lambda_A \sum_s A_s - g \sum_i \sigma_i^x. \tag{2.7}$$

This Hamiltonian corresponds to the quantum Z_2 gauge theory [2, 7]. In this context, we can consider B_p as the gauge operators. Notably, the transverse field commutes with the plaquette terms B_p but does not commute with the star operators.

It is shown by Wegner [2] that this model exhibits two gapped phases separated by a phase transition at g_c. In the regime where $g \gg \lambda_A$, all spins are aligned in the x-direction, representing a trivial paramagnetic phase. In this configuration, consider a closed loop defined as the product of Pauli-Z operators, denoted as $W(\gamma) = \prod_{l \in \gamma} \sigma_l^z$. Since all spins are polarized in the x-direction, this loop configuration is energetically disfavored. This phase is referred to as the 'confined' phase. In contrast, when $\lambda_A \gg g$, the loops can fluctuate, leading to the 'deconfined' phase.

Importantly, it's worth noting that this model is dual to the square lattice Ising model. To demonstrate this duality, consider mapping the star term $A_s \to \mu^z$ as a new Ising degree of freedom. The action of the transverse field effectively flips two neighboring stars, behaving as an effective XX coupling. Under this mapping, the model can be expressed as:

$$\tilde{H} = -\lambda_A \sum_s \mu_s^z - h \sum_{i,j} \mu_i^x \mu_j^x, \tag{2.8}$$

which is the Hamiltonian of the transverse field Ising model on a square lattice. Consequently, the phase characterized by dual Ising order corresponds to the confined phase, while the phase with Ising disorder corresponds to the deconfined phase.

2.1.3 Toric code on a ladder

We now turn to consider the implementation of the toric code in a ladder geometry, as shown in Figure 2·4. The Hamiltonian is defined as follows:

$$H = -J \sum_s A_s^x - \lambda_B \sum_p B_p^z \tag{2.9}$$

Where $A_s^x = \prod_{i \in s} \sigma_i^x$ represents the star term, and $B_p^z = \sigma_{p,\mathrm{top}}^z \sigma_{p,\mathrm{bottom}}^z$; here, σ denotes the Pauli operators. The lattice geometry is illustrated in Figure 3·1. Note that in this context, we redefine the star term as a product of X, and the plaquette term in a ladder system is simplified to a product of two Zs on a plaquette p. To eliminate ambiguity in the definition of the star term, we consistently adopt the definition that an excitation on the plaquette, denoted as a vison (with $B_p^z = -1$), and an excitation on the site, referred to as a spinon (with $A_s^x = -1$).

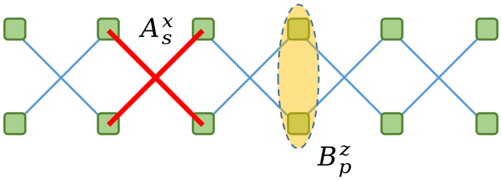

Figure 2·4: The toric code on a ladder has its star term, A_s^x, defined as the product of σ^x for four spins on a site, depicted as a red star. The plaquette term B_p^z is a symmetry operator, defined as the product of two σ^z acting on plaquette p.

Again, we observe that all operators commute with each other, allowing the system to be block-diagonalized. The ground state resides in the sector with $A_s^x = +1$ and $B_p^z = +1$. Ref. [8] demonstrates that introducing dynamics with a uniform $-\Gamma \sum_l \sigma_l^z$ field imparts dynamics to the spinons. This mapping reveals that spinon excitations can be mapped to a free fermion model. The vison excitation effectively 'cuts' the chain due to destructive interference arising from the mutual statistics of spinons and visons.

Here, we propose a different approach to interpret this property. We begin by categorizing the system's Hilbert space based on the symmetry operators B_p^z. For each B_p^z at plaquette p, the local basis can be divided into two groups: $B_p^z = \pm 1$. It's important to note that on a ladder, the plaquette term consists of a product of two Zs. Thus, one can also define another operator as a product of Pauli-X, $B_p^x = \sigma_{p,\text{top}}^x \sigma_{p,\text{bottom}}^x$, which also commutes with B_p^z. In fact, the star term can be expressed as a product of two neighboring X-plaquettes B_p^x, such that $A_s^x = B_s^x B_{s+1}^x$. With $B_p^z = +1$, the local space is spanned by $|\uparrow\uparrow\rangle, |\downarrow\downarrow\rangle$. Conversely, if $B_p^z = -1$, the local space is spanned by $|\uparrow\downarrow\rangle, |\downarrow\uparrow\rangle$, as illustrated in Fig. 2·5.

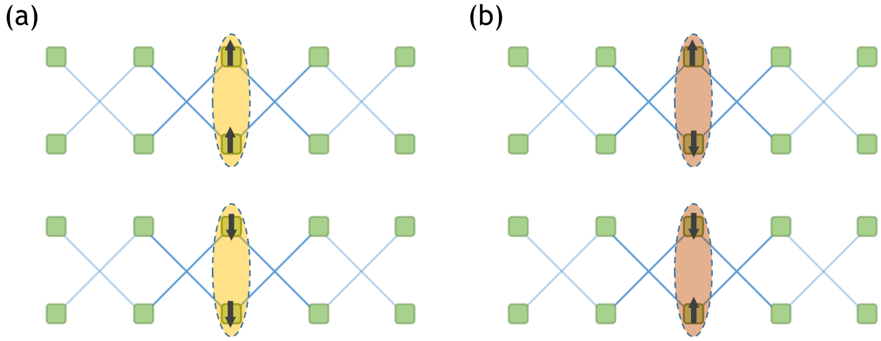

Figure 2·5: The quantum number of B_p^z divides the local Hilbert space into two parts: (a) With $B_p^z = +1$, the local space is spanned by $|\uparrow\uparrow\rangle, |\downarrow\downarrow\rangle$. (b) With $B_p^z = -1$, the local space is spanned by $|\uparrow\downarrow\rangle, |\downarrow\uparrow\rangle$.

Consider first the Hamiltonian with only the star terms, which is also referred to as the classical toric code:

$$H = -J \sum_s A_s^x. \tag{2.10}$$

As indicated previously, since B_p^z are good quantum numbers, we can block-diagonalize the Hamiltonian into symmetry sectors with the quantum number set $\vec{q} = B_p^z$. The star operator A_s^x effectively flips $|\uparrow\uparrow\rangle \leftrightarrow |\downarrow\downarrow\rangle$ (or $|\uparrow\downarrow\rangle \leftrightarrow |\downarrow\uparrow\rangle$ if the instance $B_p^z = -1$ at p). Thus, considering the mapping for $B_p^z = +1$:

$$\begin{aligned} |\uparrow\uparrow\rangle &\rightarrow |0\rangle \\ |\downarrow\downarrow\rangle &\rightarrow |1\rangle\,; \end{aligned} \tag{2.11}$$

and for $B_p^z = -1$,

$$\begin{aligned} |\uparrow\downarrow\rangle &\rightarrow |0\rangle \\ |\downarrow\uparrow\rangle &\rightarrow |1\rangle\,. \end{aligned} \tag{2.12}$$

Since the star term can be written as a product of $B_s^x B_{s+1}^x$, if we define a new Ising degree of freedom as $\tau_s^x = B_s^x$, then the Hamiltonian can be rewritten as

$$H_{\text{eff}} = -J \sum_s \tau_s^x \tau_{s+1}^x, \tag{2.13}$$

from which we can see that the classical toric code is dual to the classical ferromagnetic (FM) Ising model (in the x-basis). It is noteworthy that the above mapping works for all the symmetry sectors characterized by the $\{B_p^z\}$ quantum number set. In other words, this effective model is applicable to sectors with any number of vison excitations. Adding the plaquette terms to the Hamiltonian simply shifts each symmetry sector by a constant (where the energy shift depends on the number of visons in a given symmetry sector). A single σ^z operation, which flips $\tau_s^x \to -\tau_s^x$, can excite a pair of spinons. In the dual model, this spin flip creates domain walls. Therefore, the spinon excitation can be interpreted as a domain wall in the dual model.

Next, we consider adding dynamics to the system by examining the Hamiltonian with a uniform field (which corresponds to the Z_2 lattice gauge model on a ladder):

$$H = -J \sum_s A_s^x - \Gamma \sum_l \sigma_l^z. \tag{2.14}$$

While the uniform field no longer commutes with the star terms, the plaquette operators B_p^z still commute with H as good quantum numbers. We can slightly rewrite the Hamiltonian by defining an operator $\hat{Z}_p = \sigma_{p,\text{top}}^z + \sigma_{p,\text{bottom}}^z$:

$$\begin{aligned} H &= -J \sum_s A_s^x - \Gamma \sum_p \left(\sigma_{p,\text{top}}^z + \sigma_{p,\text{bottom}}^z\right) \quad (2.15) \\ &= -J \sum_s A_s^x - \Gamma \sum_p \hat{Z}_p. \quad (2.16) \end{aligned}$$

To attempt the dual mapping, we observe that $\{\hat{Z}_p, B_p^x = \tau_p^x\} = 0$, indicating that they anti-commute with B_p^x. More importantly, we notice that $\hat{Z}_p$ annihilates the

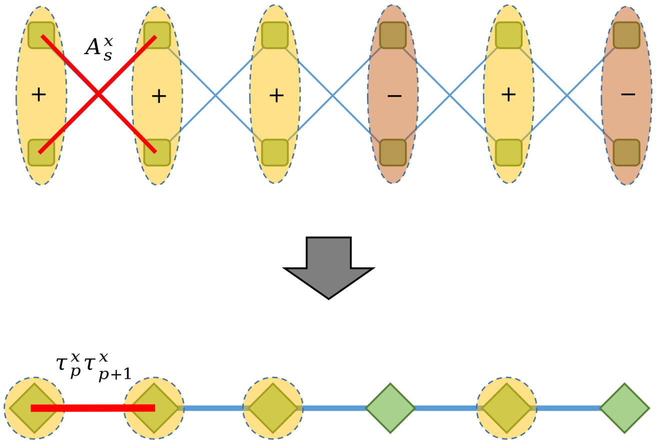

Figure 2·6: The mapping to the transverse field Ising model in the sector with two visons (indicated by $B_p^z = -1$ at the locations shown in light orange) transforms the red star operator into the nearest neighbor ferromagnetic interaction $\tau_p^x \tau_{p+1}^x$. Furthermore, the operator $\hat{Z}_p$ is mapped to τ_p^z only at locations where $B_p^z = +1$.

basis state when $B_p^z = -1$,

$$\hat{Z}_p \left|\uparrow\downarrow\right\rangle = 0 \tag{2.17}$$

$$\hat{Z}_p \left|\downarrow\uparrow\right\rangle = 0; \tag{2.18}$$

and when $B_p^z = +1$

$$\hat{Z}_p \left|\uparrow\uparrow\right\rangle = 2\left|\uparrow\uparrow\right\rangle \tag{2.19}$$

$$\hat{Z}_p \left|\downarrow\downarrow\right\rangle = -2\left|\downarrow\downarrow\right\rangle. \tag{2.20}$$

This implies that we can map $\hat{Z}_p = 2\tau_p^z$ as a transverse field at the plaquette with $B_p^z = +1$, where the effective Hamiltonian resembles the Transverse Field Ising Model (TFIM) with the field only acting on sites where $B_p^z = +1$:

$$H = -J\sum_p \tau_p^x \tau_{p+1}^x - 2\Gamma \sum_{p\in B_p^z=+1} \tau_p^z, \tag{2.21}$$

as illustrated in Fig. 2·6.

Chapter 3

Z_2 Topological Order and First-Order Quantum Phase Transitions

Topological quantum states of matter are of central focus in modern condensed matter physics. One of the main features of strongly-interacting systems with gapped topological order is that they can present degenerate ground states. This degeneracy cannot be lifted by the action of local perturbations, and hence this property makes such systems perfect candidates for building stable (topological) qubits. Several theoretical models have been proposed to realize gapped topologically ordered states. For instance, the toric code [6] and dimer models on non-bipartite lattices [9, 10] host quantum spin liquid (QSL) phases that possess Z_2 topological order. In both these examples, the Hamiltonians contain multi-body interactions, making it a challenge to encounter materials realizing these phases or to realize them in artificial structures.

Attempts have been made to construct models with simpler interactions that can host gapped QSLs. A rare successful example is the cluster charging model of bosons on the kagome lattice [11, 12, 13], which has been shown theoretically and numerically to host a Z_2 quantum spin liquid, in a system with only two-body interactions. However, these two-body interactions are of the XXZ type, which are not easily implementable in, say, programmable quantum devices. Moreover, the Z_2 gauge symmetry in this model is only emerging, i.e., it exists in the effective model derived in perturbation theory, but it is not an exact symmetry of the original Hamiltonian.

Recently, a construction for which the Z_2 gauge symmetry is exact was proposed on a variant of the transverse field Ising model (TFIM), utilizing only simple two-body ferromagnetic and antiferromagnetic ZZ interactions [14]. Monomial (matrix) transformations that correspond to combinations of spin flips and permutations play a central role in the construction, thus dubbed combinatorial gauge symmetry. Because the construction utilizes only ZZ interactions (of both signs) and a transverse field, the model can be easily implemented, for example, with current Noisy Intermediate-Scale Quantum (NISQ) technology using flux-based superconducting qubits, or other types of quantum computer architectures that provide similar interactions on qubits. The model has already been successfully implemented on a D-wave quantum device in a recent experiment [15].

In this chapter, we present a quantitative and detailed study of the combinatorial Z_2 gauge model originally proposed in Ref. [14]. We first give a brief introduction to the model with combinatorial Z_2 gauge symmetry. The model realizes the Z_2 gauge symmetry through monomial transformations and effectively realizes the 4-body interaction term as the star term in the classical version of the toric code. Two different types of quantum fluctuations are introduced while preserving the gauge symmetry: a transverse field acting on the gauge spins and a XX ferromagnetic interaction between the gauge spins, respectively. We provide numerical results on both models obtained from quantum Monte-Carlo (QMC) simulations with the Stochastic Series Expansion (SSE) method as well as exact diagonalization (ED). In both cases, we find that the system exhibits a Z_2 topologically ordered phase separated by a first-order transition from either a paramagnetic phase (model-X) or a ferromagnetic phase (model-XX).

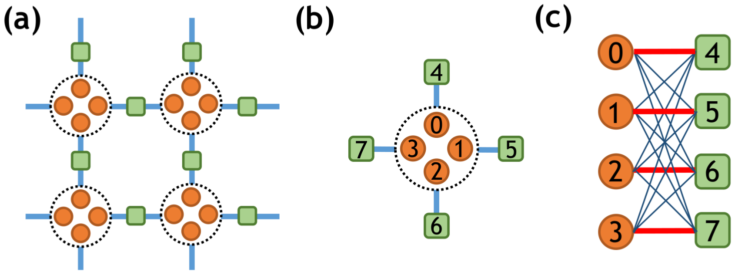

Figure 3·1: (a) The arrangement of two species of Ising spins on a square lattice. Gauge spins (green squares) reside on the links and four matter spins (orange dots) occupy each site of the square lattice. (b) The vertex unit and the interactions between spins. The interactions between gauge-matter spins within a single unit are defined by the Hadamard matrix $\mathbf{W}$ in Eq. (3.3). For clarity, the couplings are depicted on a deformed cell in panel (c), where the ferromagnetic and antiferromagnetic couplings are shown as thin blue lines and bold red lines, respectively.

3.1 Local Z_2 Gauge Symmetry with Two-body terms

3.1.1 Z_2 Combinatorial Gauge Symmetries

We start with a model featuring $S = 1/2$ spins residing on both the sites and the links of a square lattice, and we illustrate how combinatorial gauge symmetry is realized. In order to achieve local Z_2 gauge symmetry with only two-body interactions, we arrange the spins with both ferromagnetic and antiferromagnetic couplings in a pattern as shown in Fig. 3·1(a). For each star (or vertex) s of the lattice, we place four ”matter” spins μ (the orange dots inside the circles representing the lattice sites) and four ”gauge” spins σ (green squares) on the links of the star. One such star with its total of eight spins is depicted in Fig. 3·1(b) along with a labeling scheme. The Hamiltonian of the system is written as

$$H = \sum_s H_s + H^{\sigma}_{\text{kin}} \,, \tag{3.1}$$

where H^{σ}_{kin} is the kinetic term involving only the σ^x component of the gauge spins (on all links), and at each star s we define a local Hamiltonian on its eight spins [14]

$$H_s = J \sum_{a\in s} \left(\sum_{j\in s} W_{aj}\sigma^z_j \right) \mu^z_a - \Gamma_m \sum_{a\in s} \mu^x_a \,. \tag{3.2}$$

Here the sums with j and a indices include the four matter spins σ^z_j and the four gauge spins μ^z_a, respectively. Notice that H_s contains a transverse field only on the matter spins. The ZZ couplings between the gauge and matter spins have magnitude J and signs controlled by the Hadamard matrix W,

$$\mathbf{W} = \begin{pmatrix} +1 & -1 & -1 & -1 \\ -1 & +1 & -1 & -1 \\ -1 & -1 & +1 & -1 \\ -1 & -1 & -1 & +1 \end{pmatrix} . \tag{3.3}$$

Fig. 3·1(c) depicts these signs; the interaction between a gauge spin and its nearest matter spin is antiferromagnetic (bold red line) while its interaction with the other 3 matter spins are ferromagnetic (thin blue line).

The Hamiltonian in Eq. (3.1) possesses combinatorial Z_2 gauge symmetry if the H_s terms are of the above form, and if only the σ^x component of the gauge spins enters in H^{σ}_{kin}. The transformations

$$\sigma^z_i \to \sum_j \mathbf{R}_{ij}\, \sigma^z_j \tag{3.4a}$$

$$\mu^z_b \to \sum_a \mu^z_a\, \mathbf{L}^{-1}_{ab} \tag{3.4b}$$

leave the spin commutation relations invariant if $\mathbf{L}$ and $\mathbf{R}$ are monomial matrices, i.e., generalized permutation matrices with a ±1 entry in each line or column in the case of the group Z_2. The transformations correspond to combinations of rotations by 0 (+1 entry) or π (-1 entry) around the x-axis, followed by a permutation of the indices.

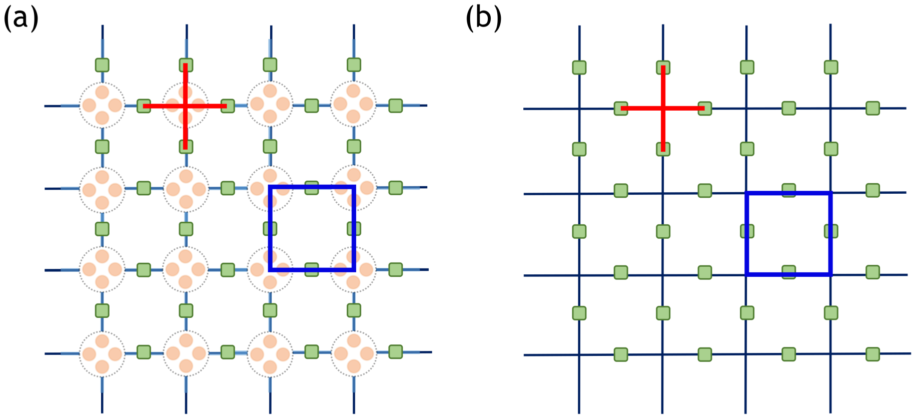

Figure 3·2: Connection between the model in our studies to the Z_2 gauge theory. The red star in (a) represents the expanded 4-body interacting term that is equivalent to the star term $\prod \sigma^z$ of the Z_2 gauge model in (b). The blue plaquette in (a) represents the local combinatorial gauge generator G_p by analogy with the local gauge generator B_p of the Z_2 gauge model defined as $\prod \sigma^x$ of the 4 spins around a plaquette in (b).

A local gauge symmetry is generated by flipping gauge spins on closed loops around the elementary plaquettes, together with accompanying transformations on matter spins. Flipping the gauge spins around the loop corresponds to choosing $\mathbf{R}$ matrices for each s traversed, with an even number of -1 entries associated with the links visited. For each such $\mathbf{R}$, there is a corresponding monomial matrix $\mathbf{L} = \mathbf{W}\,\mathbf{R}\,\mathbf{W}^{-1}$ [14]. These pairs of monomial $\mathbf{R}$ and $\mathbf{L}$ matrices are such that $\mathbf{W} = \mathbf{L}^{-1}\,\mathbf{W}\,\mathbf{R}$, and thus the transformation in Eq. (3.4) leaves the ZZ part of the Hamiltonian invariant. Moreover, since in H_s the transverse field on the μ^x is the same on all $a \in s$, the permutation action of the monomial $\mathbf{L}$ also leaves these terms unchanged. Hence, H_s is invariant under the monomial transformation with $\mathbf{L}$ and $\mathbf{R}$. Finally, since $\mathbf{R}$ is diagonal and only σ^x enters in H^{σ}_{kin}, this kinetic term is also invariant. For each such loop, we have a Z_2 symmetry of the Hamiltonian in Eq. (3.1). This local Z_2 gauge symmetry is *exact* for any value of the parameters in the Hamiltonian Eq. (3.1). We can obtain further intuition by connecting to the more familiar formulation of the Z_2

gauge theory [2, 7] as introduced in Chapter 2 in certain limits.

Consider the effective Hamiltonian for the H_s terms when their energy scales are larger than those in H^{σ}_{kin}; in this regime, one can diagonalize H_s by fixing the σ^z_i around the star and treating the problem as that of a paramagnet for the matter spins μ_a. The result is an effective Hamiltonian for the lowest states that take the form of a four-spin interaction among the gauge spins [14]:

$$H^{\text{eff}}_s = -\gamma - \lambda \prod_{i \in s} \sigma^z_i \ , \tag{3.5a}$$

where the parameters γ and λ are given by

$$\gamma = \frac{1}{2}\left(\sqrt{\Gamma^2_m + 16J^2} + 3\Gamma_m + 4\sqrt{\Gamma^2_m + 4J^2}\right) \tag{3.5b}$$

$$\lambda = -\frac{1}{2}\left(\sqrt{\Gamma^2_m + 16J^2} + 3\Gamma_m - 4\sqrt{\Gamma^2_m + 4J^2}\right) . \tag{3.5c}$$

Notice that the effective H^{eff}_s is, up to a constant shift, the same as the star term $A^z_s = \prod_{i \in s} \sigma^z_i$ that appears in the toric code [6] and the Z_2 lattice gauge model [2, 7] as introduced previously in Chapter 2. We depict in Fig. 3·2(a) the star term in our model, juxtaposed to the star term represented in the toric and Z_2 gauge models in Fig. 3·2(b) as the product of four spins on the red cross. The manifold of other states in our model, those beyond the effective term, are separated by a scale Γ_m. Thus, in the limit $\Gamma_m \to \infty$, higher energy sectors are projected out, and the system Hamiltonian asymptotically becomes the exact star term of the toric code. (We remark that the limit $\Gamma_m \to \infty$ here simply serves the purpose of sending selected excited state sectors to infinitely high energies; the effective Hamiltonian (3.5a) is a non-perturbative description of the states that do not float to infinity in the $\Gamma_m \to \infty$ limit, and the states in this manifold are not affected by the limit.)

In Chapter 2, we introduced the Z_2 lattice gauge theory,

$$H_{Z_2} = J \sum_i A_i^z - h_x \sum_i \sigma_x^i \tag{3.6}$$

where A_i^z is the star operator defined as $A_i^z = \sigma_z^1 \sigma_z^2 \sigma_z^3 \sigma_z^4$ acting on 4 spins emanating from a single site as shown in Fig. 3·2(b). The local gauge generator $B_p = \prod \sigma_x$ is defined as a product of σ_x operators around an elementary plaquette [shown as the blue cross in Fig. 3·2(b)], which is a conserved quantity of the system, i.e. $B_p \left|E_q\right\rangle = q \left|E_q\right\rangle$ where $\left|E_q\right\rangle$ is an energy eigenstate. Thus we can use these operators to characterize the quantum number sectors.

In a system with Hamiltonian as in Eq. (3.1), which possesses combinatorial Z_2 gauge symmetry, the exact local gauge transformation on a plaquette p includes additional transformations corresponding to the action of an operator $\mathcal{L}_s^\mu$ on the matter spins of star s as [14]

$$\mathcal{L}_s^\mu \; \mu_a^z \; \left(\mathcal{L}_s^\mu\right)^{-1} = \sum_b \mu_a^z \; (\mathbf{L}^{-1})_{ba} \;, \tag{3.7}$$

which implements the flips and permutations associated to the monomial matrix $\mathbf{L}$. The plaquette term generating the combinatorial Z_2 gauge symmetry is then defined as [14]

$$G_p = \prod_{s \in p} \mathcal{L}_s^\mu \prod_{i \in p} \sigma_i^x . \tag{3.8}$$

All the formulations that characterize the symmetry and quantum numbers in the standard Z_2 lattice gauge theory can also be applied to our model with combinatorial Z_2 gauge symmetry.

Similar to the Z_2 lattice gauge theory introduced in Chapter 2, in a system with linear size L (total spins $N = L \times L \times 6$) and periodic boundary condition, one

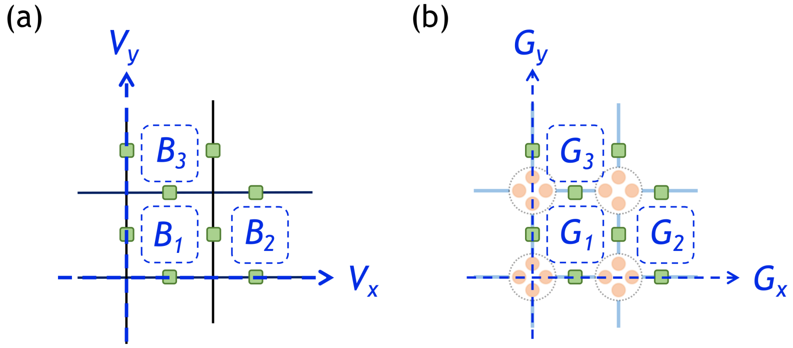

Figure 3·3: (a) Definitions of M independent gauge operators in the conventional Z_2 model for a system of size 2×2. (b) The corresponding operators define on the lattice of combinatorial Z_2 model. Here, G_x and G_y are the gauge operators defined on non-contractible loops along x and y direction respectively.

can find $M = 2 + (L^2 - 1)$ independent gauge operators G_p that commute with the Hamiltonian Eq. (3.1). Within the M operators, two of them, G_x and G_y, are defined along non-contractible loops in the two spatial directions, and their quantum numbers uniquely characterize the the 4-fold topological degeneracies of the ground state in the thermodynamic limit. As shown in Figure. 3·3(b), G_y is defined along a non-contractible loop in the y-direction, and G_x is defined in the x-direction. Other operators are local, defined as a product of σ_x around an elementary plaquette of 4 spins. Using the fact that G commutes with the Hamiltonian, we can construct eigenstates of the G operators: $G\,|q\rangle = q\,|q\rangle$ where $q = \pm 1$. It is straightforward to see that for each G operator, the eigenstate can be constructed by starting from a classical configuration (which we refer to as the "representative" state [16]) via $|q\rangle = (1 + qG)\,|\text{rep}\rangle$. Since the Hamiltonian commutes simultaneously with all M operators, the state should be constructed with a product of $1 + q_i G_i$ for all G_i. As an example, consider a 2×2 system as shown in Fig. 3·3, we have

$$|\mathbf{q}_i\rangle = \frac{1}{Z}(1 + q_x G_x)(1 + q_y G_y)\prod_{j=1}^{3}(1 + q_j G_j)\,|\text{rep}_i\rangle \tag{3.9}$$

where $\mathbf{q}$ indicates the quantum number set $\mathbf{q} = (q_x, q_y, q_1, q_2, q_3) = (\pm, \pm, \pm, \pm, \pm)$, Z is the normalization factor and subscript i indicates the i-th state within the block. There are in total 2^M symmetry blocks in the system.

3.1.2 Adding kinetic terms

The discussion thus far is rather general, and, in particular, the combinatorial gauge symmetry is exact, provided that the kinetic term H^{σ}_{kin} involves only the σ^x component. Next, we shall discuss two different choices of H^{σ}_{kin}.

Model-X: Transverse Field on The Gauge Spins

A simple choice of kinetic term is to apply a transverse field on the gauge spins,

$$H^{\sigma}_{\text{kin}} = -\Gamma_g \sum_i \sigma_i^x \ , \tag{3.10}$$

or, equivalently, the case with full Hamiltonian

$$H = J \sum_{a \in s} \left(\sum_{j \in s} W_{aj} \sigma_j^z \right) \mu_a^z - \Gamma_m \sum_{a \in s} \mu_a^x - \Gamma_g \sum_i \sigma_i^x \ . \tag{3.11}$$

In the regime where $\Gamma_g \ll J,\ \Gamma_m$, we can replace the first two terms by the star equivalent Eq. (3.5a). Therefore, Hamiltonian Eq. (3.11), which obeys the exact local combinatorial Z_2 gauge symmetry, has the usual Z_2 lattice gauge model as its low energy description:

$$H_{Z_2} = -\lambda \sum_s \prod_{i \in s} \sigma_i^z - g \sum_i \sigma_i^x, \tag{3.12}$$

with $g = \Gamma_g$ and λ given by Eq. (3.5c). The Z_2 lattice gauge model has been well studied and shown to host Z_2 topological order for $g < g_c$, and undergo a deconfinement–confinement transition at $g = g_c$ that leads to a paramagnetic phase for $g > g_c$. The critical point is $g_c \approx 0.3285\lambda$ from the exact mapping to the dual 2D Ising model

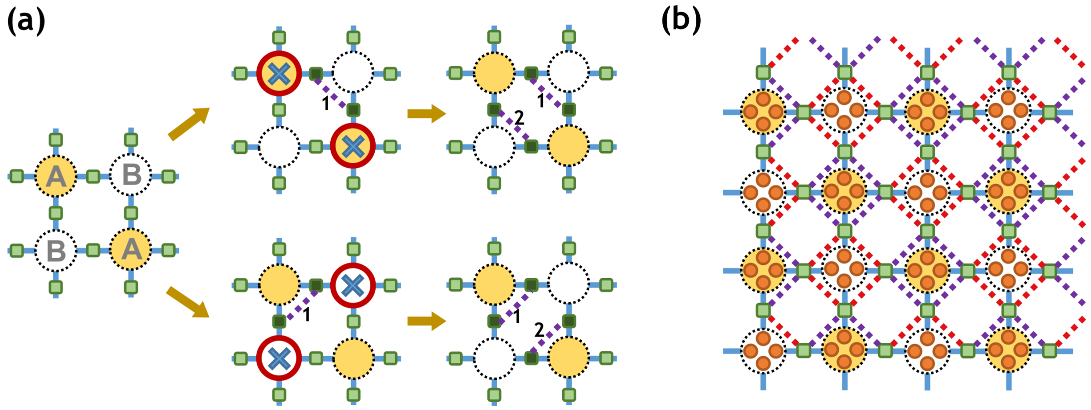

Figure 3·4: The second-order process generates the effective plaquette term in model-XX. The A-sublattice is marked in light yellow while the B-sublattice is indicated in white. **(a)** The processes that couple two stars in the A (top part) or B (bottom part) sublattice with an effective ferromagnetic interaction. **(b)** The arrangement of XX bonds (dashed lines) resulting in an effective TFIM on A and B sublattices. Different colors indicate bonds coupling sites in the A and B sublattices.

[17, 18, 19, 20].

Model-XX: Ferromagnetic XX-interaction On The Gauge Spins

Another simple choice of kinetic term is to add two-spin XX interactions between nearest-neighbor gauge spins,

$$H^{\sigma}_{\text{kin}} = -J_x \sum_{\langle kl \rangle} \sigma^x_k \sigma^x_l \ , \tag{3.13}$$

so that the full Hamiltonian is

$$H = J \sum_{a \in s} \left(\sum_{j \in s} W_{aj} \sigma^z_j \right) \mu^z_a - \Gamma_m \sum_{a \in s} \mu^x_a - J_x \sum_{\langle kl \rangle} \sigma^x_k \sigma^x_l \ . \tag{3.14}$$

Notice that H^{σ}_{kin} satisfies the general conditions presented above to retain the combinatorial gauge symmetry. (H^{σ}_{kin} is written in terms of σ^x only, and thus commute with the local operators G_p.)

To gain intuition about the model with Hamiltonian Eq. (3.14), we again consider the limit $J_x \ll J$, Γ_m and further taking $\Gamma_m \to \infty$, so that the first two terms can be replaced by their equivalent star term Eq. (3.5a). Defining the four-spin star operator $A_s^z \equiv \prod_{i\in s} \sigma_i^z$, the effective Hamiltonian, without the kinetic term, reads $H_0^{\text{eff}} = -\lambda \sum_s A_s^z$. The ground states of H^{eff} have $A_s^z = 1$ (parity $+1$) on all stars or vertices. Similarly to the dual mapping of the conventional Z_2 lattice gauge model, we can introduce a conjugate star operator A_s^x that flips the eigenvalue of A_s^z, in terms of which we write the gauge spin between two nearest-neighbor stars s and s' as $\sigma_i^x = A_s^x A_{s'}^x$.

The XX kinetic term Eq. (3.13) perturbatively generates four-spin plaquette interactions (i.e., products of four σ^x around the small loop around a plaquette). To this end, the bond operators in the kinetic term can be arranged, e.g., in the way illustrated in Fig. 3·4. Starting from the ground state of H_0^{eff}, where all vertices have parity $A_s^z = +1$, acting with a term of the form $\sigma_k^x \sigma_l^x$ on two sites k and l within a vertex s generates a pair of defects on either the A or the B sublattice, depending on the bond chosen. Adding another bond operator within the same plaquette, parallel to the first bond, generates a plaquette term at second order in J_x/λ. The effective perturbative Hamiltonian in terms of the $A^{z,x}$ operators then takes the form

$$H^{\text{eff}} = -\lambda \sum_s A_s^z - 2J_x \sum_{\langle ss' \rangle} A_s^x \, A_{s'}^x \ , \tag{3.15}$$

where $\langle ss' \rangle$ indicates nearest-neighbor stars within the same sublattice, and λ is the aforementioned effective strength of the star-term, Eq. (3.5c). In this regime, our model thus effectively reduces to two independent TFIMs; one on each sublattice. The particular arrangement of the XX terms imposes an additional even-odd conservation law in the system. The parity of negative A_s^z vertices within a sublattice is conserved, which can be easily seen from Fig. 3·4(a), where the XX operators can only create defects in pairs within each one of the sublattices.

3.2 Stochastic Series Expansion for CGS Models

The QMC simulations presented in this paper were performed with the standard SSE method, generalizing the TFIM version of this method [21] to the present more complicated model. Consider a system with partition function $Z = \mathrm{Tr}\left[\exp\{(-\beta H)\}\right]$ where H is the Hamiltonian and β is the inverse temperature. In the SSE algorithm, we express the partition function by expanding in the σ_z (μ_z) basis $|A\rangle$ with

$$\exp\left(-\beta H\right) = \sum_p \frac{\beta^p}{p!}(-H)^p, \tag{3.16}$$

where the generic Hamiltonian (up to a constant)

$$-H = \sum_{t,i} U_{t,i} + \sum_{t,i} K_{t,i} \tag{3.17}$$

can be written as the summation over local diagonal terms $U_{t,i}$ and the off-diagonal parts $K_{t,i}$. If needed, constants are added to the diagonal parts $U_{t,i}$ in order to remove the diagonal sign problem. Here, the index t indicates the type of the operator (which in the present case can be single-site or two-site operators) and i corresponds to the lattice location of the operator.

To construct an efficient sampling scheme, following the standard SSE construction, the operator product $(-H)^n$ is expanded into "strings" of the elementary $U_{t,i}$, and $K_{t,i}$ operators of the Hamiltonian. To avoid explicitly summing over the expansion orders n with variable-length strings, one can further introduce an automatically determined cutoff M (large enough for the power series to be fully convergent in practice) and distribute $M - n$ unit operators I at random among the n operators drawn from the Hamiltonian. By summing over all the locations of the unit operators, compensating for the number of equivalent terms (number of ways of distributing the identity operators) by a factor in the weight function, the partition function can be written as

$$Z = \sum_{A_0, S_M} \mathbb{W}(A_0, S_M), \tag{3.18}$$

with configurations specified by a state $|A_0\rangle$ and an operator string S_M of fixed length M. The weight of the configuration is given by

$$\mathbb{W}(A_0, S_M) = \frac{\beta^n (M-n)!}{M!} \prod_{p=1}^{M} \left\langle A_p | Q^{(p)} | A_{(p-1)} \right\rangle . \tag{3.19}$$

All the spin states in the path-integral-like construct can be accessed by acting on $|A_0\rangle$ with partial operator strings $S_p = Q(p) \cdots Q(2)Q(1)$, where p indicates the position ("slice", $p = 1, ..., M$) and with $Q(p)$ the operator acting at slice p. The index n indicates the total number of operators drawn from the Hamiltonian and S_M is the full operator string (which contains also the randomly distributed unit operators) by which $|A_0\rangle$ must be propagated back to itself for periodic time boundaries corresponding to the trace.

The Monte Carlo sampling procedures are essentially performed in the configuration space of strings S_M, but changes in the string also implies spin changes, including changes in A_0. For both model-X and model-XX, we follow similar sampling procedures as those previously established for the TFIM. We here mainly point out the extensions relative to the standard TFIM and refer to Ref. [21] for motivations and further details not covered here.

To efficiently sample the partition function, each Monte Carlo step comprises two types of updates—the diagonal (local) update and the non-local cluster update.

The diagonal update entails operators swaps of the kind

$$I^p \leftrightarrow U^p_{t,i}. \tag{3.20}$$

For each slice p, the substitution $I \to U$ is proposed as follows. First, a diagonal operator $U_{t=c}$ of type c is chosen according to the following probability:

$$P_c = \frac{U_c N_c}{\sum_t U_t N_t}, \tag{3.21}$$

where N_t is the total number of locations (number of sites or number of bonds, for example) associated with the type t. Then one of the locations $i \in N_t$ is chosen uniformly at random to replace the current unit operator I. This substitution is accepted according to the probability

$$P(I \to U_{c,i}) = \frac{\beta}{(M-n)} \sum_t U_t N_t, \tag{3.22}$$

while the reverse substitution $U_{c,i} \to I$ is accepted with probability

$$P(U_{c,i} \to I) = \frac{(M-n+1)}{\beta \sum_t U_t N_t}, \tag{3.23}$$

to satify detailed balance.

To be more specific, for model-X we have the following Hamiltonian

$$\begin{aligned} H = & \sum_{a,j \in s} J W_{aj} \sigma_j^z \mu_a^z - |J W_{aj}| \\ & - \Gamma_m \sum_{a \in s} (\mu_a^x + 1_a) - \Gamma_g \sum_i (\sigma_i^x + 1_i), \end{aligned} \tag{3.24}$$

where we have slightly re-written the Hamiltonian in Eq. (3.11) by including a constant shift in the diagonal terms to ensure that all matrix elements are positive. In this case, we have three types of diagonal terms

$$U_{t=1,a} = \Gamma_m (1_a), \tag{3.25}$$

$$U_{t=2,i} = \Gamma_g (1_i), \tag{3.26}$$

$$U_{t=3,ja} = -J W_{aj} \sigma_j^z \mu_a^z + |J W_{aj}|, \tag{3.27}$$

as well as two types of off-diagonal terms

$$K_{t=1,a} = \Gamma_m \mu_a^x, \tag{3.28}$$

$$K_{t=2,i} = \Gamma_g \sigma_i^x. \tag{3.29}$$

Following the vertex notation introduced in Ref. [21], the possible vertices are shown in Fig. 3·5

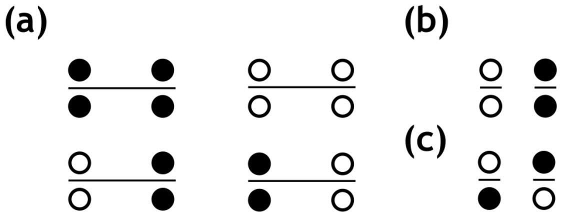

Figure 3·5: All allowed vertices for model-X. (a) FM and AFM vertices associate with the operators $U_{t=3}$. (b) Single-site constant vertices associate with $U_{t=1}$. (c) Single-site spin flip vertices associate with the off-diagonal operators $K_{t=1}$ and $K_{t=2}$.

For model-XX, we have

$$\begin{aligned} H = & \sum_{a,j\in s} JW_{aj}\sigma_j^z\mu_a^z - |JW_{aj}| - \Gamma_m \sum_{a\in s}(\mu_a^x + 1_a) \\ & - J_x \sum_{\langle k,l\rangle}(\sigma_k^+\sigma_l^+ + \sigma_k^-\sigma_l^- + 1_{k,l}) \\ & - J_x \sum_{\langle k,l\rangle}(\sigma_k^+\sigma_l^- + \sigma_k^-\sigma_l^+ + 1_{k,l}). \end{aligned} \tag{3.30}$$

Here, we have separated the $\sigma_x\sigma_x$ term into two parts, $\sigma^+\sigma^+ + h.c.$ and $\sigma^+\sigma^- + h.c.$, such that the XX terms can be integrated into the cluster update procedure. In this case, we have four types of diagonal operators

$$U_{t=1,a} = \Gamma_m(1_a), \tag{3.31}$$

$$U_{t=2,kl} = J_x(1_{kl}), \tag{3.32}$$

$$U_{t=3,kl} = J_x(1_{kl}), \tag{3.33}$$

$$U_{t=4,aj} = -JW_{aj}\sigma_j^z\mu_a^z + |JW_{aj}|, \tag{3.34}$$

and three corresponding off-diagonal operators of types $t = 1, 2, 3$:

$$K_{t=1,a} = \Gamma_m\mu_a^x, \tag{3.35}$$

$$K_{t=2,kl} = J_x(\sigma_k^+\sigma_l^+ + \sigma_k^-\sigma_l^-), \tag{3.36}$$

$$K_{t=3,kl} = J_x(\sigma_k^+\sigma_l^- + \sigma_k^-\sigma_l^+). \tag{3.37}$$

All the possible vertices are shown using the standard graphical vertex notation in Fig. 3·6.

Following the diagonal update, the cluster update procedure are performed for which the main goal is to swap diagonal and off-diagonal operators of the same type:

$$U^p_{t,i} \leftrightarrow K^p_{t,i}. \tag{3.38}$$

The clusters can involve a large number of vertices and also correspond to flips of a large number of spins in space-time. The clusters are constructed using the operator string via intermediate local vertex processes that are very similar to those described in Ref. [21], to which we refer for further details.

For model-X, the cluster update procedure is exactly the same as described in Ref. [21] for the TFIM. However, in the case of model-XX, the additional off-diagonal terms not present in the standard TFIM require a simple extension of the scheme, which we illustrate here in Fig. 3·6. Vertex processes for type-2 and type-3 operators

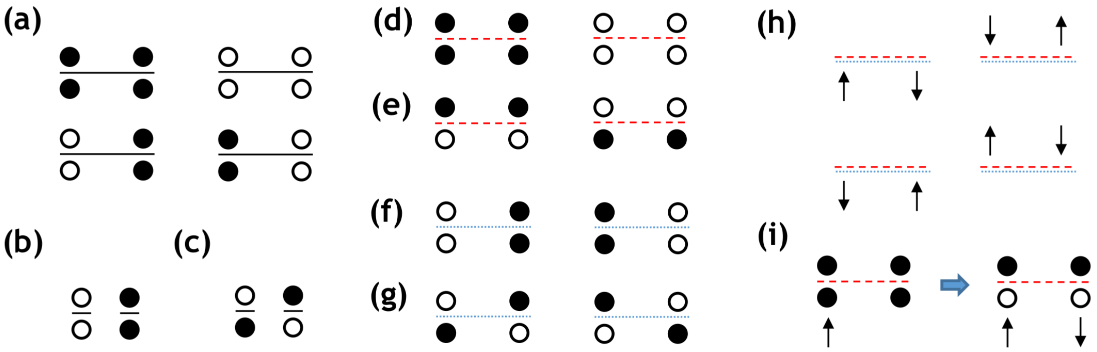

Figure 3·6: All possible vertices for model-XX. (a) FM and AFM vertices associate with $U_{t=4}$. (b) Single-site constant vertices associate with $U_{t=1}$. (c) Single-site spin flip vertices associate with $K_{t=1}$. Vertices that represent the two-site operators of type $t = 2$ are represented by the red dashed lines, with diagonal constant (d) $U_{t=2}$ and off-diagonal term (e) $K_{t=2}$. Vertices corresponding to two-site operator of type $t = 3$ are represented by the blue-dotted line, with diagonal constant (f) $U_{t=3}$ and off-diagonal (g) $K_{t=3}$. (h) Illustration of the possible vertex processes for both type-2 and type-3 operators in the cluster update for model-XX. (i) An example of an update of the kind $U_{t=2} \rightarrow K_{t=2}$.

are illustrated in Fig. 3·6(h), where the in-coming and out-going legs must be on the same side in order for new allowed vertices to be produced. An example of an $U_{t=2} \rightarrow K_{t=2}$ move is shown in Fig. 3·6(i).

3.3 Results of Model-X: Transverse Field on The Gauge Spins

In this section, we present our numerical studies of the model-X. Our results support the theoretical conjecture that the model has a topological and a paramagnetic phase with no other phases. The nature of the quantum phase transitions between these two states is revealed. In the following, we fix $J = 1$ and impose periodic boundary conditions in all our numerical simulations.

3.3.1 Fidelity Susceptibility and Phase Boundary

To confirm that the model does have phases predicted by the effective Z_2 gauge theory, we start by identifying signatures of the phase transition.

As discussed previously, In the model-X, further taking the limit $\Gamma_m \to \infty$ sends the higher energy sectors to infinity, and hence Eq. (3.12) becomes the exact low energy effective Hamiltonian in this limit. The limit $\Gamma_m \gg J$ therefore allows us to estimate the phase boundary of our model Eq (3.11) perturbatively by relating the parameters Γ_m, Γ_g, and J to the couplings g and λ of the Z_2 lattice gauge model using Eq. (3.5a)) and Eq. (3.12) as

$$\frac{g}{\lambda} \approx \frac{\Gamma_g}{12J^4/\Gamma_m^3} = \frac{\Gamma_g \Gamma_m^3}{12J^4}. \tag{3.39}$$

Setting $g = g_c \approx 0.3285\lambda$ results in the leading-order phase boundary in the (Γ_g, Γ_m) plane, as shown in Fig. 3·7(a).

The mapping to the simpler lattice gauge model is only exact in the limit of $\Gamma_m \to \infty$. In the regime where $\Gamma_m \sim J$, one can no longer exactly project out the higher energy sectors as Γ_g varies. However, since the gauge symmetry is exact in the full Hamiltonian (3.11), one still expects that the possible phases that Hamiltonian (3.11) can sustain are the Z_2 topological phase and the paramagnetic phase, both of which respect the gauge symmetry. The precise location of the phase boundary and the nature of the transition, on the other hand, may be altered by the existence of additional degrees of freedom (higher energy sectors) in Hamiltonian (3.11).

To detect possible phase transitions in the system, we consider the fidelity susceptibility, which can probe the existence of a phase transition without requiring knowledge of any order parameter [22]. The fidelity susceptibility captures the dramatic change in the wavefunction across two sides of a phase transition. It is defined

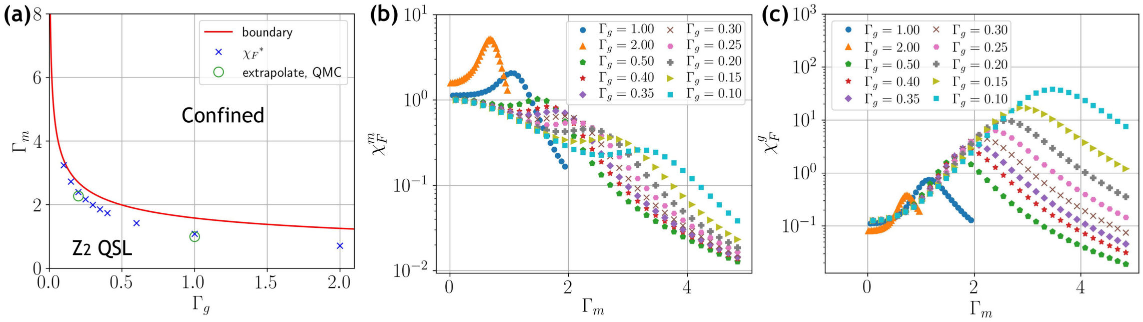

Figure 3·7: (a) Phase diagram of model-X. The red curve is the perturbative large-Γ_m phase boundary, Eq. (3.39), between Z_2 quantum spin liquid and the confined (paramagnetic) phase, resulting from the mapping to the Z_2 lattice gauge model. Blue crosses are the boundary points from the location of maximum fidelity susceptibility calculated with ED, as shown in (b). The two open circles represent the $L \to \infty$ transition point extrapolated from the QMC data simulated at fixed $\Gamma_g = 0.2$ and 1.0, where the extrapolated transition points are at $\Gamma_m \approx 2.27$, and $\Gamma_m \approx 1.0$, respectively. The Fidelity susceptibilities χ_F^m in (b) and χ_F^g in (c) were calculated using Lanczos ED with $N = 2 \times 2 \times 6$ spins.

as

$$\chi_F = \frac{\partial^2 \ln F_x}{\partial \delta_x^2}|_{\delta_x = 0}, \tag{3.40}$$

where $F_x = |\langle \psi(x) | \psi(x + \delta_x) \rangle|$ is the infinitesimal fidelity in the direction defined by x, which essentially measures the similarity between two quantum states when the tuning parameter x is varied slightly. In our model with transverse fields, two types of fidelity susceptibilities can be formally defined with variations along the two different transverse fields; $x = \Gamma_m$ or $x = \Gamma_g$;

$$\chi_F^m(\Gamma_m, \Gamma_g) = \frac{\partial^2 \ln F_{\Gamma_m}}{\partial \delta_{\Gamma_m}^2}|_{\delta_{\Gamma_m} = 0}, \tag{3.41a}$$

$$\chi_F^g(\Gamma_m, \Gamma_g) = \frac{\partial^2 \ln F_{\Gamma_g}}{\partial \delta_{\Gamma_g}^2}|_{\delta_{\Gamma_g} = 0}. \tag{3.41b}$$

At the phase transition, the fidelity susceptibility diverges in the $L \to \infty$ limit. In a finite-sized system, the divergence is replaced by a maximum at the transition, which becomes sharper and larger upon increasing the system size L. The maximum scales with L with a known exponent, which we will discuss below [23].

We first calculate the fidelity susceptibilities using exact diagonalization with the Lanczos method [23, 24] on a small system with 2×2 unit cells, i.e., $N = 24$ spins in total. Due to the rapid growth of the Hilbert space, this is currently the largest accessible system size with our computational resources. Fig. 3·7(b) shows χ_F^m as a function of Γ_m for several different values of Γ_g. A single peak is present in all cases, which implies the possibility of a phase transition in the thermodynamic limit. Furthermore, we have not observed any cases of multiple maxima in any of our calculations, suggesting only two different phases. Similar behaviors are also observed for χ_F^g as shown in Fig. 3·7(c). From the location of the maximum of χ_F^m shown in Fig. 3·7(a), we find that the data fall close to the perturbative (large-Γ_m) topological–paramagnetic phase boundary even though the value of Γ_m is not extremely large (and Γ_g not extremely small).

It may seem surprising that the phase boundary is given accurately by a system with only four unit cells. To confirm that the observed maximum of the fidelity susceptibility grows with the system size and truly indicates a phase transition, we next turn to QMC simulations to reach larger system sizes. We use the SSE QMC method [16, 25], for which a convenient way to compute the fidelity susceptibility was devised recently [26].

In our simulation, we set the inverse temperature as $\beta = 4L$. Because of the small vison gaps in the topological phase, this scaling of β does not allow us to reach the finite-size ground state deep inside the topological phase. However, with the $T \to 0$ limit approached with $\beta \propto L$ we can still address the nature of the quantum phase transition from the gapped paramagnetic phase. In our model, the

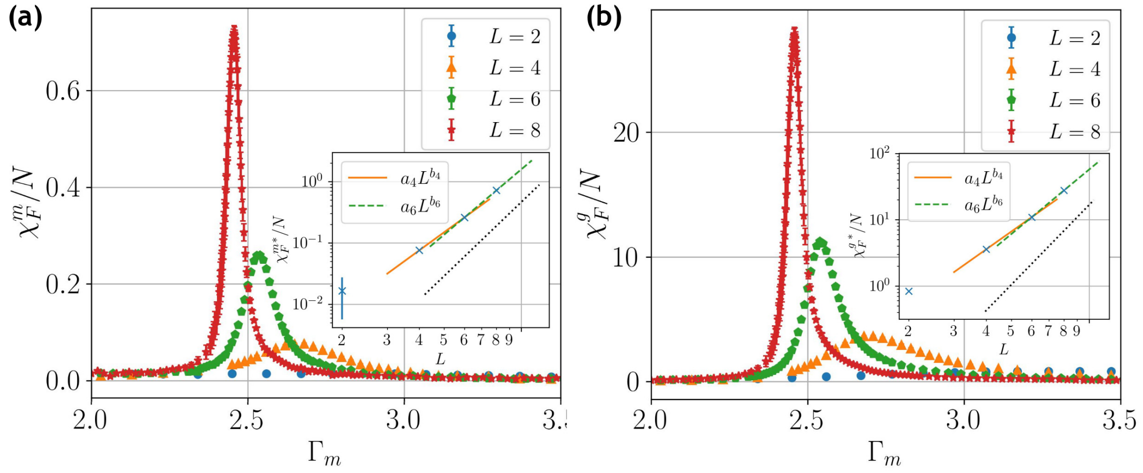

Figure 3·8: SSE results for the size-normalized fidelity susceptibilities χ_F^m/N (a) and χ_F^g/N (b) for systems with different number of spins $N = L \times L \times 6$. All data points for a given L were obtained in the same simulation with quantum parallel tempering at fixed $\Gamma_g = 0.2$ and inverse temperature $\beta = 4L$. The insets show log-log plots of the peak value of the fidelity susceptibility versus L, along with solid lines drawn through pairs of data points with L and $L + 2$ to analyze power-law behaviors $\chi_F/N \sim L^{b_L}$. The extracted size-dependent exponents in (a) are $b_4 \approx 3.0$ from the $L = 4, 6$ points and $b_6 \approx 3.5$ from $L = 6, 8$. In (b) the $L = 4, 6$ points give $b_4 \approx 2.7$ and $L = 6, 8$ give $b_6 \approx 3.2$. The dotted lines in the insets of (a) and (b) have a slope $b = 2(d+1) - d = 4$ corresponding to a first-order transition and are shown as a reference.

Ising interactions are highly frustrated, and to mitigate the associated effects of slow dynamic of the QMC updates in the topological phase and at the phase transition, we have implemented quantum replica exchange [27, 28, 29]. Simulations are thus carried out in parallel for a large number of replicas with different values of Γ_m on both sides of the transition, with swap attempts carried out for neighboring values of the parameter after several conventional SSE updates. Even with replica exchange, it is still difficult to equilibrate systems for large L, and we have limited the present study to $L \leq 8$. As we will see, these moderate system sizes are already sufficient for drawing definite conclusions.

Fig. 3·8(a) shows the results of the fidelity susceptibility χ_F^m at $\Gamma_g = 0.2$ as a function of Γ_m. We indeed find that the peak identified in the ED calculations diverges upon increasing the system size, providing solid evidence of a phase transition. The other fidelity susceptibility χ_F^g shows a similar behavior, as shown in Fig. 3·8(b).

3.3.2 Topological Order

Next, we turn to the properties of the underlying phases. Based on the mapping to the Z_2 lattice gauge model, we expect the phase with small Γ_m to be a Z_2 topological quantum spin liquid. Note that Elitzur's theorem forbids any spontaneous symmetry breaking of local gauge symmetries; thus one cannot define any local order parameter to characterize such topological order [30, 31, 7]. To detect the topological order, we investigate the global, non-contractible Wilson loop operator, defined as the product of gauge spin σ^z operators along a non-contractible loop in the α-direction

$$p_{\alpha,n} = \prod_{\{i\}_{\alpha,n}} \sigma_i^z, \quad \alpha \in \{x, y\}, \tag{3.42}$$

for the set of sites $\{i\}_{\alpha,n}$ belonging to the n-th row or column. For a Z_2 spin liquid, the quantum numbers $p_{x,n} = \pm 1$, $p_{y,n} = \pm 1$ characterize the four degenerate (in the thermodynamic limit) topological ground states regardless of which row or column n is chosen. We can take advantage of this property to define a correlation function detecting the topological order using the product of two parallel non-contractible loops on rows or columns labeled by m and n:

$$c_p^\alpha(r_{mn}) = \langle p_{\alpha,m} p_{\alpha,n} \rangle = \left(\prod_{\{i\}_{\alpha,m}} \sigma_i^z \right) \left(\prod_{\{i\}_{\alpha,n}} \sigma_i^z \right), \tag{3.43}$$

which we also illustrate in the inset of Fig. 3·9(a). Instead of investigating this correlation as a function of the distance r_{mn} between the two loops, we here take the longest distance for a given lattice size, $r_{mn} = L/2$, and analyze the L dependence of $C_p(L/2)$ defined as a summation over all translations (to reduce the statistical

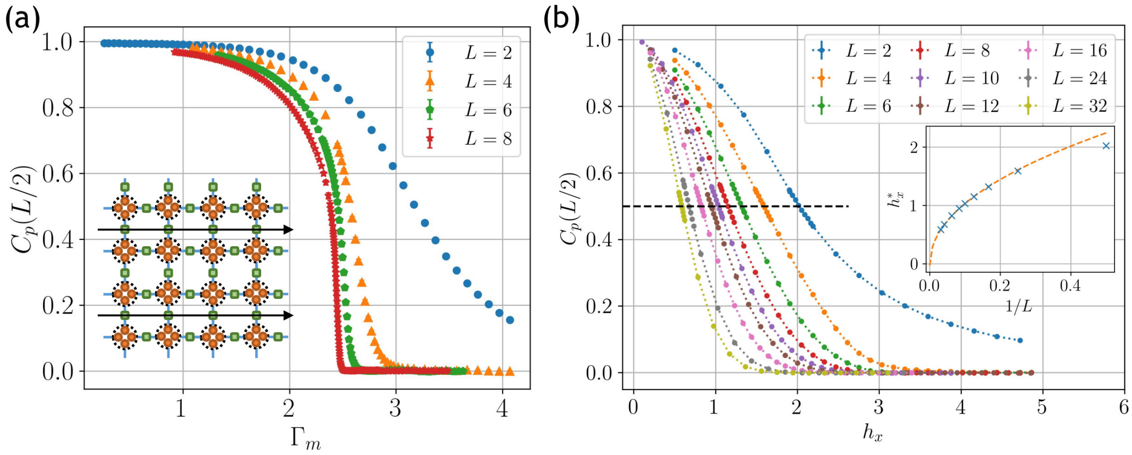

Figure 3·9: Wilson-loop correlation function obtained in SSE simulations. (a) Results for the CGS model-X with $\Gamma_g = 0.2$. Data for different system sizes show convergence to a finite value for $\Gamma_m \approx 2.3$, with the expected value $C_p(L/2) = 1$ in the $\Gamma_m \to 0$ limit. The inset illustrates the definition Eq. (3.44) of the correlation function in terms of two parallel non-contractible Wilson loops in the x direction of a periodic lattice of size $L = 4$. (b) Results for square-lattice TFIM for several system sizes at inverse temperature $\beta = 2L$. The inset shows the finite-size scaling of the location $h_x^*(L^{-1})$ for which the value of the correlator is 1/2, as indicated by the horizontal dashed line. A power-law fit $y = a + bL^{-c}$ for the $L \geq 12$ data gives $a = -0.02(1)$, $b = 3.15(2)$ and $c = 0.472(7)$, indicating a vanishing value of the correlator at any transverse field in the thermodynamic limit.

fluctuations) of the two Wilson loops oriented in the $\alpha \in \{x, y\}$ lattice direction:

$$C_p(L/2) \equiv \frac{1}{L} \sum_{j=1}^{L} c_p^{\alpha}(r_{j,j+L/2}), \tag{3.44}$$

which can be averaged over the two directions. In the topologically ordered phase we expect $C_p(L/2) \neq 0$ when $L \to \infty$, while in the paramagnetic phase $C_p(L/2) \to 0$. Note that this quantity has been used in a previous study of topological order in classical Ising gauge models at zero and non-zero temperatures [32].

In Fig. 3·9(a), we show SSE results at $\Gamma_g = 0.2$ as a function of Γ_m. We see that $C_p(L/2)$ indeed vanishes with increasing L for large Γ_m, while it converges to a finite value for Γ_m in a range consistent with the transition point found above for the same value of Γ_g. Below we will discuss the size-extrapolated phase boundary.

We stress here that the Wilson loop order parameter does not detect any phases with only local order parameters. For example, consider long range ferromagnetic phase in the transverse field Ising model (TFIM) on $L \times L$ square lattices with periodic boundary conditions at inverse temperature $\beta = 2L$. In Fig. 3·9(b), we show the same Wilson loop correlator measured from the QMC simulation. We draw the horizontal line at $C_P = 1/2$ and extract the corresponding value $h_x^*(L)$ of the transverse field. In the inset of Fig. 3·9(b), we demonstrate finite-size scaling of the value h_x^* as a function of $1/L$ with a power-law fit of the form $y = a + bL^{-c}$. Including data for the four largest system sizes, $L \geq 12$, we find the best fit with $a = -0.02(1)$, $b = 3.15(2)$ and $c = 0.472(7)$, confirming the expectation Wilson loop correlator vanishes for a conventional FM phase in the thermodynamic limit at any finite transverse field. Our results therefore demonstrate conclusively a Z_2 topological phase of finite extent as the field Γ_m is turned on.

3.3.3 First Order Phase transition

In order to understand the nature of the phase transition, We further measure other physical quantities. We also perform careful finite-size scaling to our QMC simulation results.

Peaks of Fidelity Susceptibility

Based on the similarity of the model to the Z_2 lattice gauge model, in which the transition is in the (2+1)D Ising universality class, one might naively expect a continuous transition at which the maximum should scale with system size as [23] $\chi_F/L^d \sim L^{2/\nu - d}$ with $d = 2$ the spatial dimensionality and $\nu \approx 0.63$. However, we do not observe a scaling of the above form. Instead, we analyze the data using a generic scaling form

$\chi_F/L^d \sim L^b$ with an adjustable exponent b. To further take into account finite-size corrections, we consider a size dependent exponent b_L extracted from two system sizes, L and $L+2$; graphically this exponent corresponds to the slope of the line drawn between two data points on a log-log scale as shown in the insets of Fig. 3·8.

In the case of χ_F^m in Fig. 3·8(a) we find $b_4 \approx 3.0$ (i.e., the line drawn between data points for $L=4$ and $L=6$) and $b_6 \approx 3.5$ (from $L=6,8$). In the case of χ_F^g we find $b_4 \approx 2.7$ and $b_6 \approx 3.2$. These exponents are significantly larger than the expected value $2/\nu - d \approx 2/0.63 - 2 \approx 1.175$ of the (2+1)D Ising universality class, and for both susceptibilities the deviation becomes larger for the larger system sizes. It therefore appears more likely that the transition is first-order. Generally, at classical first-order transitions the same scaling forms hold as for continuous transitions, but with the exponent $1/\nu$ replaced by the dimensionality d [33, 34]. In a quantum system, the replacement should be $1/\nu \to d+z$, where the appropriate value of the dynamical exponent z reflects the nature of the low-energy excitations in the two coexisting phases [35, 36]. Our results in Fig. 3·8 suggest a first-order behavior with $z=1$, in which case $b = 2/\nu - d \to 2(d+1) - d = 4$. We show this type of divergence for reference with the dotted lines in the insets of Figs. 3·8(a) and 3·8(b); this asymptotic behavior seems very plausible based on the available data.

Binder Ratio and Derivative

We further provide evidence of a first-order phase transition by a finite-size scaling analysis of the corresponding Binder ratio. To this end, we define the topological order parameter on the entire system as the sum of Wilson loops with $P^2 = P_x^2 + P_y^2$ where

$$P_\alpha = \frac{1}{L}\sum_{n=1}^{L} p_{\alpha,n}, \tag{3.45}$$

with $\alpha \in \{x, y\}$, and the Binder ratio

$$B = \frac{\langle P^4 \rangle}{\langle P^2 \rangle^2}. \tag{3.46}$$

In a perfect Z_2 ordered topological phase, $P_x = \pm 1$ and $P_y = \pm 1$, forming a $Z_2 \times Z_2$ symmetric order parameter distribution, while $P_x = P_y = 0$ in the paramagnetic phase. With increasing system sizes, the Binder ratio is expected to form a step function at the transition point in the case of a continuous transition, while the distribution of the order parameter in the coexistence state at a first-order transition typically is also associated with a divergent peak adjacent to the step [37, 38]. In Fig. 3·10(a) the Binder ratio indeed evolves into a step function with a side peak, though the latter is only seen clearly for the largest system sizes, $L = 8$, and for $L = 6$ there is a very weak maximum as well. Looking at the derivative of B, in Fig. 3·10(b) we observe a divergent positive main peak, and for $L = 8$ a prominent negative peak reflects the presence of the first-order side peak in Fig. 3·10(a). Thus, we have strong evidence of phase coexistence at a first-order quantum phase transition caused by an avoided level crossing. The maximum of the Binder ratio derivative diverges with the system size as the step function develops.

The derivative of the Binder ratio can be evaluated directly in SSE simulations, using the estimator derived as following. Consider the Hamiltonian $H = JH_0 + \delta H_\delta$, where δ is the tuning parameter and $[H_0, H_\delta] \neq 0$. For any arbitrary diagonal observable O, the expectation can be express in the SSE representation as [16]

$$\begin{aligned} \langle O \rangle &= \frac{1}{Z} \sum_{\{\alpha_i\}} F(\beta, n) O_{\alpha_0 \alpha_0} H^{\alpha_0 \alpha_1} \cdots H^{\alpha_{M-1} \alpha_0} \\ &= \frac{1}{Z} \sum_{\{\alpha_i\}} F(\beta, n) O_{\alpha_0 \alpha_0} J^{n_J(\{\alpha_i\})} \delta^{n_\delta(\{\alpha_i\})} R\left[H_{a_i, b_i}\right] \end{aligned} \tag{3.47}$$

where

$$F(\beta, n) \equiv \frac{\beta^n (M-n)!}{M!}, \tag{3.48}$$

and we have used the short-hand notation $H^{\alpha_i \alpha_j} = \langle \alpha_i | H | \alpha_j \rangle$ and $O_{\alpha_0 \alpha_0} = \langle \alpha_0 | O | \alpha_0 \rangle$. Further, Z is the partition function, M is the operator string length and n is the number of non-identity operators in the current string. The quantity denoted $R\left[H_{a_i, b_i}\right]$ stands for the product of local Hamiltonian operators, $\prod_i H_{\alpha_i}$, where $H_{\alpha_i} = H_0^i$ or H_δ^i.

The derivative of the observable with respect to the tuning parameter δ can be calculated from

$$\begin{aligned} \frac{\partial \langle O \rangle}{\partial \delta} &= \frac{\langle O n_\delta \rangle}{\delta} - \langle O \rangle \frac{\langle n_\delta \rangle}{\delta} \\ &= \frac{\langle O n_\delta \rangle - \langle O \rangle \langle n_\delta \rangle}{\delta}, \end{aligned} \tag{3.49}$$

where n_δ is the number of the δ operators in the string. We are interested in the Binder ratio of the Wilson loop order parameter, defined as in Eq. (3.46). Using the above expressions we obtain

$$\begin{aligned} \frac{\partial B}{\partial \delta} &= \frac{\partial_\delta \langle P^4 \rangle}{\langle P^2 \rangle^2} - \frac{2 \langle P^4 \rangle \langle P^2 \rangle \partial_\delta \langle P^2 \rangle}{\langle P^2 \rangle^4} \\ &= \frac{1}{\delta} \left[\frac{\langle P^4 n_\delta \rangle + \langle P^4 \rangle \langle n_\delta \rangle}{\langle P^2 \rangle^2} - \frac{2 \langle P^4 \rangle \langle P^2 n_\delta \rangle}{\langle P_x^2 \rangle^3} \right]. \end{aligned} \tag{3.50}$$

Here $P^2 = p_x^2 + P_y^2$ defined as Eq. (3.45) is an equal-time quantity evaluated at a given "time slice" in the SSE configuration.

With the replacement $1/\nu \to d + z$ in the scaling form $dB/d\Gamma_m \sim L^{1/\nu}$ and expecting $z = 1$ here, the peaks should diverge as L^3. Indeed, in Fig. 3·10(b) the peak values for the three largest system sizes can be fitted to a power-law L^b with $b \approx 3.0$, thus supporting a first-order transition. So far, we have discussed the divergence properties of the peaks in the Binder ratio and the fidelity susceptibility. We also need to extrapolate the peak locations in order to obtain the transition point in the thermodynamic limit. Fig. 3·10(c) shows the dependence of the peak locations on $1/L$ along with extrapolations assuming power-law corrections. All quantities show mutually consistent behaviors for the largest system sizes, but χ_F^m has much larger scaling corrections than the other quantities. Extrapolations with error analysis give the critical value of the matter field $\Gamma_m^c \approx 2.27$ for the gauge field $\Gamma_g = 0.2$ considered here. In the phase diagram in Fig. 3·7(a) we have marked this transition point with a circle, and we also show the result obtained using the same methods for $\Gamma_g = 1$. These QMC points are very close to the boundary estimated from the ED results for a very small system with $L = 2$.

Here we should note that the ED results are calculated exactly at $T = 0$, while there are still some temperature effects left in the QMC results obtained with our choice of temperature scaling, $T = (4L)^{-1}$. In the case of $L = 2$, the QMC results for $\Gamma_m^c(L)$ are actually quite far from the $T = 0$ ED results because of the temperature effects. However, since $T \to 0$ as L increases, the $L \to \infty$ extrapolated QMC results are not affected by finite temperature (beside unimportant constant factors in the peaks of the physical quantities). In this regard, it can also be noted that effects of inappropriate temperature scaling with L could potentially ruin a quantum phase transition that does not extend to $T > 0$ (as is the case with topological order in two spatial dimensions), while there is no reason to expect a transition detected when $T \propto 1/L$ to vanish if T approaches zero more rapidly.

Wilson Loop Order Parameter Distribution

We further show the full distribution of the two-component Wilson loop order parameter $\rho(P_x, P_y)$. The two components of the order parameter are defined as in Eq. (3.45). Fig. 3·11 shows color-coded plots of the distribution as the phase transition is traversed. Near the transition point, in Fig. 3·11(b), we observe a five-peak structure, indicating phase coexistence at a first-order transition. In (a) and (c) we observe distributions expected in systems with and without topological order, respectively. Note that the four peaks at the corners in Fig. 3·11(a) and Fig. 3·11(b) should mathematically be of equal size, but they differ here because of the slow migration of the simulation between these peaks, which are separated by tunneling barriers in the SSE configuration space.

The results clearly show a phase coexistence as characteristic of a first-order transition.

Energy Derivative

Finally, we show another signature of the first-order phase transition from the ground state energy density. In practice, the $T \to 0$ internal energy is obtained with QMC calculations at $T = (4L)^{-1}$. The type of first-order transition indicated by the results above, where finite-size scaling with the exponent replacement $1/\nu \to d + z$ holds, should be associated with an avoided level crossing. Thus we expect a change in the slope of the energy at the transition with increasing L. In Fig. 3·12(a) we plot the energy per site as a function of Γ_m for the same gauge-field strength as considered above, $\Gamma_g = 0.2$. At first sight, the data exhibit a smooth behavior without any visible kink. However, by taking the numerical derivative of the energy, as shown in Fig. 3·12(b), we find a clear signature of non-analytic behavior, such that the derivative becomes discontinuous at the transition in the thermodynamic limit.

Along with the other results, this demonstration of a discontinuous energy derivative provides definite proof of a first-order quantum phase transition between the topological and paramagnetic states.

3.4 Results of Model-XX: Ferromagnetic XX-interaction On The Gauge Spins

In this section, we present numerical results for the system with ferromagnetic XX-interaction as kinetic term, the model-XX defined previously in Eq. (3.14). Similar as the study of Model-X, we perform lanczos ED calculations for $L = 2$ systems, as well as QMC results for larger systems up to $L = 6$ with quantum replica exchange. We fixed $\Gamma_m = 1.0$ and simulated several replicas at different values of J_x across the two phases. The values are chosen such that the acceptance rate of swapping neighboring replicas is in the range $0.4 \sim 0.6$. Our findings and arguments are very similar to those for model-X, with the exception of issues pertaining to the ferromagnetic phase, and we therefore keep the discussion brief in this section.

3.4.1 Phase Boundary

In the limit $J_x \gg \lambda$, since all gauge spins interact ferromagnetically, an x-direction ferromagnetic phase arises; thus we expect a quantum phase transition between the topological phase and a ferromagnetic phase, replacing the topological–paramagnetic transition of the model-X. Similarly to the model with transverse field on the gauge spins, where the phase boundary between the topological and paramagnetic phases is given perturbatively by Eq. (3.39) through the mapping to the TFIM, here this mapping gives the following relation between the field strength in the TFIM and the field λ in Eq. (3.5c);

$$\frac{\lambda}{2J_x} \approx \frac{6J^4}{\Gamma_m^3 J_x}. \tag{3.51}$$

Thus, the topological–ferromagnetic phase boundary can be obtained to leading order by setting the ratio above to the critical point 3.04497(18) of the 2D quantum Ising model [19, 18].

As in the previous study of model-X, we first discuss Lanczos ED results for the fidelity susceptibility χ_F^x defined as in Eq. (3.41b) with the substitution $\Gamma_g \to J_x$. In Fig. 3·13(b), we show χ_F^x versus J_x for several values of Γ_m. In all cases, we observe a peak indicative of a phase transition. The locations of the maxima are shown along with the perturbative phase boundary in Fig. 3·13(a). In Fig. 3·13(c) we plot QMC results for larger systems. As expected we find a maximum that diverges with increasing system size, showing a true phase boundary and only two phases.

3.4.2 Topological Order

The same Wilson loop order parameters P_x and P_y defined in Eq. (3.45) are used to confirm the extent of the topological phase. To detect the topological order, we again consider the correlation function $C_p(L/2)$ between two parallel non-contractible Wilson loops, defined previously in Eq. (3.44). Fig. 3·14 shows results at $\Gamma_m = 1.0$. Here a discontinuity reflecting the first-order transition develops more clearly as compared to the results for model-X in Fig. 3·9, thus suggesting a more strongly first-order transition in this case. Note, however, that the parameter values chosen for the two models in these figures, $\Gamma_g = 0.2$ and $\Gamma_m = 1$, are not directly comparable. In both cases, the strength of the discontinuity will vary with the model parameters.

3.4.3 First Order Phase Transition

Peaks of Fidelity susceptibility

To extract information about the phase transition, we perform a finite-size scaling analysis of the fidelity susceptibility peaks obtained from QMC simulations, as shown in Fig. 3·14(c). Using the effective exponent b_L defined with system sizes L and $L+2$, we find $b_2 \approx 4.8$ and $b_4 \approx 3.9$. These exponents are again significantly larger than the $2/\nu - d \approx 2/0.63 - 2 \approx 1.175$ for the (2+1)D Ising universality class, but close to

$b = 2(d+z) - d = 4$ for a first-order transition when $z = 1$. We note one difference with respect to the previous model-X, as seen in Fig. 3·8, in that case the exponent b_L increases with L, while in the present case it decreases.

Binder Ratio and The Derivative

We provide QMC results of the Binder ratio B as defined in Eq. (3.46) with both components taken into account. The results, shown in Fig. 3·15(a) exhibit developing step functions with associated peaks indicative of a first-order transition. The derivatives in Fig. 3·15(b) exhibit the expected divergent peaks. Because of the limited system sizes, we refrain from analyzing the peaks further. We have used the peaks to extrapolate the transition point to infinite size and show the result with the green circle in the phase diagram in Fig. 3·13(a) at $\Gamma_m = 1$. As in the model-X with transverse field on the gauge spins, we find only a small difference between the QMC result and the $L = 2$ ED result in this case.

Energy Derivative

We present further evidence of a first-order phase transition from the energy density. As shown in Fig. 3·15(c), in this case we observe a clear kink behavior for the larger system sizes, $L \geq 4$, and the derivative in Fig. 3·15(d) accordingly shows a strong discontinuity developing as direct evidence of phase coexistence.

3.5 Low-Energy Excitations in the Topological Phase

Having used QMC simulations to establish the existence of an extended Z_2 topological phase and its quantum phase transition into the paramagnetic phase, we now again turn to Lanczos ED calculations in order to investigate the energy level spectrum of the system.

We use the combinatorial Z_2 symmetry to block-diagonalize the Hamiltonian into $M = 2 + L^2 - 1$ blocks in the basis of Z_2 gauge generators, as discussed in detail previously. The blocks are categorized by a set $\mathbf{q} = (\pm, \pm, \{\pm\})$ of quantum numbers, where the first two elements correspond to the two non-contractible loops with associated quantum numbers G_x and G_y and $\{\pm\}$ denotes the set of $L^2 - 1$ local quantum numbers G_i. In the thermodynamic limit, the topological ground state should be four-fold degenerate, corresponding to the lowest energy states from sectors with $G_x = \pm$, $G_y = \pm$ and $G_i = +$ for all other $i \in M - 2$ local operators.

3.5.1 Level Spectroscopy for Model-X

The transverse field does not commute with the Hamiltonian; thus, there are always finite-size gaps between the four topological states in a finite system.

Our ED calculations here are again restricted to $L = 2$ (and we present some QMC results also for $L = 4$), but even for this very small system many of the salient signatures of spinon and vison excitations can be observed, as well as signatures of the first-order quantum phase transition.

In Fig. 3·16(a), we graph low-energy gaps Δ_E relative to the ground state versus the matter field Γ_m at fixed $\Gamma_g = 0.2$. For each of the 32 topological symmetry blocks pf the $L = 2$ system, the two smallest gaps are shown, but because of degeneracies due to lattice symmetries there are only 11 distinct curves. The unique finite-size ground state has $\mathbf{q} = (+, +, +, +, +)$, i.e., $G_x = +$, $G_y = +$ and $G_i = +$ for $i = 1, 2, 3$. The four levels that become degenerate in the thermodynamic limit in the topological phase are highlighted with different symbols. As for the remaining low-energy levels, we note that in the Z_2 topological phase two types of quasi-particle excitations should be expected; spinons (s) and visons (v), which are created in pairs by acting on the ground state with σ^x and σ^z respectively on the gauge spins, as indicated in the insets of Fig. 3·16(a).

In the $\Gamma_m \to 0$ limit, the spinon excitations are gapped with $\Delta_E \approx 4J$ for $\Gamma_g = 0.2$ (the gap value is exactly $4J$ if $\Gamma_g = 0$), as seen clearly in Fig. 3·16(a), where these levels are shown with orange symbols. The vison gap opens when increasing Γ_m, as can be seen from the fact that the effective model takes the form

$$H_{pert} = \sum_s H_s - g \sum_p G_p \tag{3.52}$$

to lowest order in perturbation theory. Here G_p is the local gauge generator that appears at 12th order, where the coupling is

$$g \propto \left(\Gamma_m^8 \Gamma_g^4\right)/J^{11}. \tag{3.53}$$

We can identify the vison excited states simply by considering the quantum number blocks that couple to the ground state through the on-site σ^z operators (which do not commute with the local gauge operators). In Fig. 3·16(b), we plot ED results for the same parameters as in Fig. 3·16(a), but with a change in scale to focus on the vison states. These states are gapped for all $\Gamma_m > 0$, but the gaps are much smaller in the topological phase than in the paramagnetic phase. The lowest vison state, which contains two visons, is eight-fold degenerate on the small system considered here. The other levels in Fig. 3·16(b) correspond to states with (an even number) more than two visons.

We can extract the lowest vison gap from QMC simulation by analyzing the imaginary-time autocorrelation function of σ_z, , defined as

$$G(\tau, \beta) = 1/N_g \sum_{i \in g} \left\langle \sigma_z^i(0) \sigma_z^i(\tau) e^{-\beta \hat{H}} \right\rangle \tag{3.54}$$

where σ_z is the Pauli-z operator acting on the gauge spin, τ is the imaginary time and $\beta = 1/T$ is the inverse temperature. The estimator is averaged over all the $N_g = L \times L \times 2$ gauge spins. The operator σ_z acting on the ground state creates a pair of visons, thus, at a sufficiently low temperature, the extracted gap from the exponential fitting of Green's function gives the estimation of the vison gap.

In order to obtain the gap correctly, it is essential that the temperature is sufficiently low in the simulation. To elaborate on this point, consider a finite temperature Green's function in the basis of energy eigenstates

$$\begin{aligned} G(\tau,\beta)_i &\equiv \frac{1}{Z}\left\langle \sigma_z^i(0)\sigma_z^i(\tau)e^{-\beta\hat{H}}\right\rangle \\ &= \frac{1}{Z}\sum_{a,b}\langle a|\,\sigma_z^i e^{-\tau E_a}\,|b\rangle\,\langle b|\,\sigma_z^i e^{-(\beta-\tau)E_b}\,|a\rangle \\ &= \frac{1}{Z}\sum_{a,b}|\,\langle a|\,\sigma_z^i\,|b\rangle\,|^2 e^{-\beta E_b}e^{-\tau(E_a-E_b)}. \end{aligned} \tag{3.55}$$

For the few leading terms in a system at a sufficient low temperature we have

$$\begin{aligned} G(\tau,\beta) &\approx \frac{e^{-\beta E_0}}{Z}\sum_a |\sigma_{a0}^{z,i}|^2 e^{-\tau\Delta_{a0}} \\ &+ \frac{e^{-\beta E_1}}{Z}\sum_a |\sigma_{a1}^{z,i}|^2 e^{-\tau\Delta_{a1}} \\ &= \frac{e^{-\beta E_0}}{Z}\left[|\sigma_{10}^{z,i}|^2 e^{-\tau\Delta_{10}} + \sum_{a=2}|\sigma_{a0}^{z,i}|^2 e^{-\tau\Delta_{a0}}\right] \\ &+ \frac{e^{-\beta E_1}}{Z}\sum_a |\sigma_{a1}^{z,i}|^2 e^{-\tau\Delta_{a1}}, \end{aligned} \tag{3.56}$$

where $\Delta_{ab} = E_a - E_b$ is the energy difference between the two states a and b, and we ignore all the terms with $a = b$ since the diagonal matrix element $\sigma_{aa}^{zz,i}$ vanishes. We further separate the dominant terms by rewriting the above expression as

$$\begin{aligned} G(\tau,\beta) \approx \frac{e^{-\beta E_0}}{Z}|\sigma_{10}^{zz,i}|^2 e^{-\tau\Delta_{10}}\left[1 + \sum_{a=2}\frac{|\sigma_{a0}^{zz,i}|^2}{|\sigma_{10}^{zz,i}|^2}r^{-\tau\Delta_{a1}}\right] \\ + \frac{e^{-\beta E_1}}{Z}\left[|\sigma_{01}^{zz,i}|^2 e^{\tau\Delta_{10}} + \sum_{a=2}|\sigma_{a1}^{zz,i}|^2 e^{-\tau\Delta_{a1}}\right]. \end{aligned} \tag{3.57}$$

Considering only the leading three terms related to the gap Δ_{10} we are interested in, and with the fact that $|\sigma_{10}^{zz,i}|^2 = |\sigma_{01}^{zz,i}|^2$, we have

$$\begin{aligned} G(\tau,\beta) \approx & \frac{e^{-\beta E_0}}{Z}|\sigma_{10}^{zz,i}|^2 e^{-\tau\Delta_{10}}\left[1+\sum_{a=2}\frac{|\sigma_{a0}^{zz,i}|^2}{|\sigma_{10}^{zz,i}|^2}r^{-\tau\Delta_{a1}}\right] \\ & + \frac{e^{-\beta E_1}}{Z}|\sigma_{10}^{zz,i}|^2 e^{\tau\Delta_{10}} \\ & = |\sigma_{10}^{zz,i}|^2\frac{e^{-\beta E_0}}{Z}\times \\ & \{e^{-\tau\Delta_{10}}\left[1+\sum_{a=2}\frac{|\sigma_{a0}^{zz,i}|^2}{|\sigma_{10}^{zz,i}|^2}r^{-\tau\Delta_{a1}}\right]+e^{-(\beta-\tau)\Delta_{10}}\} \end{aligned} \tag{3.58}$$

Furthermore, notice that the σ_z operator does not commute with the gauge operator G_p. In fact, if we operate on the site with spin σ_z^1 with the gauge operator $G_p = \sigma_x^1\sigma_x^2\sigma_x^3\sigma_x^4$, the σ_z operator changes the quantum number corresponding to G_p since

$$\sigma_z^1 G_p = -G_p\sigma_z^1. \tag{3.59}$$

As illustrated in Fig. 3·17, acting with a σ_z operator on the ground state with quantum number set $\mathbf{q} = (+,+,+,+,+)$ creates a pair of visons and thereby changes the quantum numbers associated with G_1 and G_3, leading to a new quantum number set $\mathbf{q}' = (+,+,-,+,-)$. This means that the ground state will have non-zero matrix elements only to the states with the right quantum number set. Thus, we can safely assume the matrix elements $|\sigma_{a0}^{zz}|^2 = 0$ for low levels. If we ignore these term in the summation we have

$$G(\tau,\beta) \sim \{e^{-\tau\Delta_{10}} + e^{-(\beta-\tau)\Delta_{10}}\}. \tag{3.60}$$

In our simulations, we evaluate this non-equal time correlator at various values of τ and extract the gap Δ_{10} by fitting the results to Eq. (3.60).

In Fig. 3·16(b) we compare the lowest gap extracted from the QMC data for the $L = 2$ system at inverse temperature $\beta = 48$ with the ED result. We observe good agreement between the two calculations. Note that the eight-fold degenerate levels with two vison excitations undergo a true (not avoided) level crossing with a state with $G_x = G_y = +$ and all local quantum numbers $G_i = -$. This level-crossing is a finite-size effect, and we do not expect such behavior to persist for larger system sizes. The $G_i = -$ state contains four visons, i.e., it can be reached from the ground state with two different σ_i^z operations. It therefore does not contaminate the correlation function $G(\tau)$ corresponding to the two-vison level of interest. For this small system the four-vison state falls under the lowest 2-vison state below $\Gamma_m \approx 3$, i.e., close to the phase transition into the topological state.

Note again that the quantum numbers G_i are conserved (i.e. commute with the Hamiltonian) in both the topological phase and the paramagnetic phase of the model. However, visons with $G_i = -$ are deconfined only in the topological phase. In the paramagnetic phase, the lowest energy vison excitations must form bound states residing on two adjacent plaquettes, while states with more visons and larger separations between the visons have larger energy costs, as shown in Fig. 3·16(b).

In the inset of Fig. 3·16(b), we show the vison gap based on QMC calculations for both $L = 2$ and $L = 4$ at $\Gamma_g = 0.2$, using inverse temperature $\beta = 24L$. While the $L = 2$ gap exhibits only a rather smooth variation with Γ_m, at $L = 4$ a sharp feature has developed close to the phase transition. The sharp behavior of the gap here is consistent with the scenario of a first-order transition through an avoided ground state level crossing, and this mechanism should be associated also with avoided level crossings of the low-lying excitations.

Although the model possess Z_2 topological order and can be directly implemented on existing quantum devices [15], it will be difficult to reach the true ground state, or even a thermal state with a low density of visons, due to the very small vison gap. These difficulties are clear from the effective model obtained perturbatively, Eq. (3.52) with the 12th-order effective coupling in Eq. (3.53). Nonetheless, there may still be signatures of the mutual statistics of the spinons and visons that could be observed in the regime where temperature is larger than the vison gap but still much smaller than the spinon gap, as discussed in Ref. [39]. In this regime the visons randomly appear within plaquettes because their energy of formation is much smaller than the temperature. In the presence of kinetic terms (such as a transverse field), the spinons acquire dynamics at a scale much faster than that of the visons, so effectively they quantum diffuse in a background of randomly placed visons. Because of the mutual statistical phase of π between the two types of particles, the random visons serve as sources of π fluxes, which lead to quantum interference corrections to the diffusion of the spinons.

3.5.2 Level Spectroscopy for Model-XX

We now turn to analyzing energy levels for model-XX. We have again used Lanczos ED to find low-lying states for each block of quantum numbers characterizing the combinatorial Z_2 symmetries in the $L = 2$ system. In Fig. 3·19, we present the two smallest gaps versus the XX coupling J_x at $\Gamma_m = 1.0$. The lowest states in the sectors $G_x = \pm$, $G_y = \pm$ and $G_i = +$ again are those that will eventually become degenerate as $L \to \infty$ in the topological phase, and these states are highlighted with different symbols. The lowest energy excitations in the topological phase, states with visons, form levels very similar to what we saw in the model-X. However, the spinon spectrum looks very different. Due to the XX ferromagnetic interaction, spinons created in pairs within one of the sublattices has lower energy comparing to the one created in neighboring pairs (created by a single σ_x operation) as illustrated in Fig. 3·19(a).

At $J_x \to 0$, only spinon excitations exist, with a gap size of order $\mathrm{O}(J)$, as can be seen in Fig. 3·19(a) where these levels are marked in orange. The vison gap opens with increasing J_x, as the effective model from the lowest order in perturbation takes the form

$$H_{\mathrm{pert}} = \sum_s H_s - g \sum_p G_p. \tag{3.61}$$

Here G_p is the local gauge generator (plaquette term) that appears at 10th order, with $g \sim \Gamma_m^8 J_x^2 / J^9$, which should be compared to the 12th order perturbative Hamiltonian in the case of model-X.

In the case of the XX interaction used here, there is an additional gauge spin inversion symmetry in x-basis that is not present in the model-X. Define the inversion operator

$$V \equiv \prod_i \sigma_i^z \tag{3.62}$$

as the product of all σ^z gauge-spins. This operator clearly commute with Hamiltonian and its quantum numbers $v = \pm$ correspond to symmetric or antisymmetric states. We find that all the lowest energy levels of the 32 gauge blocks (blue) are symmetric and the second state (orange) is always anti-symmetric except for the highest energy level shown in Fig. 3·19(a), which exhibits an actual level crossing. In Fig. 3·18 we show the same energy levels of the model-XX at $\Gamma_m = 1.0$ as previously in Fig. 3·19. Here different colors indicate symmetry or antisymmetry with respect to V. In the FM phase at large J_x the gauge spins order along spin-x direction, and the first excited state and the ground state are both from the block with topological quantum number set $\mathbf{q} = (+++++)$. In Fig. 3·19 we can observe how the symmetric and antisymmetric V states become degenerate (strictly in the thermodynamic limit) to allow spontaneous symmetry breaking in the FM phase.

Among all the spinon excitations, the lowest one belongs to the same sector as the ground state, with $\mathbf{q} = +++++$. This excitation, which is marked with a dashed line in Fig. 3·19(a), becomes degenerate with the ground state for large J_x, reflecting the ferromagnetic Ising order with spontaneously broken Z_2 symmetry in the thermodynamic limit.

For the vison excitations, since σ^z operators do not commute with local gauge operators, we can identify the vison excited states simply by considering the quantum number blocks that couple to the ground state through the on-site σ^z operators. In Fig. 3·19(b), we plot ED results for the same parameters as in Fig. 3·19(a), but with a change in scale to focus on the vison states. These states are gapped for all $J_x > 0$, but the gaps are much smaller in the topological phase than in the FM phase. The lowest vison state, which is marked by yellow symbols in Fig. 3·19(b), contains two m particles, and is eight-fold degenerate on the small system considered here. The other levels marked by blue in Fig. 3·19(a) correspond to states with more than two (an even number of) visons.

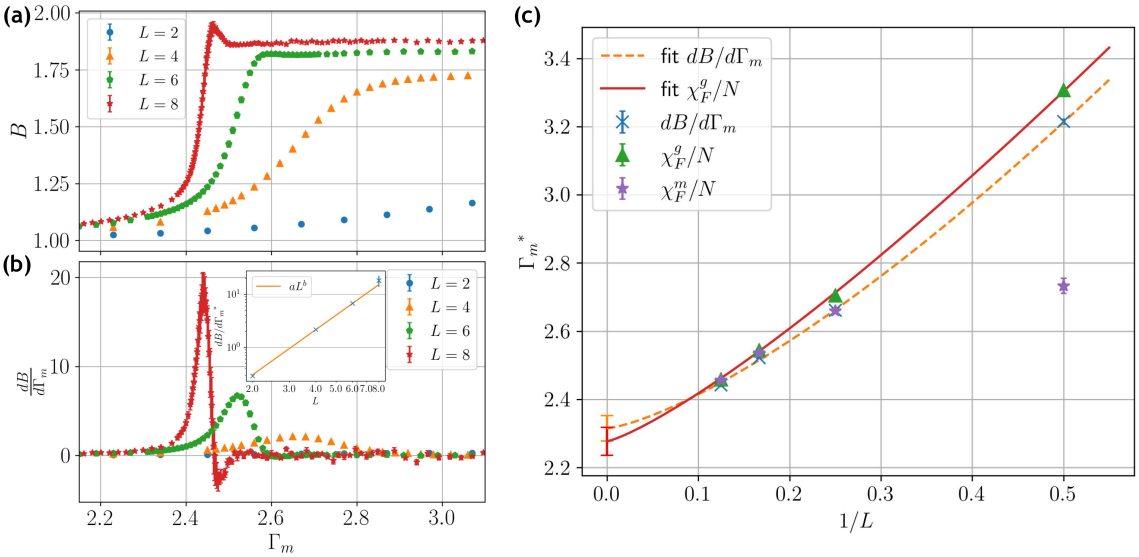

Figure 3·10: Results for the model-X at $\Gamma_g = 0.2$. (a) The Binder ratio B defined with both components of the Wilson loop order parameter $P^2 = P_x^2 + P_y^2$ in Eq. (3.46). The peaks adjacent to the phase transition for system sizes $L \geq 6$ (barely discernible for $L = 6$) are signatures of a first-order transition. (b) The numerical derivative of B with respect to Γ_m [computed using the linear approximation between the successive points in (a)]. The inset shows a power-law fit $y \propto L^b$ to the maximum value of the derivative, with only the largest three system sizes included. The exponent is $b \approx 3.0$, which is consistent with expected value $b = d + 1 = 3$ for a first-order transition. (c) Scaling with the inverse system size of the Γ_m values of the finite-size maxima $dB/d\Gamma_m$, χ_F^m/N and χ_F^g/N, with $\Gamma_g = 0.2$. Both $dB/d\Gamma_m^*$ and χ_F^{g*}/N have been fitted with a single power-law correction and give the $L \to \infty$ extrapolated values $\Gamma_m^c = 2.31(3)$ and $\Gamma_m^c = 2.27(4)$, respectively. The apparent large subleading corrections to χ_F^{m*} location forbid us to get a reasonable extrapolation based on the available data, though the $L = 6$ and $L = 8$ pints show full consistency with the other estimates.

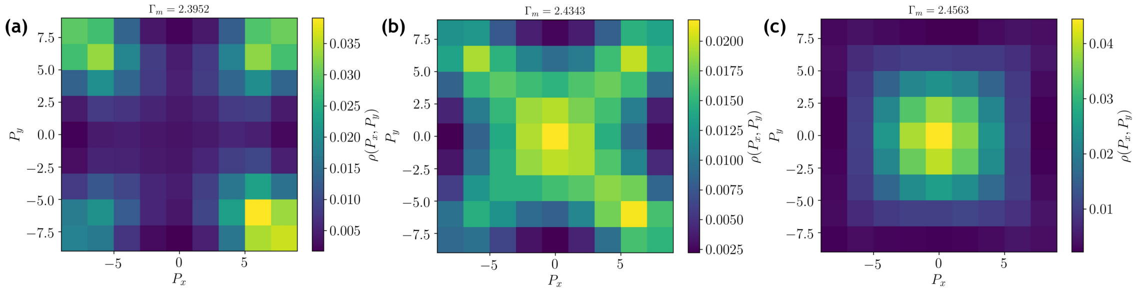

Figure 3·11: Distribution $\rho(P_x, P_y)$ of the Wilson loop order parameter accumulated in SSE simulation at $\Gamma_g = 0.2$ and three different values of the matter field; (a) $\Gamma_m = 2.3952$ (in the Z_2 QSL phase), (b) $\Gamma_m = 2.4343$ (close to the transition point), and (c) $\Gamma_m = 2.4563$ (in the confined phase). Near the transition point, in (b), five peaks are clearly observed, reflecting phase coexistence at a first-order transition.

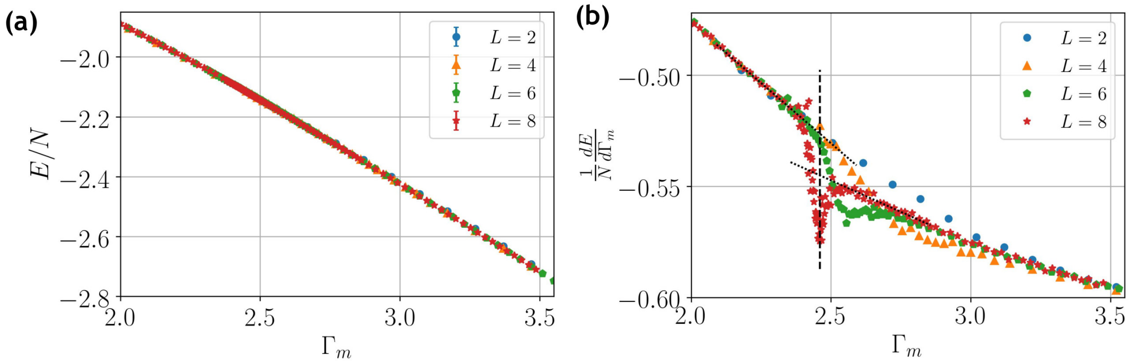

Figure 3·12: (a) Energy density computed in SSE simulations with $\Gamma_g = 0.2$. (b) The corresponding derivatives are taken numerically based on the available data in (a). Features indicating a discontinuity developing with increasing L demonstrate a first-order transition. We have fitted lines to the $L = 8$ data away from the sharp features and observe the presence of a jump when these forms are extrapolated to the location of the sharp peak (the vertical dashed line, which can be taken as a finite-size definition of the transition point).

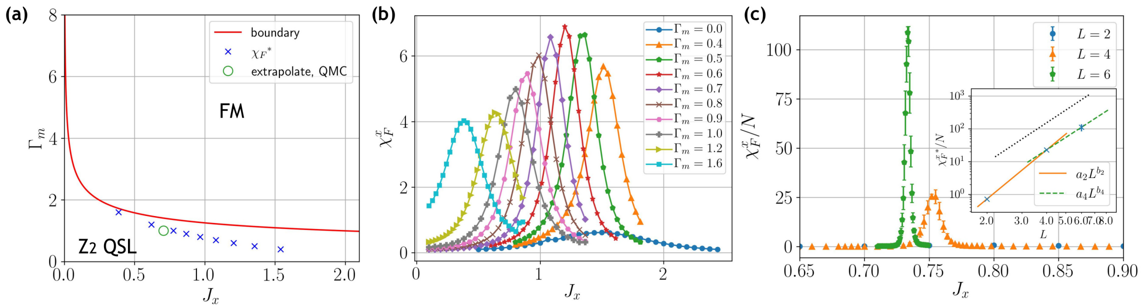

Figure 3·13: (a) Phase diagram of the model with XX interactions. The red curve is the approximate phase boundary obtained from the asymptotic $\Gamma_m \to \infty$ mapping to the TFIM. This boundary separates the Z_2 topological quantum spin liquid and the ferromagnetic phases. The blue crosses are points on the boundary estimated from the maximum of the fidelity susceptibility in (b), calculated using ED on an $L = 2$ system. The green open circle indicates the $L \to \infty$ extrapolated transition point $J_x \approx 0.706$ from QMC simulations at $\Gamma_m = 1.0$. (c) Fidelity susceptibility of model-XX at $\Gamma_m = 1.0$ for different system sizes L calculated using SSE simulation at inverse temperature $\beta = 4L$. The inset shows power-law fits $y \propto L^{b_L}$ to the maximum values for system sizes L and $L + 2$. The exponents are $b_2 \approx 4.9$ and $b_4 \approx 3.9$. The slope of dotted line corresponds to the predicted exponent $b_\infty = 2(d + 1) - d = 4$ expected for a first-order transition.

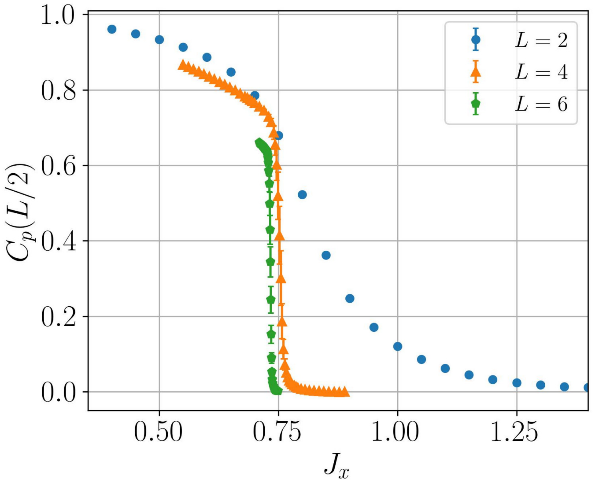

Figure 3·14: QMC results for model-XX at $\Gamma_m = 1.0$ for the Wilson loop correlation function, Eq. (3.44).

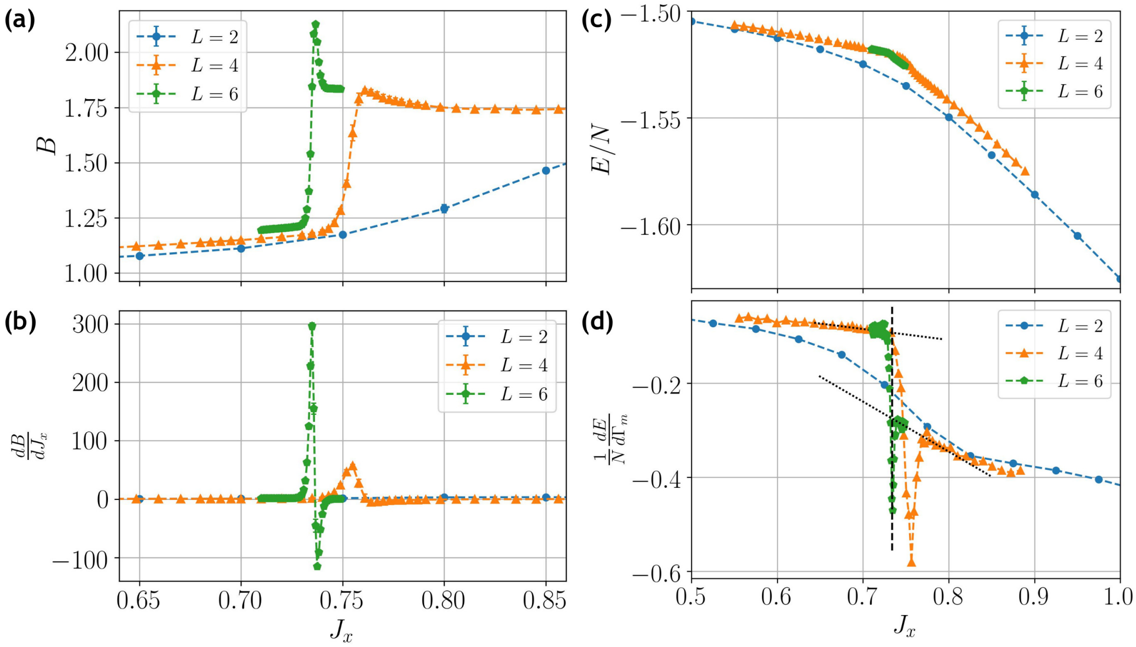

Figure 3·15: Results for model-XX at $\Gamma_m = 1.0$. (a) The Binder ratio of the Wilson loop order parameter defined with both components in Eq. (3.45); $P^2 = P_x^2 + P_y^2$. The divergent peak next to the step indicates phase coexistence at a first-order transition. Accordingly, in (b) the derivative of the Binder ratio shows divergent positive and negative peaks. (c) Energy per spin of model-XX obtained in the same simulations as the other quantities at $\Gamma_m = 1.0$ and temperature $T = (4L)^{-1}$. (d) The derivatives are evaluated using the linear approximation using the data in (c). The dotted lines are fits to the $L = 4$ results away from the peak and demonstrate a jump in the energy derivative at the transition (here represented by the peak location as indicated by the vertical dashed line).

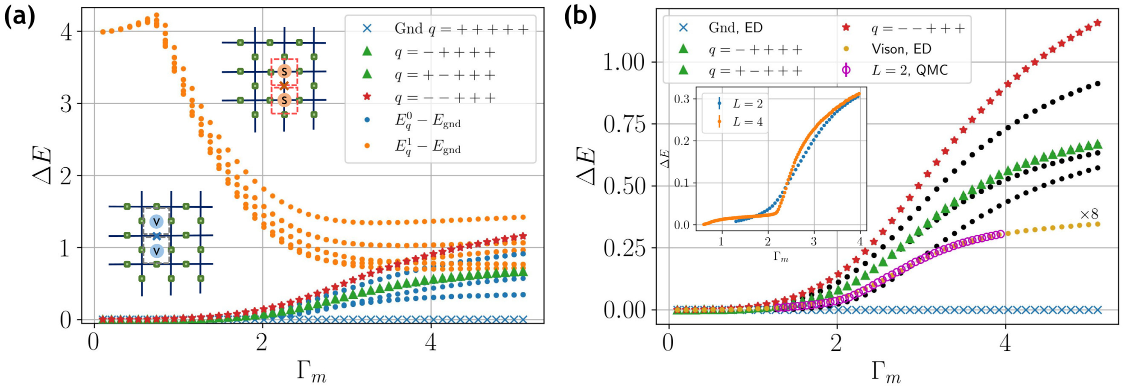

Figure 3·16: ED level spectrum at $\Gamma_g = 0.2$ for a system of size $L = 2$ ($N = 2 \times 2 \times 6$ spins). In (a) the two lowest energy gaps relative to the ground state (marked Gnd in the legends) are graphed versus the matter field strength for each of the 32 blocks with quantum numbers $\mathbf{q} = (\pm, \pm, \pm, \pm, \pm)$. Many blocks are degenerate because of lattice symmetries; thus the number of different curves is much less than 64. The four states that become degenerate topological ground states in the Z_2 phase are marked by blue crosses (the finite-size ground state), red stars, and green triangles (two degenerate sectors); these states all have the local quantum numbers $G_i = +1$. The blue dots represent all other lowest block levels; these are states with visons (two or a larger even number) of the topological phase (marked by v in the inset illustration). The orange curves represent the second-lowest states in each block; they correspond to the spinon excitations (particles indicated in the inset by s) of the topological phase and they all become degenerate for $\Gamma_m \to 0$. In (b), the lowest block states are graphed on a magnified scale. The eight-fold degenerate level that is the lowest excitation in the paramagnetic phase was calculated with both ED (yellow dots) and extracted from imaginary-time correlations from QMC simulations (violet circles), to demonstrate the correctness of the latter for $L = 2$. QMC results for both $L = 2$ and $L = 4$ (calculated at inverse temperature $\beta = 24L$) are shown in the inset.

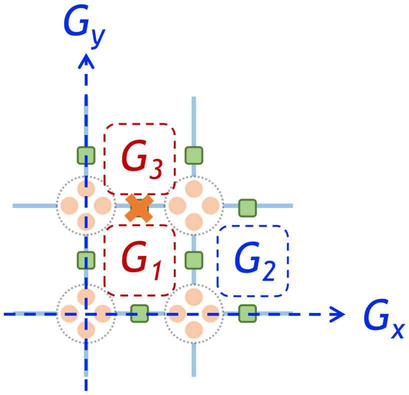

Figure 3·17: The on-site σ_z operator creates a pair of visons when acting on the ground state with quantum number $\mathbf{q} = (+,+,+,+,+)$. The quantum number corresponding to the operators G_1 and G_3 is then changed, leading to an excited state with quantum number $\mathbf{q}' = (+,+,-,+,-)$.

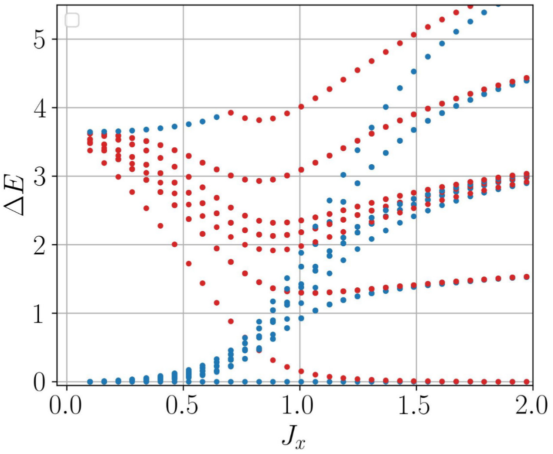

Figure 3·18: The low-energy levels previously shown in Fig. 3·19, now marked by the eigenvalues ±1 of the spin-inversion operator, Eq. (3.62), in model-XX at $\Gamma_m = 1$. The gaps to the symmetric and antisymmetric states are marked with blue and red symbols, respectively. Out of all 64 states shown here, all the vison excitation states as well as the ground state are symmetric. The spinon excitations are all antisymmetric, except for the highest one, where a level crossing causes a change in symmetry at $J_x \approx 0.7$.

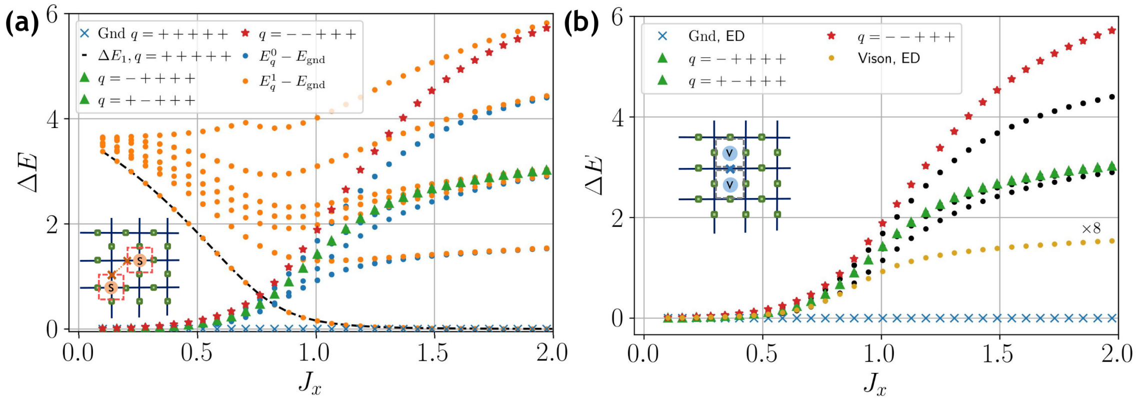

Figure 3·19: Level spectrum relative to the ground state for the $L = 2$ system with XX interactions, calculated with Lanczos ED. The organization of panels (a) and (b) is as in the corresponding Fig. 3·16 for the model-X. We refer to the same for further explanation of the visualization of the spectrum. The lowest spinon excitation, shown as orange circles with a dashed line, is the first excited state from the same block as the ground state (which has $\mathbf{q} = +++++$). This state is antisymmetric with respect to spin inversion and forms the two-fold degenerate multiplet together with the corresponding symmetric state in the ferromagnetic phase.

Chapter 4

$U(1)$ Symmetry-Enriched Toric Code

Topological order in two spatial dimensions has been extensively studied in various different realizations such as: quantum spin liquids [40, 41, 42, 43, 44, 9, 45, 11, 6, 46, 47, 48], fractional quantum Hall states [49, 50, 51, 52], superconductors [53], topological quantum field theories [54, 55], etc.

More recently, a notion of *fracton topological order* has been introduced [56, 57, 58, 59, 60, 61, 62, 63]. Fractonic phases of matter exhibit fractionalized excitations (fractons) that cannot be created in pairs. Unlike an anyon, which is created at the end points of a string-like operator (Wilson line) and can freely move across space, a single fracton is immobile, since fractons are created at the corners of membrane- or fractal-like operators. Another difference with the usual topological order is that in fractonic systems the ground state degeneracy (GSD) depends not only on the topology of the manifold, but also on the microscopic properties of the model, such as the system size and the lattice geometry. This is a manifestation of UV/IR mixing in quantum field theory [64, 65].

Additional classification of topological phases of matter arise from an interplay between symmetry and topological order. Even in the absence of intrinsic topological order, a system invariant under a symmetry can exhibit several distinct phases that cannot be adiabatically connected to each other, unless one violates the symmetry or closes the energy gap. These phases do not break the considered symmetry and are known as *symmetry-protected topological* (SPT) phases, with notable examples including free-fermionic topological insulators in 2D [66, 67, 68] and 3D [69, 70, 71, 72], topological superconductors [73], as well as interacting bosonic SPTs [74, 75, 76, 77]. Furthermore, the distinct phases protected by a symmetry need not lack intrinsic topological order. In fact, the presence of symmetry can give rise to adiabatically disconnected phases with distinct topological orders, so called *symmetry-enriched topological* (SET) phases, where anyons transform non-trivially under the symmetry [78, 79, 80, 81, 82, 83, 84, 85, 86].

Despite numerous attempts [46, 87, 79, 77, 80, 82, 88, 89, 84, 85, 90, 86], to-date there is no unifying theory for all topological orders. In the case of SETs, many classification attempts rely on constructing representative exactly solvable models that serve as fixed points for each phases. In addition, the majority of the work has been done on finite symmetry groups and only recently has there been an attempt to classify $U(1)$-symmetric SETs [86].

One of the motivations to study the model is its relation to the so called WXY model [91], which consists of two-body interaction terms between "matter" and "gauge" spins, located at the vertices and edges of a square lattice, respectively. It possesses combinatorial Z_2 gauge symmetry [14, 91, 92, 93, 94] in addition to a global $U(1)$ symmetry. The $U(1)$ toric code is believed to emerge after one integrates out the matter spins in the WXY model. However, unlike the former, the WXY model is difficult to study numerically since the unit cell is too large for exact diagonalization and the sign problem prevents us from employing Quantum Monte Carlo.

In the following, we pose the question of what happens as one tries to enrich the usual $\mathbb{Z}_2$ toric code with a global $U(1)$ symmetry. Although topological order has been previously enriched with $U(1)$ symmetry through the addition of extra degrees of freedom [95, 86], here we take a different approach and restrict the usual toric code Hamiltonian to only interactions that are $U(1)$ symmetric. The presence of the extra symmetry imposes additional constraints on the ground state loop dynamics, compared to the conventional Z_2 toric code. We refer to the lattice model as the "$U(1)$ symmetry-enriched toric code" – or "$U(1)$ toric code" for short. Its Hamiltonian is not a sum of commuting projectors, and hence not exactly solvable in any obvious way. However, the model does not have a sign problem, which allows us to study the model via large scale Quantum Monte Carlo (QMC) simulation.

4.1 Kitaev's Z_2 Toric Code with U(1) symmetry

To begin, let's elucidate our model's construction based on Kitaev's Z_2 toric code, as introduced in Chapter 1. We consider a square lattice composed of sites, each denoted as s with coordinates (i, j), where i and j represent the respective x- and y-coordinates. Additionally, we have elementary lattice vectors: $\hat{x} \equiv 2\hat{e}_x = (1, 0)$ (twice the unit vector in the x-direction) and $\hat{y} \equiv 2\hat{e}_y = (0, 1)$ (twice the unit vector in the y-direction). Now, on each link ℓ of this lattice, we place an Ising degree of freedom. A link ℓ is associated with a site s if ℓ happens to be one of the four links adjacent to that site s, specifically, if ℓ corresponds to $s \pm \hat{e}_x$ or $s \pm \hat{e}_y$.

We introduce Pauli operators with an angle parameter θ for these links. These operators, denoted as σ_ℓ^θ, are constructed as a linear combination of the usual Pauli spin operators σ^x, σ^y, and σ^z: $\sigma_\ell^\theta = \cos(\theta), \sigma_\ell^x + \sin(\theta), \sigma_\ell^y$. Similar to how the toric code defines a star operator as the product of four Pauli-X operators, here we define a star operator denoted as $A_s(\theta)$ for each site s. This star operator is the product of four Pauli operators, each corresponding to a link adjacent to site s:

$$A_s(\theta) = \prod_{\ell \in s} \sigma_\ell^\theta. \tag{4.1}$$

Importantly, the generalized star operator $A_s(\theta)$, for any angle θ, remains invariant under a Z_2 local transformation. This local transformation is generated by the product of σ^z operators on the links forming a given plaquette p:

$$B_p = \prod_{\ell \in \partial p} \sigma_\ell^z \, . \tag{4.2}$$

One can easily check that $[A_s(\theta), B_p] = 0$ holds for all combinations of s, p, and θ. This is due to the fact that a given plaquette operator either has no overlap with a star operator or overlaps with two sites of a star in the system. Further more for any local closed loop γ composed of a sequence of connected links, the loop operator

$$W(\gamma) = \prod_{\ell \in \gamma} \sigma_\ell^z \tag{4.3}$$

commutes with the Hamiltonian, $[H, W(\gamma)] = 0$, and can be represented as a product of plaquette operators B_p enclosed by γ. As also introduced in Chapter 1, when putting the system on a torus, two additional loop-operators, W_x and W_y, defined along the shortest non-contractible loops that wind around the torus in the x and y directions are also conserved.

To introduce the global $U(1)$ symmetry, we average $A_s(\theta)$ over all angles:

$$\mathcal{A}_s = \frac{1}{2\pi} \int_0^{2\pi} d\theta \; A_s(\theta) \tag{4.4}$$

When we simplify the terms within this integral, we find that this star operator can be expressed in terms of spin raising and lowering operators as follows:

$$\begin{aligned} \mathcal{A}_s &= \sigma^+_{s+\hat{e}_x} \sigma^+_{s+\hat{e}_y} \sigma^-_{s-\hat{e}_x} \sigma^-_{s-\hat{e}_y} \\ &+ \sigma^+_{s+\hat{e}_x} \sigma^-_{s+\hat{e}_y} \sigma^+_{s-\hat{e}_x} \sigma^-_{s-\hat{e}_y} \\ &+ \sigma^+_{s+\hat{e}_x} \sigma^-_{s+\hat{e}_y} \sigma^-_{s-\hat{e}_x} \sigma^+_{s-\hat{e}_y} + \text{h.c.}, \end{aligned} \tag{4.5}$$

with $\sigma_\ell^\pm = \left(\sigma_\ell^x \pm i \sigma_\ell^y\right)/2$, and h.c. stands for hermitian conjugate. Notice that the total magnetization in the z-direction, defines as $M_z = \sum_\ell \sigma_\ell^z$, is conserved. This can be easily observed from Eq. (4.5), since, in the σ^z basis, every term flips exactly two spins up and two spins down. The conservation of magnetization are originated from the global U(1) symmetry as introduced in Chapter 1. The stars $\mathcal{A}_s$ in Eq. (4.4) are invariant under a global z-axis rotation,

$$U_z \, \mathcal{A}_s \, U_z^\dagger = \frac{1}{2\pi} \int_0^{2\pi} d\theta \; A_s(\theta + \alpha) = \mathcal{A}_s, \tag{4.6}$$

where

$$U_z = \exp\left(-i\frac{\alpha}{2} M_z\right). \tag{4.7}$$

4.1.1 U(1) toric code on a ladder

We first consider the system defined on a ladder, similar to the normal toric code on a ladder but with U(1) invariant stars:

$$H_{U(1)} = -J \sum_s \mathcal{A}_s \tag{4.8}$$

where $\mathcal{A}_s = \sigma_1^+ \sigma_2^+ \sigma_3^- \sigma_4^- +$perm consists of 6 terms with all permutations of two Pauli raising and two lowering operators, as shown in Eq. (4.5).In the U(1) toric code, the neighboring stars no longer commute with each other (in contrast to the original toric code, where stars do commute, as discussed in Chapter 2). However, the plaquettes B_p^z still commute with the Hamiltonian as good quantum numbers. Notice that the U(1) invariant star term favors configurations with two spins-up and two spins-down on a star. Based on this, we expect the ground state to emerge from the sector with all $B_p^z = -1$. Indeed, our numerical results from exact diagonalization confirm the ground state with all $B_p^z = -1$.

Next, let's discuss the dual mapping. In the sector with all $B_p^z = -1$, as previously observed in Chapter 2, the original toric code on a ladder can be interpreted as the sector with fully populated and confined visons. The effective model in this case is the classical FM (Ferromagnetic) Ising model. It is worth mentioning that since a uniform field maps to a null operator in the sector with $B_p^z = -1$, the effective model remains the classical FM Ising model, irrespective of the presence of a uniform field (i.e., this sector does not 'feel' the presence of a uniform field). We find that in the manifold of this sector, the effect of the original star term A_s^x is equivalent to that of the U(1) star $\mathcal{A}_s$, since all the local basis states $|\uparrow\downarrow\rangle$ on each plaquette render the star always flippable. Therefore, in the sector of $B_p^z = -1$, the model is dual to the classical FM Ising model, as in the original toric code

$$H_{eff}^{\{B_p^z\}=-1} = -J \sum_p \tau_p^x \tau_{p+1}^x. \tag{4.9}$$

For the sector with all $B_p^z = +1$, this sector can be interpreted as having no visons in the original toric code. Recall that with $B_p^z = +1$, the local space is spanned by the basis states $|\uparrow\uparrow\rangle$ and $|\downarrow\downarrow\rangle$. Considering the same mapping as in Eq. (2.11), the U(1) star will only have non-zero values on states where the nearest neighbors are opposite. This results in the effective model:

$$H_{eff}^{\{B_p^z\}=+1} = -J \sum_p \left(\tau_p^+ \tau_{p+1}^- + \tau_p^- \tau_{p+1}^+\right), \tag{4.10}$$

which corresponds to the 1D quantum XY model.

From the above observations, we see that the U(1) star can be dual to either a classical FM interaction or a quantum XY interaction, depending on the signs of B_p^z and B_{p+1}^z that it acts upon. We summarize as follows: If $B_p^z = B_{p+1}^z = +1$, the star term is dual to a quantum XY interaction. For $B_p^z = B_{p+1}^z = -1$, it is dual to a classical Ising interaction. In cases where $B_p^z = -B_{p+1}^z$, the star term maps to a null operator and therefore disconnects (cuts) the chain, as illustrated in Fig. 4·1.

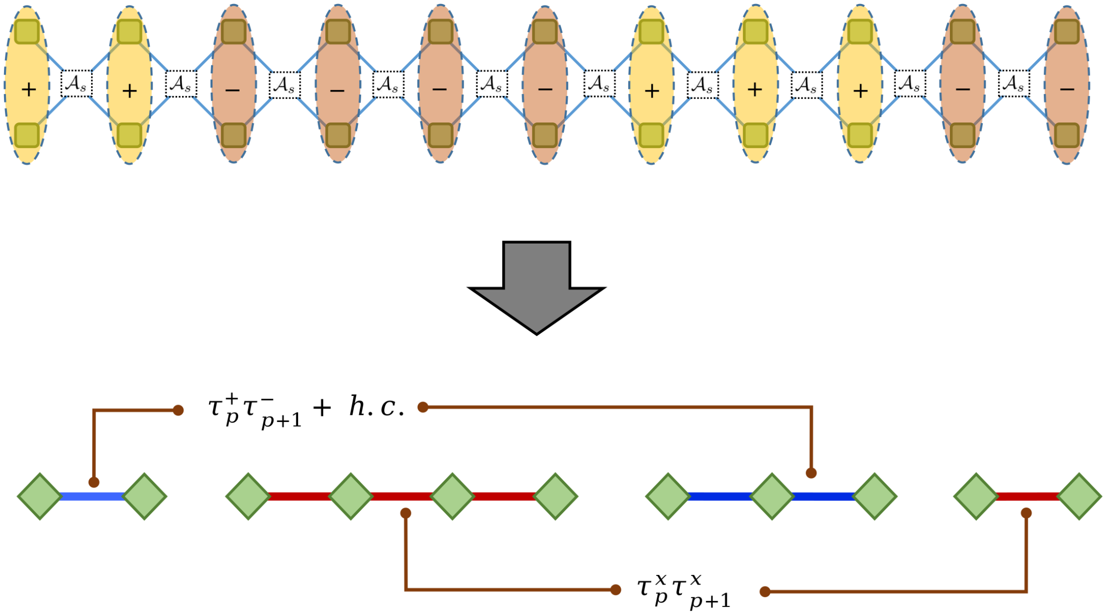

Figure 4·1: The dual mapping of the U(1) toric code ladder results in disconnected chains with XY and Ising interactions, depending on the sign of the plaquette B_p^z. In the upper graph, $B_p^z = -1$ is indicated by light orange ovals, and $B_p^z = +1$ is indicated by light yellow ovals. The mapping transforms the U(1) star operator into segments of an FM Ising chain where $B_p^z = -1$ consecutively, while consecutive $B_p^z = +1$ maps to segments of an XY chain.

4.1.2 U(1) toric code on 2D lattice

After studying the U(1) toric code on a ladder, we are now ready to define the U(1) symmetry-enriched toric code on a 2D lattice. The Hamiltonian is defined as the sum over all possible star and plaquette operators,

$$H = -\lambda_{\mathcal{A}} \sum_s \mathcal{A}_s - \lambda_B \sum_p B_p. \tag{4.11}$$

Note that, in contrast to the conventional toric code, our model is not a sum of commuting projectors: neighboring stars do not commute with each other, i.e., $[\mathcal{A}_s, \mathcal{A}_{s'}] \neq 0$ if s is adjacent to s'.

In our study we consider the system on a torus (with periodic boundary condition). Based on the above discussion, we find that the system has two kinds of conserved quantities: the total magnetization M_z from the global U(1) symmetry, as well as all the plaquettes $\{B_p\}$ and non-contractable loops W_x, W_y from the local Z_2 gauge symmetry. Therefore, the $U(1)$ toric code can be block-diagonalized in the common eigenbasis of these operators, so that each sector is characterized by a set of independent conserved quantities $\{M_z, W_x, W_y, \{B_p\}\}$.

We are particularly interested in the four sectors categorized by $W_x = \pm 1, W_y = \pm 1$, as they underscore the topological features. In the following, we refer to these four sectors as topological sectors, with respective quantum numbers $(W_x, W_y) = (+,+), (+,-), (-,+)$ and $(-,-)$.

4.2 Quantum Monte Carlo with Generalized Sweeping Cluster Update

One of the important observations from Eq. (4.11) is that our Hamiltonian is sign problem-free. This means that we can study the system with unbiased Monte Carlo methods to reach larger system sizes and also allows us to systematically study the finite-size effects.

To investigate the system, we employ the standard SSE QMC method [96, 97, 16]. In SSE simulations, the partition function is expanded as a series of powers of the Hamiltonian H, with terms from this series sampled as classical configurations. In these configurations, slices of "imaginary time" contain "vertices" that transition from one local classical configuration to another based on the terms in the Hamiltonian.

In the case of $U(1)$ toric code, there are only 6 allowed off-diagonal vertices with equal weight, as shown in Fig. 4·2(a). In order to perform the simulation, all diagonal terms have to be non-zero. To achieve this, we add a constant to the Hamiltonian, which then allows additional 16 diagonal vertices as shown in Fig. 4·2(b). The constant is chosen such that all the vertices have equal weight. Vertices with 2-up-2-down configurations are called “flippable stars”, as marked by green frames in Fig. 4·2. In the following, we set the weight of all vertices to 1.

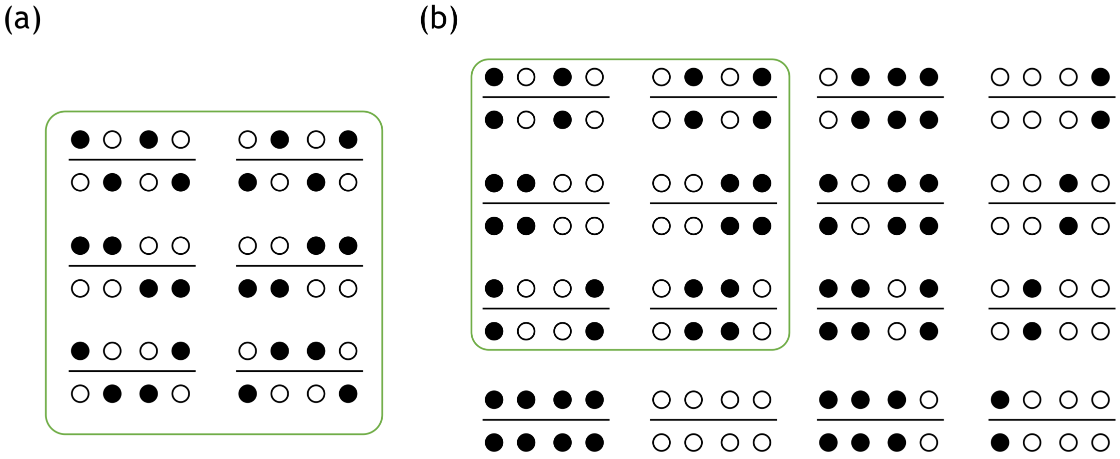

Figure 4·2: (a) 6 allowed off-diagonal vertices from the Hamiltonian. Black (white) dots denote spin-up (spin-down). The four dots below (above) the line denote the classical configuration of the four spins on a star before (after) the application of a Hamiltonian term. (b) 16 additional allowed diagonal vertices after adding a constant to the Hamiltonian. The 12 vertices marked by green frames are the flippable stars.

We follow the standard SSE procedure, which consists of two parts in each Monte Carlo step. Firstly, we perform the standard local (diagonal) update. If an ”imaginary time” slice is empty, a diagonal operator on a random star may be inserted. If an ”imaginary time” already contains a diagonal operator, it might be removed. The probabilities for these two processes are given by:

$$\begin{aligned} P_{\text{insert}} &= \frac{\beta N_s}{(M-n)}, \\ P_{\text{remove}} &= \frac{(M-n+1)}{\beta N_s}. \end{aligned} \tag{4.12}$$

Here, $\beta = 1/T$ represents the inverse temperature, $N_s = L_x \times L_y$ denotes the total number of stars, M is the total length of the operator-string (i.e., the number of "imaginary time" slices), and n is the total number of non-identity operators present in the current operator-string. Off-diagonal operators remain unaffected during this step.

he process is then followed by an off-diagonal (sometimes also called non-local) update. Naively, one might consider the cluster update method, similar to the transverse field Ising model [21], where the cluster is built starting from the off-diagonal term, and whenever a diagonal term is encountered, all the sites in the vertex are flipped. However, this update method is highly insufficient. As the system size increases and the temperature decreases, most of the time, the cluster constructed will be just the whole system, and the update is trapped in flipping back and forth between two configurations. We note that a similar issue arises in the simulation of dimer quantum models. To overcome this issue, a sweeping cluster update is proposed as a more efficient alternative for non-local updates [98].

To apply the sweeping cluster update for our U(1) toric code model, a modification is necessary. The construction of a cluster starts with the random choice of a flippable star, either diagonal or off-diagonal. This action creates four defect lines, which propagate upward along the "imaginary time" direction, initiating the growth of the cluster. We then sweep over the "imaginary time" slices, keeping track of the defect lines. If a vertex is encountered by one or more defect lines, we update the vertex according to specific rules and continue the propagation of the defect lines. The number of defect lines exiting a vertex might differ from the number entering it. Eventually, the cluster will converge, and the defect lines will terminate at another flippable star. The pictorial representation of a cluster is shown in Fig. 4·3(a). It's worth noting that cases in which a vertex has a different number of entering and exiting lines have been explored in Ref. [99] using a different approach. Our model

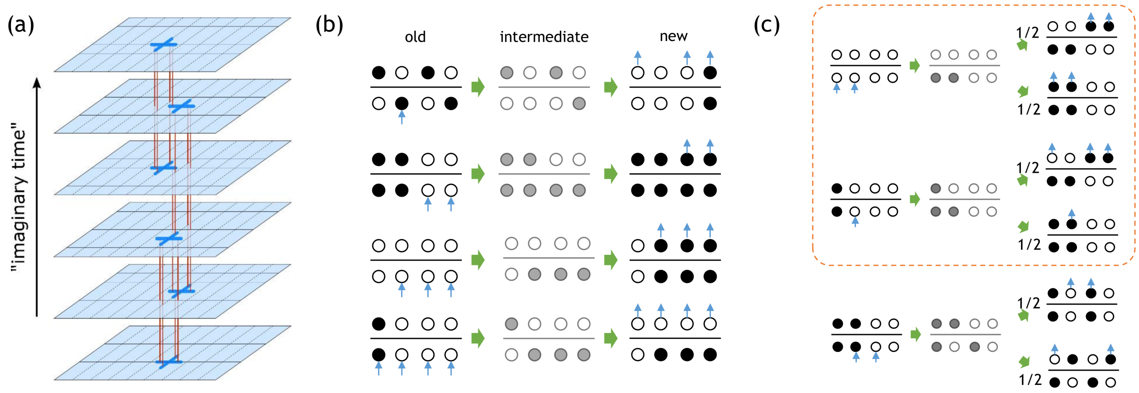

Figure 4·3: (a) Example of a cluster. It starts as 4 defect lines coming out of a flippable star. The defect lines propagate upward along the "imaginary time" direction, modifying the vertices they encounter according to specified rules. After a vertex, the number of defect lines might potentially increase/decrease. Finally, the cluster terminates at another flippable star. (b) Examples of vertex updates. If a new configuration of the bottom four spins is not flippable, there is a unique way to propagate the defect lines, such that the new vertex remains allowed. (c) Examples of vertex updates. If less than 4 defect lines hit a vertex and update the bottom four spins to a flippable configuration, there are two possible ways to propagate the defect lines. We choose one of them with probability 1/2. Processes marked by the orange frame are the updates from a non-flippable vertex to a flippable vertex, for which the reverse process does not have probability 1/2. Blue arrows denote the defect lines propagating along the "imaginary time" direction (from bottom to top).

(as well as the dimer model) has a special property that allows the cluster to build clusters in one direction.

To determine the rules for vertex updates, we proceed as follows: Consider a vertex that is intersected by a certain number of defect lines from below. We flip the corresponding spins and obtain an intermediate vertex configuration, as shown in Fig. 4·3(b) and Fig. 4·3(c). At this point, four possibilities arise:

1. If the configuration of the bottom four spins of an intermediate vertex is non-flippable, then there is only one way to propagate the defect lines through the

vertex. Some examples are shown in Fig. 4·3(b).

2. If the defect lines flip the bottom four spins into a flippable configuration, and there are less than 4 lines hitting the vertex, then there are two possible ways to propagate the defect lines. The resulting vertex can be either diagonal or off-diagonal, with probability 1/2 each. Examples are shown in Fig. 4·3(c).
3. If 4 defect lines hit a flippable vertex and the total number of defect lines is more than 4, then we propagate all the lines and flip the entire vertex.
4. If 4 defect lines hit a flippable vertex and the total number of defect lines is exactly 4, then we terminate the cluster.

Note that the transition from a non-flippable vertex to a flippable one occurs with a probability of 1/2, while the reverse process does not share this probability. To maintain detailed balance, we need to keep track of the occurrences of these processes. Consider an operator-string A transitioning into an operator-string B through the flipping of a cluster as outlined in the aforementioned procedure. Throughout this update, we enumerate the count of non-flippable vertices transitioning to flippable ones as $N_{n\to f}$ and the count of flippable vertices transitioning to non-flippable ones as $N_{f\to n}$. To satisfy detailed balance, the acceptance probability for the process $A \to B$ (via cluster flipping) should be evaluated as follows:

$$P(A \to B) = \frac{N_v(A)}{N_v(B)} \left(\frac{1}{2}\right)^{N_{f\to n} - N_{n\to f}}, \tag{4.13}$$

where N_v is the number of flippable vertices present in the corresponding operator-string.

It is important to keep in mind that the update procedure we have described conserves all quantum numbers, specifically M_z, W_x, W_y, B_p. This is useful for extracting the energy gap between different topological sectors, as we will see in the following

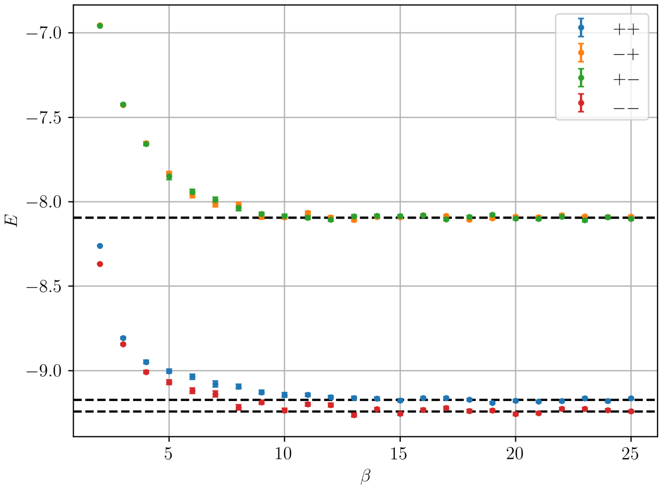

Figure 4·4: Ground state energy in four topological sectors of a system of size 4 × 4 stars. (dots) obtained from the SSE QMC with the generalized sweeping cluster update algorithm; (dashed lines) obtained from the ED calculation.

section. Furthermore, this update procedure cannot transition the system out of a specific Hilbert space fragment (Krylov subsector). Consequently, by selecting an appropriate initial state, we can effectively target a Hilbert space fragment that is dynamically connected to that initial state if necessary. Finally, we benchmark our QMC results by comparing them to the results obtained from an ED calculation of a small system size. The results are presented in Fig. 4·4.

4.3 Hilbert Space Fragmentation

In systems with symmetries, as previously mentioned, the Hamiltonian is block-diagonalized into sectors associated with the conserved quantities or charges of the symmetries. For example, consider a symmetry operator $\hat{O}$ that commutes with the Hamiltonian; it block-diagonalizes the Hamiltonian into symmetry sectors associated with quantum numbers, i.e., eigenvalues of $\hat{O}$.

In some models, even after accounting for all symmetries of the model, a given symmetry block is further divided into smaller disconnected parts that are not related to the symmetry of the system but arise from the constraints imposed by the quantum terms in the Hamiltonian. This phenomenon is called Hilbert space fragmentation, and the corresponding dynamically disconnected quantum blocks are referred to as Hilbert space fragments or Krylov subsectors [100, 101, 102]. This means that if we start with a state in one fragment, the Hamiltonian dynamics cannot transition the state into another fragment, even if they are in the same symmetry sector.

Hilbert space fragmentation typically arises in models with local kinetic constraints. In the context of our U(1) toric code model, the constraint on the quantum dynamics, where the star can only flip the local configuration with two-up and two-down spins, leads to fragmentation in the model. As a simple example, consider the two states in Fig. 4·5(a), which belong to the same block with quantum numbers: $M_z = 0$, $W_x = W_y = +1$, $B_p = +1$ for every plaquette p (with PBC).

One can easily observe that for the state at the top, all the stars have an odd number of up-spins. Therefore, the U(1) star operator in our model cannot transition the state to another state, making it inert. The state is dynamically disconnected and belong to different fragments from the state below. In fact, the inert state comprises its own 1-dimensional fragment. Another example of a 7-dimensional fragment is shown in Fig. 4·5(b). If we translate this pattern of spins in space, we will obtain a different Krylov subsector with the same quantum numbers.

Technically, fragments exhibit block structure, meaning that there must be some conserved quantity associated with each fragment. In conventional symmetries, these conserved quantities are the generators of the symmetry. However, in the thermodynamic limit, the number of fragments resulting from Hilbert space fragmentation scales much faster than the number of symmetry sectors from any type of symmetry (unless it is a local gauge symmetry) [102]. Therefore, the corresponding conserved

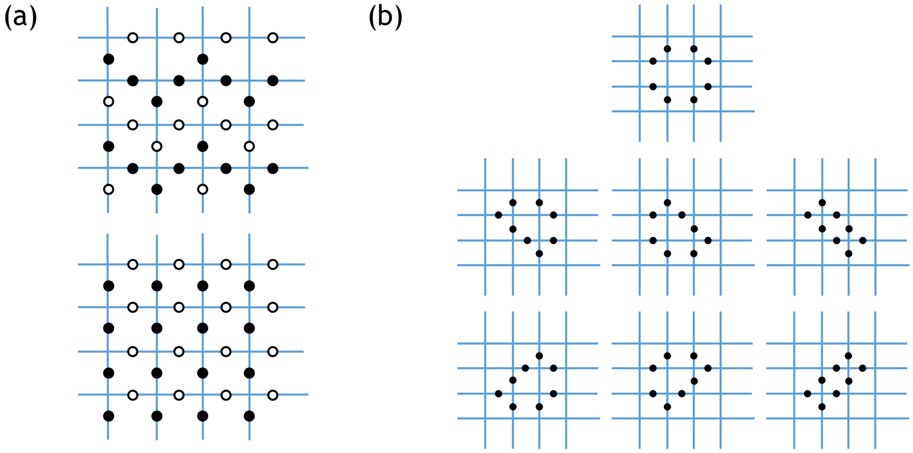

Figure 4·5: (a) Two states from the same symmetry sector, but from different fragments: an inert state with no flippable stars (top), and a state where every star is flippable (bottom) (b) Basis states of a 7-dimensional Krylov subsector. Black dots denote spin-downs, white dots (or the absence of a dot) denote spin-ups.

operators (which can be constructed, e.g., by writing down a projector on the observed block in the Hamiltonian) are highly non-local and non-trivial.

Another important factor to consider when discussing Hilbert space fragmentation is the size of fragments in a given symmetry sector. Consider a specific symmetry sector with dimension D. Let's define D_{max} as the dimensionality of the largest fragment. We are particularly interested in the ratio of D_{max}/D. If this ratio approaches one in the thermodynamic limit, then the symmetry sector is dominated by one largest block. In this case, it is called weak fragmentation. Essentially, a larger block implies more kinetic energy. In the case of weak fragmentation, the physics will be dominated by the largest fragment, and most likely, the lowest energy state in a given symmetry sector will be found in the dominant fragment.

To investigate Hilbert space fragmentation, we first categorize states into different U(1) symmetry as well as local gauge symmetry sectors. Then, for each sector of interest, we explicitly enumerate states and further categorize the states into frag-

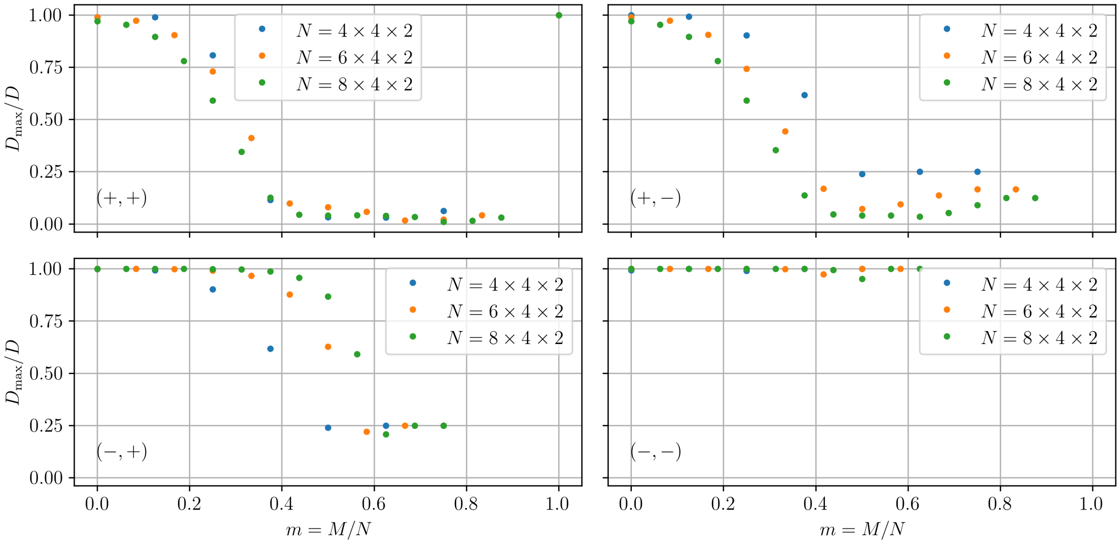

Figure 4·6: Exact enumeration study of the fragmentation fraction is defined as $D_{\max}/D$, where $D_{\max}$ is the size of the largest fragment, and D is the size of the sector. The corresponding topological sectors are marked at the lower-left side of each figure.

ments based on the flipping of stars from the Hamiltonian. We study Hilbert space fragmentation in systems of sizes $N = 4\times4\times2, 6\times4\times2$, and $8\times4\times2$ (the first two numbers represent the numbers of stars in the x- and y-directions, and the last factor of 2 corresponds to the two spins in a unit cell). We focus on the symmetry sector with all $B_p = +1$ and calculate the ratio of $D_{\max}/D$ for different magnetization and topological symmetry sectors. The results are presented in Fig. 4·6.

One can observe that the system exhibits weak fragmentation in the vicinity of zero magnetization, where the largest fragment completely dominates the Hilbert space of its symmetry sector. We conjecture that this behavior carries over to the thermodynamic limit. Additionally, through a simple combinatorial argument, it becomes apparent that the largest symmetry sectors have $M_z = 0$. Since larger random matrices exhibit a broader spread of eigenvalues compared to smaller random matrices, we can safely assume that the ground state of each of the four topological symmetry sectors belongs to its largest fragment in the $M_z = 0$ sector. This conjecture is supported by work done in a related study [103], although their results specifically apply to our $(+, +)$ topological sector.

It's worth noting that Hilbert space fragmentation in the topological $(+, +)$ sector with all $B_p = +$ of the $U(1)$ toric code can be mapped to an equivalent model that has been explored in other contexts [104, 103], where the dynamics of domain walls in the same setting have been investigated [105, 106]. Our results also confirm observations made by [103], where the same "dynamical freezing transition," characterized by a sharp drop in the $D_{\max}/D$ value at intermediate magnetization values [except for the $(-, -)$ sector, although this may be a finite size effect], has been noted.

4.4 Topological Degeneracy and UV/IR Mixing

In the scope of this study, we focus on the even parity sector where all $B_p = +1$, which corresponds to the ground states of the Hamiltonian (4.11) with sufficiently large λ_B (we set $\lambda_{\mathcal{A}} = 1$ henceforth). Within the even parity sector, we then study all four topological sectors that are characterized by $W_x = \pm 1$ and $W_y = \pm 1$.

We introduce two orthogonal compactification vectors $\vec{L}_1$ and $\vec{L}_2$, parameterized by two non-negative integers a and b, as

$$\begin{aligned} \vec{L}_1 &= L(a\hat{x} + b\hat{y}) \\ \vec{L}_2 &= L(-b\hat{x} + a\hat{y}), \end{aligned} \tag{4.14}$$

where L (a positive integer) is the linear system size. We choose the vector (a, b) to be the shortest integer vector in its direction, i.e., a and b are coprimes. Vectors $\vec{L}_1, \vec{L}_2$ define the compactification scheme in the sense that any spatial vector $\vec{r}$ is identified with vectors $\vec{r} + \vec{L}_1$ and $\vec{r} + \vec{L}_2$. An example of a small lattice with a non-trivial compactification scheme is shown in Fig. 4·7.

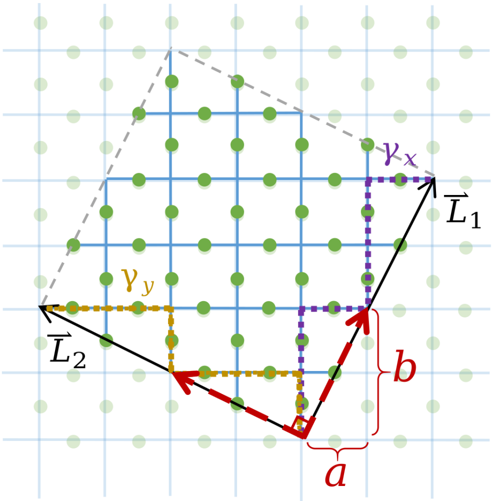

Figure 4·7: An example of a lattice with compactification $a = 1, b = 2$ and linear size $L = 2$. Any vector $\vec{r}$ is identified with vectors $\vec{r} + \vec{L}_1$ and $\vec{r} + \vec{L}_2$. The whole lattice is shown in bright colors, while the shaded region denotes repeating parts of the lattice due to the periodic boundary condition. Two non-contractible loops γ_x and γ_y shown as purple and yellow dotted lines respectively along two compactification vectors $\vec{L}_1$ and $\vec{L}_2$.

Below we explore in detail two lattice compactifications on a torus. The first one is 0°-tilt compactification, corresponding to $a = 1$, $b = 0$ – the usual compactification along the vertical and horizontal lines of the square lattice. The other is 45°-tilt compactification, with $a = 1$, $b = 1$. We focus on the systematically cases with L even, systematically study using quantum Monte Carlo method with sweeping cluster update as mentioned above. Specifically, the algorithm is designed such that the lowest energy of symmetry sector of interest can be directly accessed, specified by an initial basis state from the symmetry sector. We observe that the ground states have magnetization $M_z = 0$ in all of the topological sectors. Cases with L odd are also explored with large enough selected system size, and compactifications with other tilt angles are also studied using exact diagonalization (ED).

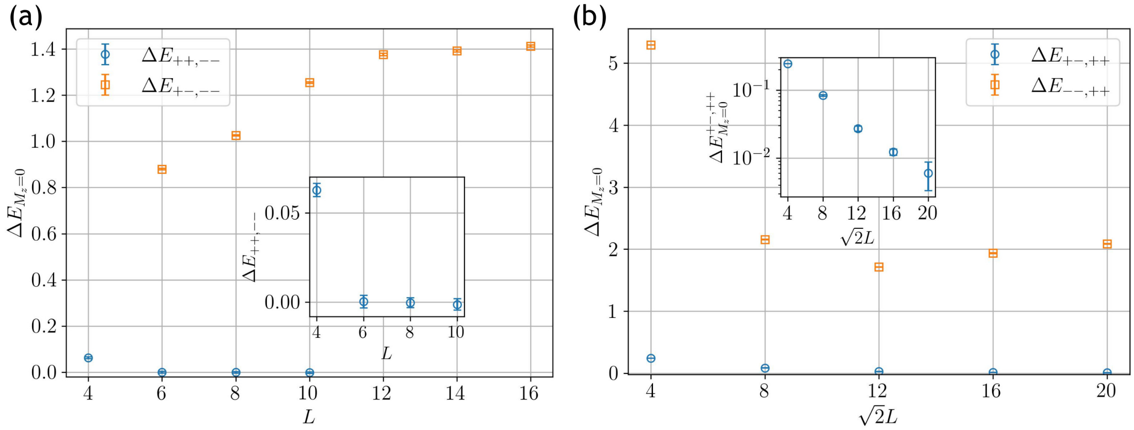

Figure 4·8: Energy gaps between the ground states in different topological sectors as a function of system size L. (a) For 0°-tilt compactification. $E_{W_x W_y, W'_x W'_y}$ labels the energy difference between sectors (W_x, W_y) and (W'_x, W'_y). For all system sizes, the sector $(-,-)$ has the lowest energy. The inset shows that the finite size gap $\Delta E_{++,--} \to 0$ as $L \to \infty$. The results indicate that the system has a two-fold TGSD. (b) For 45°-tilt compactification. The state in the $(-,-)$ sector has higher energy, and is separated from the states in the other three sectors $(+,+)$, $(+,-)$, and $(-,+)$, which are degenerate. [Note that $(+,-)$ and $(-,+)$ sectors have identical energy spectra due to the C_4 rotation symmetry of the lattice.]

4.4.1 Lowest Energy in Topological Sectors

We are interested in the lowest energy states from these four topological sectors. In particular whether their energy are degenerate or not, as this degeneracy might indicate the existence of topological order in the system.

0°-tilt compactification

In the case of 0°-tilt compactification, we observe a finite energy gap of order $\mathcal{O}(1)$ between sectors $(W_x, W_y) = (+,-)$ and $(-,-)$ for all system sizes L considered. The sectors $(+,-)$ and $(-,+)$ have identical energy spectra due to the C_4 rotation symmetry of the lattice. On the other hand, the energy difference between sectors $(+,+)$ and $(-,-)$ vanishes as L increases, with the lowest energy state in the sector

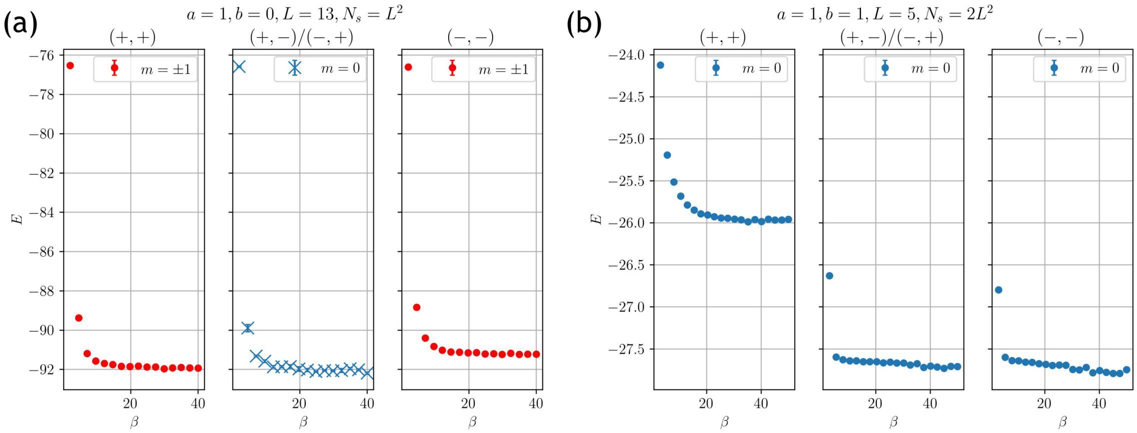

Figure 4·9: QMC results of energies in 4 topological sectors for (a) 0°-tilt with system size $L = 13$ where only the sectors (+,-) and (-,+) are compatible with zero magnetization. (b) 45°-tilt with system size $L = 5$, where the TGSD remains three as the even size system, but the degenerate sectors are (+,-) (-,+) and (-,-). N_s denotes the total number of stars on the lattice.

$(-,-)$ in all cases as shown in Fig. 4·8(a). We find that this energy difference becomes essentially zero within error bars beyond system sizes as small as $L = 6$. We conclude that the system has a two-fold degeneracy associated to sectors $(+,+)$ and $(-,-)$, to which we henceforth refer as a topological degeneracy (TGSD) distinguished by quantum numbers associated to operators (W_x, W_y) defined on non-contractible loops.

In the case of odd system size L, we find that sectors $(+,+)$ and $(-,-)$ are not compatible with even magnetization as shown in Fig. 4·9(a). Therefore, the lowest energy levels in these sectors has $M_z = \pm1$, not $M_z = 0$. These states can be split by a local longitudinal field perturbation term in the Hamiltonian. On the other hand, sectors with $(+,-)$ and $(-,+)$ are compatible with even magnetization, and the lowest energy states have $M_z = 0$. Based on the above observation, we believe that in case the topological order is present in the system, the TGSD has to come from the $(+,-)$ and $(-,+)$ sectors.

45°-tilt compactification

We repeat the studies above for the 45°-tilted lattice. The essential observation here is that the state in the $(-,-)$ sector has higher energy than the states in the other three sectors $(+,+),(+,-)$, and $(-,+)$, which are degenerate, thus yielding a three-fold TGSD for even system size L. The results are shown in Fig. 4·8(b).

In the case of odd system size, all four topological sectors are compatible with even magnetization and the lowest energy states have $M_z = 0$. As shown in Fig. 4·9(b), we find that states from $(+,-)$, $(-,+)$ and $(-,-)$ become degenerate at low temperatures ($\beta = 1/T$), indicating a three-fold TGSD. Compared to the even L case, the TGSD stays the same, but instead of the $(+,+)$ sector, the reference sector is now $(-,-)$.

Other compactifications

For other compactification schemes, we study the ground state energy in different topological sectors using ED (see Fig. 4·10). The total number of stars is $N_s = (a^2 + b^2)L^2$, and the total number of spins is $N = 2N_s$. Here, we show the results only for zero magnetization, as we find that the states with $M_z = 0$ have lower energy than other states non-zero magnetization states.

Due to size limitations to the computations, it is only possible to study compactification schemes with small values of a and b. Here we show results for three different cases: a) $a = 2, b = 1$ and $L = 2$ ($N_s = 20$); b) $a = 3, b = 1$ and $L = 1$ ($N_s = 10$); and c) $a = 3, b = 2$ and $L = 1$ ($N_s = 13$). In case (a), we find energy features similar to the 0°-tilt case with an even system size L. The lowest energy states of sectors $(+,+)$ and $(-,-)$ are well separated from the lowest energy states of $(+,-)$ and $(-,+)$ sectors, and are, possibly, the two topologically degenerate ground states, with the small energy difference between them being a finite size effect. Likewise,

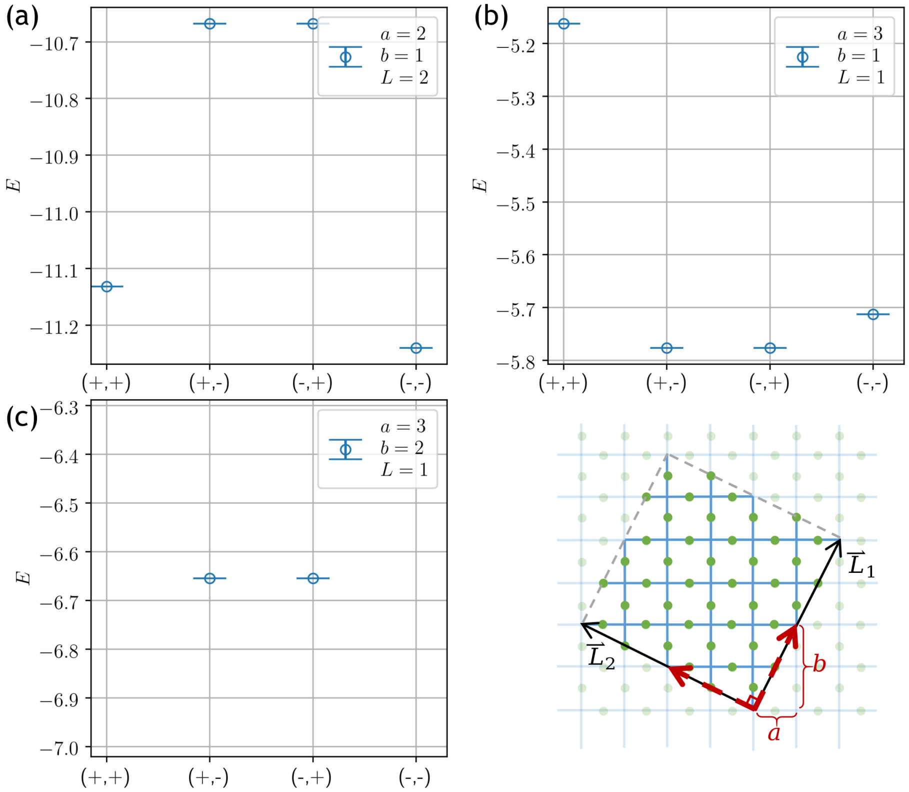

Figure 4·10: ED results for the energy of the lowest states in each topological sectors with $m = 0$ for different compactifications. (a) $a = 2, b = 1, L = 2$. (b) $a = 3, b = 1, L = 1$ (c) $a = 3, b = 2, L = 1$.

for (b), we find that the energies behave similarly to the 45°-tilt case. The $(+,-)$, $(-,+)$ and $(-,-)$ sectors contain the 3 topologically degenerate ground states, again, separated by a small finite size gap and well separated from the $(+,+)$ sector. In case (c), sectors $(+,+)$ and $(-,-)$ are incompatible with even magnetization, and states from the $(+,-)$, $(-,+)$ sectors are degenerate, similarly to the 0°-tilt case with odd system size L.

Based on the above observations, we find that the TGSD is always either 2 or 3, depending on the compactification scheme. The results can be summarized in the following way: if $(a^2 + b^2)$ is even, TGSD $= 3$; if $(a^2 + b^2)$ is odd, TGSD $= 2$. In the case of TGSD $= 3$, if L is even, the ground states belong to the $(+,+), (+,-), (-,+)$

sectors, while if L is odd, they belong to the $(-,-),(+,-),(-,+)$ sectors. In the case of TGSD $= 2$, for even L, the ground states lie in the $(+,+)$ and $(-,-)$ sectors, while for odd L, the $(+,+)$ and $(-,-)$ sectors are not compatible with zero magnetization and the ground states lie in sectors $(+,-),(-,+)$.

4.4.2 Discussion on Topolgoical order and UV/IR mixing

The results above establish numerically that the TGSD depends on the tilt angle of the compactification of the lattice. For the 0°-tilt, we find a TGSD of two (sectors $(+,+)$ and $(-,-)$), while for the 45°-tilt we find a TGSD of three (sectors $(+,+),(+,-)$, and $(-,+)$). This result is peculiar for two reasons. First, a change of the TGSD upon changing the compactification of the lattice is a clear manifestation of UV/IR mixing, a feature quite common in gapped fractonic phases. In fractonic systems the TGSD typically depends on the system size and on the relative dimensions of the lattice [56, 57, 58, 59, 60, 61, 62], while here it depends on the choice of compactification directions (vectors) defining a torus.

Second, the three-fold topological degeneracy in the 45°-tilt poses a puzzle. The $U(1)$ toric code Hamiltonian Eq. (4.11) is time-reversal symmetric. The observed three-fold topological degeneracy is quite unusual when coming from a time-reversal (T) invariant $\mathbb{Z}_2$ gauge theory. Typically, topological quantum field theories with T-symmetry are characterized by Hilbert space dimensions that are either the square of an integer or numbers that decompose into Pythagorean prime ones [107]. Neither is consistent with a degeneracy of three. One logical possibility is that the T-symmetry is spontaneously broken. If this is the case, it is not manifest through long-range magnetic order, since we find that the ground states have zero magnetization and that the spin-spin correlation functions decay exponentially.

Since we do not have an analytical solution with which to compare the numerical features that we observe, we follow a phenomenological approach to see what features the theory must have in order to be consistent with our numerical results. Let us posit the existence of non-local tunneling operators $T_{x,y}$, which are not necessarily unitary, that flip the eigenvalues of the non-local winding loop operators $W_{x,y}$. As opposed to the usual toric code, one cannot explicitly write down these operators (or at least we do not know of a way, yet).

Consider first the case of 45°-tilt compactification, and operators $T_x^{45^\circ}$ and $T_y^{45^\circ}$, depicted as a red solid-arrow and a black dashed-arrow in Fig. 4·11; these operators change the eigenvalues of W_x and W_y, respectively. The three ground states can be indexed as

$$|{+}{+}\rangle \ , \ |{-}{+}\rangle \sim T_x^{45^\circ} \ |{+}{+}\rangle \ , \ |{+}{-}\rangle \sim T_y^{45^\circ} \ |{+}{+}\rangle \ . \tag{4.15}$$

To be consistent with the numerical result, that the fourth state $|{-}{-}\rangle$, is an excited state and not yet another ground state, the application of the product $T_x^{45^\circ} T_y^{45^\circ}$ to the reference state $|{+}{+}\rangle$ must be orthogonal to the ground state manifold, or equivalently, i.e., it must annihilate the reference state in the ground state manifold,

$$T_x^{45^\circ} \, T_y^{45^\circ} \ |{+}{+}\rangle \ \sim 0 \ . \tag{4.16}$$

This scenario parallels that of $SU(2)_2$ topological order (hosting Ising anyons), where one can insert fluxes (corresponding to the tunneling operators, $T_x^{45^\circ}$ or $T_y^{45^\circ}$) through one or the other hole of the torus and switch ground states, but not insert flux through both (see, for example, Ref. [108]). The net effect is to make the fourth ground state inaccessible as in Eq. (4.16). (Refs. [109, 110] give examples of systems with $SU(2)_2$ topological order where the tunneling operators $T_{x,y}$ can be constructed and their algebra is studied.)

These tunneling operators also allow us to propose an heuristic argument that connects the topological ground state degeneracy in the two compactification schemes.

For the case of 0°-tilt compactification, the two tunneling operators $T_x^{45^\circ}$ and $T_y^{45^\circ}$ (again depicted as a red solid-arrow and a black dashed-arrow in Fig. 4·11) wind across the torus along the $+45^\circ$ and -45° directions. Along both directions, the tunneling operators flip both winding loop eigenvalues W_x and W_y, and we write the two ground states as

$$|{+}{+}\rangle \ , \ |{-}{-}\rangle \sim T_x^{45^\circ} \ |{+}{+}\rangle \ \sim T_y^{45^\circ} \ |{+}{+}\rangle \ . \tag{4.17}$$

Because both $T_x^{45^\circ}$ and $T_y^{45^\circ}$ have the same action on $|{+}{+}\rangle$, they provide us with only one additional state, $|{-}{-}\rangle$, and thus a topological ground state degeneracy of two in the 0°-tilt compactification.

Again, the argument for the exclusion of the fourth sector, $|{-}{-}\rangle$, from the ground state manifold in the case of 45°-tilt compactification parallels that in the case of Ising anyons. These arguments suggest a logical possibility that the $U(1)$ toric code may realize non-Abelian topological order. A thorough investigation of this possibility is left for future work.

4.5 Other Properties

In addition to lowest energies in different topological sectors, we also examine the dependence of the ground state properties of the lattice on a torus with various compactifications.

4.5.1 Correlation Functions

The observation of an $\mathcal{O}(1)$ energy separation between topological sectors suggests that the system is gapped. However, this observation alone does not rule out the possibility that the system is gapless within each of the $(+,+)$ and $(-,-)$ ground state sectors.

To support the claim that the system is gapped within each of these sectors, we compute the spin-spin correlation functions along the x-direction, $C(r)$, and along the 45° diagonal direction, $C_d(r)$, defined as

$$C(r) = \frac{1}{L}\sum_{\alpha} \sigma^z_{(\hat{e}_x+\alpha\hat{y})}\sigma^z_{(\hat{e}_x+\alpha\hat{y})+r\hat{x}}, \tag{4.18a}$$

$$C_d(r) = \frac{1}{L}\sum_{\alpha} \sigma^z_{(\hat{e}_x+\alpha\hat{e}_{\bar{x}y})}\sigma^z_{(\hat{e}_x+\alpha\hat{e}_{\bar{x}y})+r\hat{e}_{xy}}, \tag{4.18b}$$

where $\hat{e}_{xy} = \hat{e}_x + \hat{e}_y$, $\hat{e}_{\bar{x}y} = -\hat{e}_x + \hat{e}_y$.

0°-tilt compactification

In the case of 0°-tilt compactification, we observe that both correlation functions decay rapidly to zero within a short distance on the order of two lattice sites. The QMC results for spin-spin correlations obtained in topological sectors $(-,-)$, $(+,+)$ and $(+,-)$ are shown in Fig. 4·12. Note that the results for the sectors $(+,-)$ and $(-,+)$ are identical due to symmetry; therefore, only the results for $(+,-)$ are presented. This rapid decay is consistent with the absence of long-range magnetic order and provides evidence that the system is gapped within each topological sector.

45°-tilt compactification

In Fig. 4·13, we present the spin-spin correlation functions for 45°-tilt compactification, for all topological sectors. We again observe rapidly decaying spatial correlations, consistent with the absence of long range magnetic order.

Vanishing of certain correlators

It is a known result that a non-vanishing gap in a system with short-range interactions implies exponential decay of the two-point connected correlation functions,

$C(\vec{r}) \equiv \langle\hat{O}(0)\hat{O}(\vec{r})\rangle - \langle\hat{O}(0)\rangle\,\langle\hat{O}(\vec{r})\rangle$, for any local operator $\hat{O}$ [111]. However, the converse statement, that exponentially decaying two-point correlation functions imply the existence of a finite gap, is not necessarily true. The decay of the correlator largely depends on the excitation content captured by the chosen correlator. For example, one could have a gapless system with both gapped and gapless modes in which the chosen correlator only couples to the gapped degree of freedom, leading to an exponential decay of the correlation function. It is nonetheless common to use the exponential decay of a correlation function as a common diagnostic tool to provide numerical evidence that hints towards the existence of a non-vanishing gap. A justification is that, with exception of special cases, a simple typical operator should couple to all excitations of the system, and thus the correlator decay is dominated by the slowest decay, so its correlations would typically be power law for a gapless system. If such power law decay is not observed, it is more likely than not that the system is gapped.

Further evidence that the system we consider is a spin liquid is that a large class of operators has zero expectation value, including $\sigma^x\sigma^x$, $\sigma^y\sigma^y$ and any Pauli string with an odd number of σ^z's or σ^x's (where σ^y counts as both σ^x and σ^z). This fact, together with numerical evidence of the exponential decay of the $\langle\sigma^z(0)\sigma^z(r)\rangle$ correlator presented in the main text, is strong evidence (although not a strict proof) for the presence of a gap.

We now derive the class of Pauli strings, $\hat{P}$, for which the expectation value is exactly zero in the ground state manifold (consequently, any operator that is a linear combination of these Pauli strings will also have zero expectation value). We express $\hat{P}$ as a product of only σ^x's and σ^z's, by replacing σ^y with $i\sigma^z\sigma^x$. Next, let us use the fact that any ground state has all $B_p = +1$. This implies that unless all σ^x's in the Pauli string form closed loops on the dual lattice, $\hat{P}$ anticommutes with some B_p and therefore $\langle \hat{P} \rangle = 0$. As an simple example, consider the expectation value of $\hat{P} = \sigma_i^x$ at site i, and ground state $|g\rangle$. Using the fact that $B_p |g\rangle = |g\rangle$ we have the following

$$\langle \sigma_i^x | \sigma_i^x \rangle = \langle g | \sigma_i^x | g \rangle \tag{4.19}$$

$$= \langle g | B_p \, \sigma_i^x \, B_p | g \rangle \tag{4.20}$$

$$= \langle g | B_p \, (-B_p \, \sigma_i^x) | g \rangle \tag{4.21}$$

$$= - \langle \sigma_i^x | \sigma_i^x \rangle \, . \tag{4.22}$$

Therefore we have $\langle \sigma_i^x | \sigma_i^x \rangle = - \langle \sigma_i^x | \sigma_i^x \rangle = 0$.

This implies that a necessary condition for the non-vanishing expectation value is that there is an even number of σ^x's in the Pauli string. Further, note that in the ground state manifold the Hamiltonian commutes with the operator $F^x \equiv \prod_i \sigma_i^x$ (a global spin flip), since $M_z = 0$. Therefore, a Pauli string with an odd number of σ^z's (and an even number of σ^x) would anticommute with F^x and have zero expectation value. To sum up, the only Pauli strings that potentially might have a non-zero expectation value are the ones with an even number of σ^z's and where all σ^x's form closed loops (where σ^z and σ^x can potentially be applied to the same site to form σ^y).

4.5.2 Symmetry Breaking

For both 0°-tilt and 45°-tilt compactifications, we further measures the star-star correlator $\langle \mathcal{A}_s \, \mathcal{A}_{s'} \rangle$.

Interestingly, In 0°-tilt case, we observe a spatial checkerboard pattern in the measurements as shown in Fig. 4·14(a). This pattern suggests that the ground states spontaneously break translation symmetry. This staggered pattern appears in both degenerate topological sectors $(-,-)$ and $(+,+)$, indicating the coexistence of spontaneous symmetry breaking with topological degeneracy, i.e., the total ground state degeneracy is 4, the product of the two-fold TGSD by a factor of 2 originating from the symmetry breaking. Note that this additional degeneracy is not topological and can be lifted by local perturbations.

In the 45°-tilt compactification scheme we also observe that the star-star correlators $\langle \mathcal{A}_s\, \mathcal{A}_{s'} \rangle$ present a staggered pattern, similar to what we observed for the 0°-tilt case and showed in Fig. 4·14(b). This provides evidence that within each topological sector we have a two-fold degeneracy associated to spontaneous translation symmetry breaking. Accounting for this additional factor of 2, the total ground state space is 6-fold degenerate.

4.6 Proposal for Experimental Realization

Here we illustrate how the four-spin interaction term $\mathcal{A}_s$ in our Hamiltonian in Eq. (4.5) appears naturally in a physical set-up proposed in Ref. [91] using arrays of superconducting quantum wires coupled via Josephson junctions. Consider, for each star s, a 4×4 array of vertical and horizontal wires intersecting at 16 crossings, as depicted in Fig. 4·15. Each of the four vertical wires $n = 1, \ldots, 4$ is coupled to each of the four horizontal wires $i = 1, \ldots, 4$ by a Josephson junction. The sign of each coupling is encapsulated by a matrix W with diagonal elements $W_{n=i} = -1$ (corresponding to a π-junction) and off-diagonal elements $W_{n\neq i} = +1$ (corresponding to a regular junction).

The Hamiltonian at a given site s for such a system is given by

$$H = H_J + H_K \tag{4.23a}$$

with

$$H_J = -J \sum_{n,i} W_{ni}\; \cos(\phi_n - \theta_i) \tag{4.23b}$$

and

$$H_K = \frac{1}{2C_\mathrm{m}} \sum_n q_n^2 + \frac{1}{2C_\mathrm{g}} \sum_i Q_i^2 \,, \tag{4.23c}$$

where C_m and C_g are the self-capacitances. ϕ_n and θ_i are the superconducting phases in each wire and q_n and Q_i are their conjugate charges, respectively. On the lattice, we refer to the ϕ as "matter" phases and they are not connected to wires on any other site. On the other hand, we refer to the θ as "gauge" phases and they are shared by neighboring sites. (Here we focus on a single star; on a lattice, gauge wires are shared between neighboring stars.)

The form of the W-matrix guarantees that this Hamiltonian has local Z_2 symmetry, per combinatorial gauge symmetry (CGS). At the same time, this Hamiltonian also has global $U(1)$ symmetry, hence it is a natural starting point for the $U(1)$ toric code.

There are two types of limits that one usually considers in Josephson junction Hamiltonians – phase and charge. The former is dominated by large J where the flux is typically treated classically and then one considers the quantum fluctuations perturbatively. We are interested in the opposite charging limit, where both capacitances are small and we are in the quantum regime at the outset. To treat this case we will proceed in two steps: first take the limit of small C_m and then small C_g.

Small C_m limit: first, we add a bias voltage $\bar{q}$ to each matter wire so that the kinetic term becomes

$$\frac{1}{2C_\mathrm{m}} \left(q_n - \bar{q}\right)^2 \,. \tag{4.24}$$

If the bias is close to $\bar{q} = N + 1/2$ (N is an integer) such that two quantized states $q_n = N$ and $q_n = N + 1$ are close in energy, then the matter wires become two-level systems, because the small capacitance penalizes all other charge states. For our purposes we consider a gate bias very close to the half integer point. At this point the operators $e^{\pm\imath\phi_n}$ increase or decrease the charge value and we can replace them by ordinary spin raising/lowering operators $e^{\pm\imath\phi_n} \to \mu_n^{\pm}$, where $\mu_n^{\pm} = \mu_n^{\mathrm{x}} \pm \imath\mu_n^{\mathrm{y}}$. [112]. The Hamiltonian (4.23b) in this limit becomes

$$H_J = -J \sum_{n,i} W_{ni} \left(\mu_n^+ \, e^{+\imath\theta_i} + \mu_n^- \, e^{-\imath\theta_i}\right) \,. \tag{4.25}$$

The μ spins can be integrated out exactly by diagonalizing, for each n, a 2×2 spin-1/2 Hamiltonian (treating the θ_i's as slow fields). Keeping only the lowest energy terms, the result is an effective potential as a function of θ_i's only:

$$H_J^{\mathrm{eff}} = -|J| \sum_n \left[\sum_{i,j} W_{ni} W_{nj} \cos(\theta_i - \theta_j)\right]^{1/2} \,. \tag{4.26}$$

Notice that this Hamiltonian still has the global $U(1)$ symmetry as well as the discrete Z_2 symmetry, which we can write as:

$$\theta_i \to \theta_i + \frac{\pi}{2}(1-\sigma_i^{\mathrm{z}}), \;\; \sigma_i^{\mathrm{z}} = \pm1, \text{ if } \sigma_1^{\mathrm{z}}\,\sigma_2^{\mathrm{z}}\,\sigma_3^{\mathrm{z}}\,\sigma_4^{\mathrm{z}} = +1\,. \tag{4.27}$$

Small C_g limit: now we will follow a similar procedure with the gauge wires and add a bias $\bar{Q} = M + 1/2$ (M is an integer) to all Q_i. This restricts the charge on each gauge wire to two values.

Mathematically, however, we take a different approach. Rather than replacing the flux operators by Pauli matrices immediately, we will first expand Eq. (4.26) in a Fourier series, keeping only the terms $e^{\pm\imath\theta_i}$, i.e., those that change the charge from one to zero or vice versa on each wire. It is straightforward to check that the only terms that appear in the Fourier expansion have the form of $\mathcal{A}_s$ in Eq. (4.5) but with each spin operator $\sigma_i^{\pm}$ standing for $e^{\pm\imath\theta_i}$.

We note that this procedure realizes the star term $\mathcal{A}_s$, but we do not generate the plaquette term B_p. It remains a problem for future work to systematically study different sectors with given eigenvalues of B_p to determine whether the ground states of Hamiltonian Eq. (4.11) with $\lambda_B = 0$ remain those in the sector with $B_p = +1$ for all p, which were justified in our quantum Monte Carlo studies by the presence of the sufficiently large λ_B coupling in the Hamiltonian.

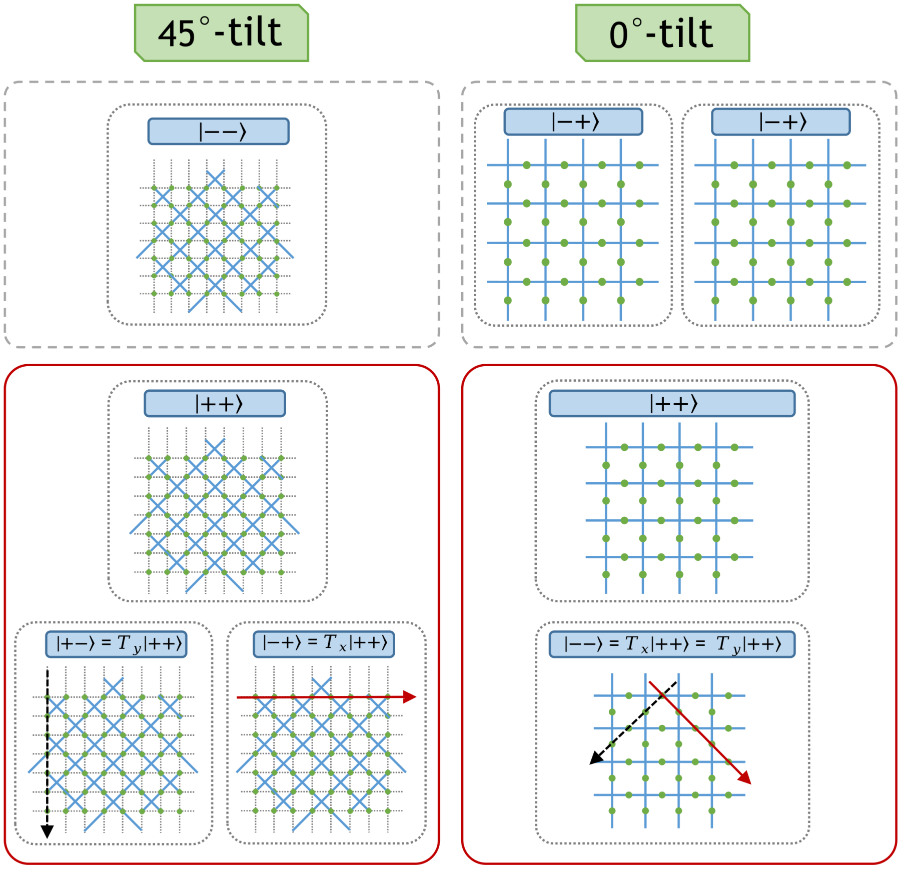

Figure 4·11: Mapping between topological sectors in 0°-tilt (right side) and 45°-tilt (left side) compactifications. The ground state manifold is depicted with the red frames, while topological sectors with excited lowest energy states are depicted with gray dashed frames. We assume existence of non-local and non-unitary tunneling operators, $T_x^{45^\circ}$ (red arrows) and $T_y^{45^\circ}$ (dashed black arrows), that in the 45°-tilt case take the state $|{+}{+}\rangle$ to states $|{-}{+}\rangle$ and $|{+}{-}\rangle$, respectively. Simultaneous application of both tunneling operators to $|{+}{+}\rangle$ annihilates the state, and therefore $|{-}{-}\rangle$ does not belong to the ground state manifold. In the 0°-tilt case, assuming the same orientation of the tunneling operators with respect to the microscopic details of the lattice, both $T_x^{45^\circ}$ and $T_y^{45^\circ}$ take state $|{+}{+}\rangle$ to $|{-}{-}\rangle$, and hence states $|{+}{-}\rangle$, $|{-}{+}\rangle$ remain out of the ground state manifold.

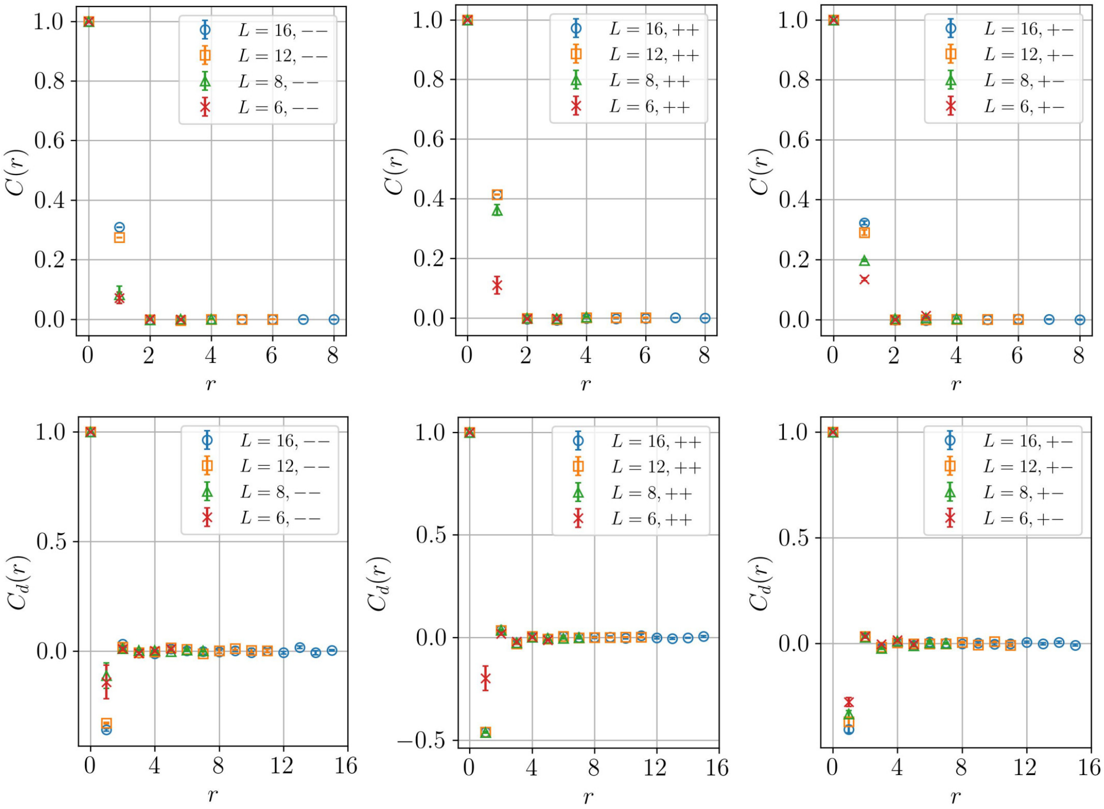

Figure 4·12: Spin-spin correlation functions in the x- and 45°-directions ($C(r)$ and $C_d(r)$, respectively) are shown for different system sizes, L. The results are presented from left to right for the $(-,-)$, $(+,+)$, and $(+,-)$ topological sectors. The correlation functions decay to zero rapidly, indicating that the system is gapped for all topological sectors.

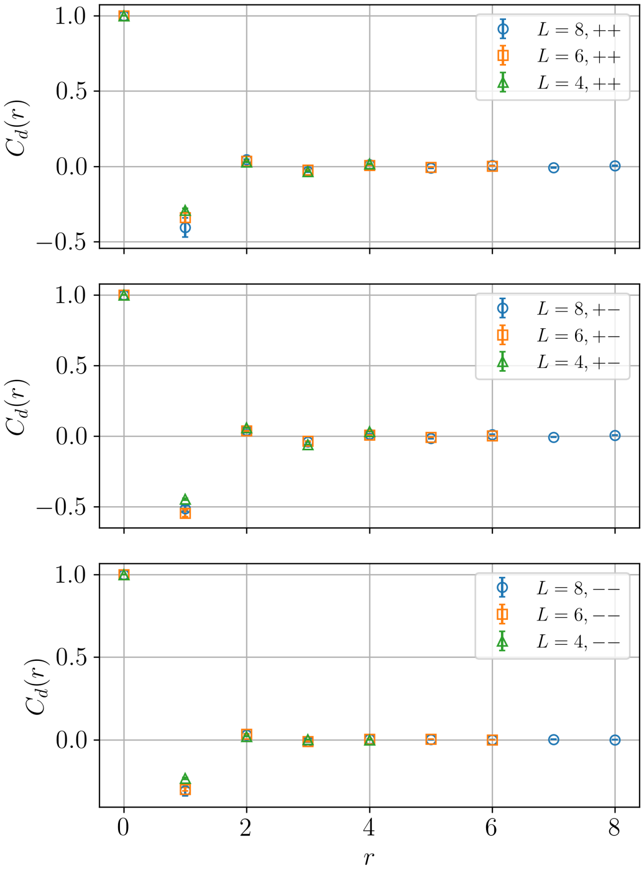

Figure 4·13: Spin-spin correlation functions in the topological sectors $(+,+)$, $(+,-)/(-,+)$ and $(-,-)$ for the 45°-tilt setup. All the results shows a fast decaying within the order of two lattice sites for all system sizes L.

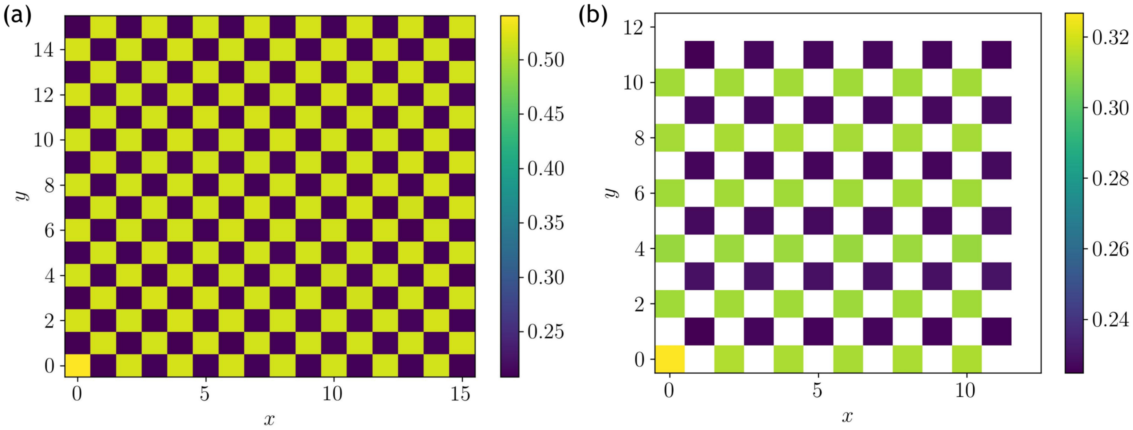

Figure 4·14: Intensity plot of the star-star correlation $\left\langle \mathcal{A}_{s=(0,0)}\ \mathcal{A}_{s'=(x,y)} \right\rangle$, indicating translational symmetry breaking. (a) Result for 0°-tilt compactification, in the sector $(-,-)$ and with $M_z = 0$. The system size is $L = 16$. (b) Result for 45°-tilt compactification, in the sector $(+,+)$ and with $M_z = 0$. The system size is $L = 12$.

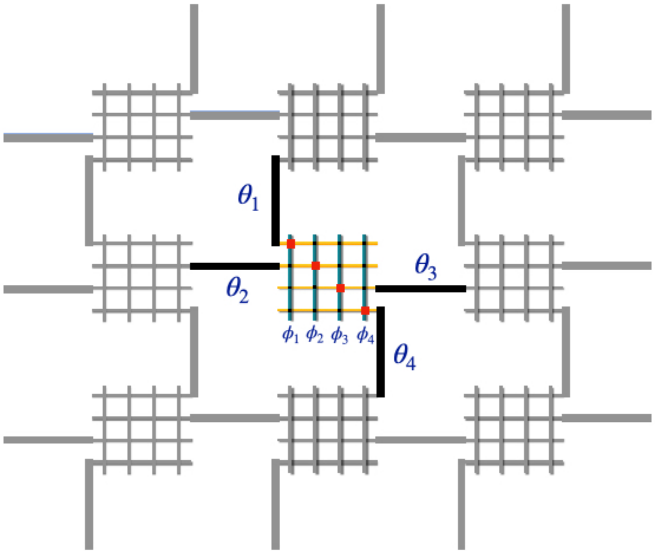

Figure 4·15: A proposed physical realization of the star term $\mathcal{A}_s$ in the $U(1)$ toric code lattice Hamiltonian. The center "waffle" is highlighted as an example. It is composed of intersecting superconducting wires coupled by Josephson junctions. The junctions in the diagonal (red) denote π couplings. Vertical wires (blue) are "matter" degrees of freedom labeled by phase ϕ_n. Horizontal wires (gold) are "gauge" degrees of freedom with phases θ_i. Only the gauge degrees of freedom (black) couple to other, neighboring, waffles.

Chapter 5

Conclusion and Future Directions

In this dissertation, we focus on the study of two quantum spin-1/2 lattice models with local Z_2 gauge symmetry using unbiased numerical methods.

In the Z_2 CGS models, we have presented a numerical study of spin models with only one- and two-spin interactions that realize a combinatorial Z_2 gauge symmetry. We considered two models that only differ by the kinetic terms given to the gauge spins: model-X (containing a transverse field) and model-XX (containing XX interactions). We found conclusive evidence for an extended Z_2 topological quantum spin liquid phase in both models.

In the case of model-X, we identified two phases; a topological phase and a paramagnetic phase. We demonstrated a first-order quantum phase transition between these phases, in contrast to the well known continuous transition of the conventional Z_2 lattice gauge model. In model-XX we identified a topological phase and a competing ferromagnetic state. Our data also support a first-order transition between these two phases in model-XX. Perturbatively, the XX interaction of model-XX generates a plaquette operator G_p at a lower order in perturbation theory as compared to the transverse field of model-X, and therefore the size of the vison gap increases, as we also observe.

The presence of the first-order transition between the topological and the competing state, in both models, raises the following interesting question: As we have discussed in the paper, in the limit of a large transverse field Γ_m on the matter spins, the models map to the usual Ising gauge model, which has a continuous transition. An important question is then whether the continuous transition persists for some finite range of values of Γ_m, or whether it turns first-order immediately. This question can in principle be answered by considering the corrections to the usual Z_2 gauge model in Eq. (3.12), which will appear when carrying out a perturbative expansion to higher order in Γ_m^{-1}. The question is then whether these corrections are renormalization-group relevant or irrelevant at the critical point. While we have not carried out this expansion and duality mapping, it appears likely that the additional interactions generated in the Ising model will involve products of more than two spins, and most likely these interactions will be irrelevant at the Ising critical point. Thus, we suspect that there will be indeed a tricritical point separating continuous Ising transitions and first-order transitions for large values of Γ_m in Figs. 3·7 and 3·13. We leave tests of this hypothesis open for future work.

In the case of $U(1)$ toric code, the model is invariant under both a global $U(1)$ symmetry and local Z_2 gauge transformations. We presented evidence that the system is gapped and the $U(1)$ global symmetry is not spontaneously broken. The exponential decay of spin-spin correlators support the claim that the system is a gapped spin liquid. We found topologically degenerate ground states, labeled by non-contractible string operators.

The model displays quite distinct topological degeneracies that depend on the tilt of the lattice that is wrapped around the torus, a form of UV/IR mixing unlike those encountered, for example, in fractonic models. The number of degenerate ground states is also puzzling. It is difficult to explain the three-fold topological degeneracy for the 45°-tilt compactification as coming from Abelian topological order if the $U(1)$ toric code is described by a doubled theory (for example, the usual toric code which is described by a doubled Chern-Simons theory).

One logical possibility is that the enrichment of the Z_2 toric code by the global $U(1)$ symmetry may turn the topological order non-Abelian. We presented an heuristic argument aimed at relating the three-fold topological degeneracy for the 45°-tilt compactification to the two-fold topological degeneracy for the 0°-tilt compactification based on a mapping of posited logical operators that switch between topological ground states in both geometries.

Finally, we presented a physical realization of the $U(1)$-symmetric star terms in the Hamiltonian in a system of superconducting quantum wires coupled by Josephson junctions at their crossings. We believe that the possibility that the model may be realizable with physical Hamiltonians should further motivate future theoretical studies of the unusual topological properties of the $U(1)$ toric code.

References

[1] X.-G. Wen, "Topological order: From long-range entangled quantum matter to a unified origin of light and electrons," *International Scholarly Research Notices*, vol. 2013, 2013.

[2] F. J. Wegner, "Duality in generalized ising models and phase transitions without local order parameters," *Journal of Mathematical Physics*, vol. 12, no. 10, pp. 2259–2272, 1971.

[3] X. G. Wen, "Vacuum degeneracy of chiral spin states in compactified space," *Phys. Rev. B*, vol. 40, pp. 7387–7390, Oct 1989.

[4] X. G. Wen, "Topological orders in rigid states," *International Journal of Modern Physics B*, vol. 04, no. 02, pp. 239–271, 1990.

[5] X. G. Wen and Q. Niu, "Ground-state degeneracy of the fractional quantum hall states in the presence of a random potential and on high-genus riemann surfaces," *Phys. Rev. B*, vol. 41, pp. 9377–9396, May 1990.

[6] A. Kitaev, "Fault-tolerant quantum computation by anyons," *Annals of Physics*, vol. 303, no. 1, pp. 2–30, 2003.

[7] J. B. Kogut, "An introduction to lattice gauge theory and spin systems," *Rev. Mod. Phys.*, vol. 51, pp. 659–713, Oct 1979.

[8] S. Zhou, M. Zelenayova, O. Hart, C. Chamon, and C. Castelnovo, "Probing fractional statistics in quantum simulators of spin liquid Hamiltonians," *arXiv e-prints*, p. arXiv:2211.09784, Nov. 2022.

[9] R. Moessner and S. L. Sondhi, "Resonating valence bond phase in the triangular lattice quantum dimer model," *Phys. Rev. Lett.*, vol. 86, pp. 1881–1884, Feb 2001.

[10] G. Misguich, D. Serban, and V. Pasquier, "Quantum dimer model on the kagome lattice: Solvable dimer-liquid and ising gauge theory," *Phys. Rev. Lett.*, vol. 89, p. 137202, Sep 2002.

[11] L. Balents, M. P. A. Fisher, and S. M. Girvin, "Fractionalization in an easy-axis kagome antiferromagnet," *Phys. Rev. B*, vol. 65, p. 224412, May 2002.

[12] S. V. Isakov, Y. B. Kim, and A. Paramekanti, "Spin-liquid phase in a spin-1/2 quantum magnet on the kagome lattice," *Phys. Rev. Lett.*, vol. 97, p. 207204, Nov 2006.

[13] S. V. Isakov, A. Paramekanti, and Y. B. Kim, "Exotic phase diagram of a cluster charging model of bosons on the kagome lattice," *Phys. Rev. B*, vol. 76, p. 224431, Dec 2007.

[14] C. Chamon, D. Green, and Z.-C. Yang, "Constructing quantum spin liquids using combinatorial gauge symmetry," *Phys. Rev. Lett.*, vol. 125, p. 067203, Aug 2020.

[15] S. Zhou, D. Green, E. D. Dahl, and C. Chamon, "Experimental realization of spin liquids in a programmable quantum device," 2020.

[16] A. W. Sandvik, "Computational studies of quantum spin systems," *AIP Conf. Proc.*, vol. 1297, no. 1, pp. 135–338, 2010.

[17] H. Rieger and N. Kawashima, "Application of a continuous time cluster algorithm to the two-dimensional random quantum ising ferromagnet," *Eur. Phys. J. B - Condensed Matter and Complex Systems*, vol. 9, pp. 233–236, May 1999.

[18] M. S. L. du Croo de Jongh and J. M. J. van Leeuwen, "Critical behavior of the two-dimensional ising model in a transverse field: A density-matrix renormalization calculation," *Phys. Rev. B*, vol. 57, pp. 8494–8500, Apr 1998.

[19] C.-W. Liu, A. Polkovnikov, and A. W. Sandvik, "Quasi-adiabatic quantum monte carlo algorithm for quantum evolution in imaginary time," *Phys. Rev. B*, vol. 87, p. 174302, May 2013.

[20] E. Fradkin, *Field Theories of Condensed Matter Physics.* Cambridge University Press, 2 ed., 2013.

[21] A. W. Sandvik, "Stochastic series expansion method for quantum ising models with arbitrary interactions," *Phys. Rev. E*, vol. 68, p. 056701, Nov 2003.

[22] W.-L. You, Y.-W. Li, and S.-J. Gu, "Fidelity, dynamic structure factor, and susceptibility in critical phenomena," *Phys. Rev. E*, vol. 76, p. 022101, Aug 2007.

[23] S.-J. Gu, "Fidelity approach to quantum phase transitions," *Int. J. Mod. Phys. B*, vol. 24, no. 23, pp. 4371–4458, 2010.

[24] P. Prelovšek and J. Bonča, *Ground State and Finite Temperature Lanczos Methods*, pp. 1–30. Berlin, Heidelberg: Springer Berlin Heidelberg, 2013.

[25] A. W. Sandvik, *Stochastic Series Expansion Methods.* Verlag des Forschungszentrum Julich, 2019.

[26] L. Wang, Y.-H. Liu, J. Imriška, P. N. Ma, and M. Troyer, "Fidelity susceptibility made simple: A unified quantum monte carlo approach," *Phys. Rev. X*, vol. 5, p. 031007, Jul 2015.

[27] K. Hukushima and K. Nemoto, "Exchange monte carlo method and application to spin glass simulations," *J. Phys. Soc. Jpn.*, vol. 65, no. 6, pp. 1604–1608, 1996.

[28] K. Hukushima, H. Takayama, and K. Nemoto, "Application of an extended ensemble method to spin glasses," *Int. J. Mod. Phys. C*, vol. 07, no. 03, pp. 337–344, 1996.

[29] P. Sengupta, A. W. Sandvik, and D. K. Campbell, "Bond-order-wave phase and quantum phase transitions in the one-dimensional extended hubbard model," *Phys. Rev. B*, vol. 65, p. 155113, Apr 2002.

[30] S. Elitzur, "Impossibility of spontaneously breaking local symmetries," *Phys. Rev. D*, vol. 12, pp. 3978–3982, Dec 1975.

[31] R. Kotecký, "Statistical field theory,volume 1: From brownian motion to renormalization and lattice gauge theory,volume 2: Strong coupling, monte carlo methods, conformal field theory, and random systems," *Astrophys. Space Sci.*, vol. 193, pp. 163–163, Jul 1992.

[32] N. Xu, C. Castelnovo, R. G. Melko, C. Chamon, and A. W. Sandvik, "Dynamic scaling of topological ordering in classical systems," *Phys. Rev. B*, vol. 97, p. 024432, Jan 2018.

[33] M. E. Fisher and A. N. Berker, "Scaling for first-order phase transitions in thermodynamic and finite systems," *Phys. Rev. B*, vol. 26, pp. 2507–2513, Sep 1982.

[34] K. Binder and D. P. Landau, "Finite-size scaling at first-order phase transitions," *Phys. Rev. B*, vol. 30, pp. 1477–1485, Aug 1984.

[35] A. Sen and A. W. Sandvik, "Example of a first-order néel to valence-bond-solid transition in two dimensions," *Phys. Rev. B*, vol. 82, p. 174428, Nov 2010.

[36] B. Zhao, P. Weinberg, and A. W. Sandvik, "Symmetry-enhanced discontinuous phase transition in a two-dimensional quantum magnet," *Nat. Phys.*, vol. 15, pp. 678–682, Jul 2019.

[37] K. Vollmayr, J. D. Reger, M. Scheucher, and K. Binder, “Finite size effects at thermally-driven first order phase transitions: A phenomenological theory of the order parameter distribution,” *Z. Phys. B Condensed Matter*, vol. 91, pp. 113–125, Mar 1993.

[38] S. Iino, S. Morita, N. Kawashima, and A. W. Sandvik, “Detecting signals of weakly first-order phase transitions in two-dimensional potts models,” *J. Phys. Soc. Jpn.*, vol. 88, no. 3, p. 034006, 2019.

[39] O. Hart, Y. Wan, and C. Castelnovo, “Correlation holes and slow dynamics induced by fractional statistics in gapped quantum spin liquids,” *Nat. Commun.*, vol. 12, Mar. 2021.

[40] N. Read and B. Chakraborty, “Statistics of the excitations of the resonating-valence-bond state,” *Phys. Rev. B*, vol. 40, pp. 7133–7140, Oct 1989.

[41] N. Read and S. Sachdev, “Large-n expansion for frustrated quantum antiferromagnets,” *Phys. Rev. Lett.*, vol. 66, pp. 1773–1776, Apr 1991.

[42] X. G. Wen, “Mean-field theory of spin-liquid states with finite energy gap and topological orders,” *Phys. Rev. B*, vol. 44, pp. 2664–2672, Aug 1991.

[43] L. Balents, M. P. A. Fisher, and C. Nayak, “Dual order parameter for the nodal liquid,” *Phys. Rev. B*, vol. 60, pp. 1654–1667, Jul 1999.

[44] T. Senthil and M. P. A. Fisher, “Z_2 gauge theory of electron fractionalization in strongly correlated systems,” *Phys. Rev. B*, vol. 62, pp. 7850–7881, Sep 2000.

[45] R. Moessner, S. L. Sondhi, and E. Fradkin, “Short-ranged resonating valence bond physics, quantum dimer models, and ising gauge theories,” *Phys. Rev. B*, vol. 65, p. 024504, Dec 2001.

[46] M. A. Levin and X.-G. Wen, “String-net condensation: A physical mechanism for topological phases,” *Phys. Rev. B*, vol. 71, p. 045110, Jan 2005.

[47] L. Savary and L. Balents, “Quantum spin liquids: a review,” *Reports on Progress in Physics*, vol. 80, p. 016502, nov 2016.

[48] C. Broholm, R. J. Cava, S. A. Kivelson, D. G. Nocera, M. R. Norman, and T. Senthil, “Quantum spin liquids,” *Science*, vol. 367, no. 6475, p. eaay0668, 2020.

[49] D. C. Tsui, H. L. Stormer, and A. C. Gossard, “Two-dimensional magnetotransport in the extreme quantum limit,” *Phys. Rev. Lett.*, vol. 48, pp. 1559–1562, May 1982.

[50] R. B. Laughlin, “Anomalous quantum hall effect: An incompressible quantum fluid with fractionally charged excitations,” *Phys. Rev. Lett.*, vol. 50, pp. 1395–1398, May 1983.

[51] S. C. Zhang, T. H. Hansson, and S. Kivelson, “Effective-field-theory model for the fractional quantum hall effect,” *Phys. Rev. Lett.*, vol. 62, pp. 82–85, Jan 1989.

[52] A. Stern, “Anyons and the quantum hall effecta pedagogical review,” *Annals of Physics*, vol. 323, no. 1, pp. 204–249, 2008. January Special Issue 2008.

[53] T. Hansson, V. Oganesyan, and S. Sondhi, “Superconductors are topologically ordered,” *Annals of Physics*, vol. 313, no. 2, pp. 497–538, 2004.

[54] E. Witten, “Topological Quantum Field Theory,” *Commun. Math. Phys.*, vol. 117, p. 353, 1988.

[55] E. Witten, “Quantum Field Theory and the Jones Polynomial,” *Commun. Math. Phys.*, vol. 121, pp. 351–399, 1989.

[56] C. Chamon, “Quantum glassiness in strongly correlated clean systems: An example of topological overprotection,” *Phys. Rev. Lett.*, vol. 94, p. 040402, Jan 2005.

[57] S. Bravyi, B. Leemhuis, and B. M. Terhal, “Topological order in an exactly solvable 3d spin model,” *Annals of Physics*, vol. 326, no. 4, pp. 839–866, 2011.

[58] J. Haah, “Local stabilizer codes in three dimensions without string logical operators,” *Phys. Rev. A*, vol. 83, p. 042330, Apr 2011.

[59] B. Yoshida, “Exotic topological order in fractal spin liquids,” *Phys. Rev. B*, vol. 88, p. 125122, Sep 2013.

[60] J. Haah, “Commuting pauli hamiltonians as maps between free modules,” *Communications in Mathematical Physics*, vol. 324, no. 2, pp. 351–399, 2013.

[61] S. Vijay, J. Haah, and L. Fu, “A new kind of topological quantum order: A dimensional hierarchy of quasiparticles built from stationary excitations,” *Phys. Rev. B*, vol. 92, p. 235136, Dec 2015.

[62] S. Vijay, J. Haah, and L. Fu, “Fracton topological order, generalized lattice gauge theory, and duality,” *Phys. Rev. B*, vol. 94, p. 235157, Dec 2016.

[63] M. Pretko, X. Chen, and Y. You, “Fracton phases of matter,” *International Journal of Modern Physics A*, vol. 35, no. 06, p. 2030003, 2020.

[64] N. Seiberg and S.-H. Shao, “Exotic symmetries, duality, and fractons in 2+1-dimensional quantum field theory,” *SciPost Phys.*, vol. 10, p. 027, 2021.

[65] N. Seiberg and S.-H. Shao, “Exotic $U(1)$ symmetries, duality, and fractons in 3+1-dimensional quantum field theory,” *SciPost Phys.*, vol. 9, p. 046, 2020.

[66] C. L. Kane and E. J. Mele, “Quantum spin hall effect in graphene,” *Phys. Rev. Lett.*, vol. 95, p. 226801, Nov 2005.

[67] C. L. Kane and E. J. Mele, “Z_2 topological order and the quantum spin hall effect,” *Phys. Rev. Lett.*, vol. 95, p. 146802, Sep 2005.

[68] B. A. Bernevig, T. L. Hughes, and S.-C. Zhang, “Quantum spin hall effect and topological phase transition in hgte quantum wells,” *Science*, vol. 314, no. 5806, pp. 1757–1761, 2006.

[69] J. E. Moore and L. Balents, “Topological invariants of time-reversal-invariant band structures,” *Phys. Rev. B*, vol. 75, p. 121306, Mar 2007.

[70] L. Fu, C. L. Kane, and E. J. Mele, “Topological insulators in three dimensions,” *Phys. Rev. Lett.*, vol. 98, p. 106803, Mar 2007.

[71] R. Roy, “Topological phases and the quantum spin hall effect in three dimensions,” *Phys. Rev. B*, vol. 79, p. 195322, May 2009.

[72] Y. Ando, “Topological insulator materials,” *Journal of the Physical Society of Japan*, vol. 82, no. 10, p. 102001, 2013.

[73] M. Sato and Y. Ando, “Topological superconductors: a review,” *Reports on Progress in Physics*, vol. 80, p. 076501, may 2017.

[74] W. P. Su, J. R. Schrieffer, and A. J. Heeger, “Solitons in polyacetylene,” *Phys. Rev. Lett.*, vol. 42, pp. 1698–1701, Jun 1979.

[75] F. Haldane, “Continuum dynamics of the 1-d heisenberg antiferromagnet: Identification with the o(3) nonlinear sigma model,” *Physics Letters A*, vol. 93, no. 9, pp. 464–468, 1983.

[76] I. Affleck, T. Kennedy, E. H. Lieb, and H. Tasaki, “Rigorous results on valence-bond ground states in antiferromagnets,” *Phys. Rev. Lett.*, vol. 59, pp. 799–802, Aug 1987.

[77] X. Chen, Z.-C. Gu, Z.-X. Liu, and X.-G. Wen, “Symmetry-protected topological orders in interacting bosonic systems,” *Science*, vol. 338, no. 6114, pp. 1604–1606, 2012.

[78] X.-G. Wen, "Quantum orders and symmetric spin liquids," *Phys. Rev. B*, vol. 65, p. 165113, Apr 2002.

[79] M. Levin and A. Stern, "Classification and analysis of two-dimensional abelian fractional topological insulators," *Phys. Rev. B*, vol. 86, p. 115131, Sep 2012.

[80] A. M. Essin and M. Hermele, "Classifying fractionalization: Symmetry classification of gapped $\mathbb{Z}_2$ spin liquids in two dimensions," *Phys. Rev. B*, vol. 87, p. 104406, Mar 2013.

[81] L.-Y. Hung and X.-G. Wen, "Quantized topological terms in weak-coupling gauge theories with a global symmetry and their connection to symmetry-enriched topological phases," *Phys. Rev. B*, vol. 87, p. 165107, Apr 2013.

[82] A. Mesaros and Y. Ran, "Classification of symmetry enriched topological phases with exactly solvable models," *Phys. Rev. B*, vol. 87, p. 155115, Apr 2013.

[83] C.-Y. Huang, X. Chen, and F. Pollmann, "Detection of symmetry-enriched topological phases," *Phys. Rev. B*, vol. 90, p. 045142, Jul 2014.

[84] Y.-M. Lu and A. Vishwanath, "Classification and properties of symmetry-enriched topological phases: Chern-simons approach with applications to Z_2 spin liquids," *Phys. Rev. B*, vol. 93, p. 155121, Apr 2016.

[85] M. Cheng, Z.-C. Gu, S. Jiang, and Y. Qi, "Exactly solvable models for symmetry-enriched topological phases," *Phys. Rev. B*, vol. 96, p. 115107, Sep 2017.

[86] Q.-R. Wang and M. Cheng, "Exactly solvable models for u(1) symmetry-enriched topological phases," *Phys. Rev. B*, vol. 106, p. 115104, Sep 2022.

[87] A. Kitaev, "Periodic table for topological insulators and superconductors," *AIP Conference Proceedings*, vol. 1134, no. 1, pp. 22–30, 2009.

[88] X. Chen, F. J. Burnell, A. Vishwanath, and L. Fidkowski, "Anomalous symmetry fractionalization and surface topological order," *Phys. Rev. X*, vol. 5, p. 041013, Oct 2015.

[89] N. Tarantino, N. H. Lindner, and L. Fidkowski, "Symmetry fractionalization and twist defects," *New Journal of Physics*, vol. 18, p. 035006, mar 2016.

[90] M. Barkeshli, P. Bonderson, M. Cheng, and Z. Wang, "Symmetry fractionalization, defects, and gauging of topological phases," *Phys. Rev. B*, vol. 100, p. 115147, Sep 2019.

[91] C. Chamon, D. Green, and A. J. Kerman, "Superconducting circuit realization of combinatorial gauge symmetry," *PRX Quantum*, vol. 2, p. 030341, Sep 2021.

[92] K.-H. Wu, Z.-C. Yang, D. Green, A. W. Sandvik, and C. Chamon, "z_2 topological order and first-order quantum phase transitions in systems with combinatorial gauge symmetry," *Phys. Rev. B*, vol. 104, p. 085145, Aug 2021.

[93] D. Green and C. Chamon, "Constructing non-abelian quantum spin liquids using combinatorial gauge symmetry," *arXiv preprint arXiv:2209.14333*, 2022.

[94] H. Yu, G. Goldstein, D. Green, A. E. Ruckenstein, and C. Chamon, "Abelian combinatorial gauge symmetry," *arXiv preprint arXiv:2212.03880*, 2022.

[95] M. Levin, F. J. Burnell, M. Koch-Janusz, and A. Stern, "Exactly soluble models for fractional topological insulators in two and three dimensions," *Phys. Rev. B*, vol. 84, p. 235145, Dec 2011.

[96] A. W. Sandvik and J. Kurkijärvi, "Quantum monte carlo simulation method for spin systems," *Phys. Rev. B*, vol. 43, pp. 5950–5961, Mar 1991.

[97] A. W. Sandvik, "A generalization of handscomb's quantum monte carlo scheme-application to the 1d hubbard model," *Journal of Physics A: Mathematical and General*, vol. 25, p. 3667, jul 1992.

[98] Z. Yan, Y. Wu, C. Liu, O. F. Syljuåsen, J. Lou, and Y. Chen, "Sweeping cluster algorithm for quantum spin systems with strong geometric restrictions," *Phys. Rev. B*, vol. 99, p. 165135, Apr 2019.

[99] R. G. Melko and A. W. Sandvik, "Stochastic series expansion algorithm for the $s = 12$ xy model with four-site ring exchange," *Phys. Rev. E*, vol. 72, p. 026702, Aug 2005.

[100] P. Sala, T. Rakovszky, R. Verresen, M. Knap, and F. Pollmann, "Ergodicity breaking arising from hilbert space fragmentation in dipole-conserving hamiltonians," *Phys. Rev. X*, vol. 10, p. 011047, Feb 2020.

[101] V. Khemani, M. Hermele, and R. Nandkishore, "Localization from hilbert space shattering: From theory to physical realizations," *Phys. Rev. B*, vol. 101, p. 174204, May 2020.

[102] S. Moudgalya and O. I. Motrunich, "Hilbert space fragmentation and commutant algebras," *Phys. Rev. X*, vol. 12, p. 011050, Mar 2022.

[103] O. Hart and R. Nandkishore, "Hilbert space shattering and dynamical freezing in the quantum ising model," 2022.

[104] A. Yoshinaga, H. Hakoshima, T. Imoto, Y. Matsuzaki, and R. Hamazaki, "Emergence of hilbert space fragmentation in ising models with a weak transverse field," *Phys. Rev. Lett.*, vol. 129, p. 090602, Aug 2022.

[105] F. Balducci, A. Gambassi, A. Lerose, A. Scardicchio, and C. Vanoni, "Localization and melting of interfaces in the two-dimensional quantum ising model," *arXiv preprint arXiv:2203.09495*, 2022.

[106] F. Balducci, A. Gambassi, A. Lerose, A. Scardicchio, and C. Vanoni, "Interface dynamics in the two-dimensional quantum ising model," *arXiv preprint arXiv:2209.08992*, 2022.

[107] D. Delmastro and J. Gomis, "Symmetries of abelian chern-simons theories and arithmetic," 2019.

[108] M. Oshikawa, Y. B. Kim, K. Shtengel, C. Nayak, and S. Tewari, "Topological degeneracy of non-abelian states for dummies," *Annals of Physics*, vol. 322, no. 6, pp. 1477–1498, 2007.

[109] H. B. Xavier, C. Chamon, and R. G. Pereira, "Network construction of non-abelian chiral spin liquids," 2022.

[110] T. Iadecola, T. Neupert, C. Chamon, and C. Mudry, "Ground-state degeneracy of non-abelian topological phases from coupled wires," *Phys. Rev. B*, vol. 99, p. 245138, Jun 2019.

[111] M. B. Hastings and T. Koma, "Spectral gap and exponential decay of correlations," *Communications in Mathematical Physics*, vol. 265, pp. 781–804, Aug 2006.

[112] V. Bouchiat, D. Vion, P. Joyez, D. Esteve, and M. H. Devoret, "Quantum coherence with a single cooper pair," *Physica Scripta*, vol. 1998, p. 165, jan 1998.

CURRICULUM VITAE

[redacted]